Double graphene quantum dots and hybrid resonators for THz quantum devices

Solen Coeymans

Sorbonne Université

Ecole Doctorale 397 : Physique et Chimie des Matériaux

Laboratoire de Physique de l'École Normale Supérieure

Double graphene quantum dots and hybrid resonators for THz quantum devices

Solen COEYMANS

Thèse de doctorat de Physique et Chimie des Matériaux

Dirigée par Juliette MANGENEY

Directrice de recherche, LPENS, Paris, France

Présentée et soutenue publiquement le 07 Novembre 2024 à Paris.

Rapporteurs :

François Parmentier – *Chargé de recherche, SPEC, Saclay, France*

Olivier Gauthier-Lafaye – *Directeur de recherche, LAAS, Toulouse, France*

Examinatrice :

Cheryl Feuillet-Palma – *Maître de conférences, LPEM, Paris, France*

Président :

Jean-François Lampin – *Directeur de recherche, IEMN, Villeneuve d'Ascq, France*

Invité :

Yanko Todorov – *Directeur de recherche, LPENS, Paris, France*

On serait tenté de croire que cette création a eu dans le passé une quelconque forme fonctionnelle et qu'aujourd'hui l'objet est simplement cassé. Mais cela ne semble pas être le cas. Aucun signe du moins ne le donne à penser ; on ne voit nulle part de traces d'insertion ou de zones de rupture qui pourraient renvoyer à quelque chose de ce genre ; l'ensemble a certes l'air absurde, mais, à sa manière, achevé. On ne saurait d'ailleurs rien dire de plus précis sur cet objet, car Odradek est extraordinairement mobile et ne se laisse pas attraper.

Franz Kafka - *Le Souci du père de famille.*

Abstract

This thesis focuses on the development of THz quantum devices, addressing the challenge of coupling a two-level system to a THz resonator. The THz spectral range, typically situated between 100 GHz and 30 THz, has long been considered as a "technological gap" due to the lack of viable solutions for the generation and detection of THz waves. However, recent remarkable advances in THz technology are opening up new possibilities for fundamental research and applications are today, the current THz gap is clearly in quantum technologies. Indeed, quantum technologies at THz frequencies are still in their infancy, while the neighboring spectral domains of microwaves and optics have seen considerable growth. . However, the unique properties of THz waves hold great promise for many quantum applications, such as secure wireless quantum communication, solid-state qubits and quantum sensing.

The main objective of this work is to evaluate the potential of graphene double quantum dots (double GQDs) to act as a two-level system operating in the THz range, and to couple them to a THz resonator. GQDs hold great promise for the development of THz quantum devices, as their energy level spacing is in the THz range, and they exhibit ultrahigh sensitivity to coherent THz radiation due to their exceptionally large THz electric dipole.

This thesis addresses a first challenge, which is the cleanroom nanofabrication of physically etched double GQD-based devices and their integration with LC resonators. Nanofabrication involves graphene and hexagonal boron nitride (hBN) exfoliation and transfer, heterostructure characterization, electron-beam lithography and etching steps. Using dark transport spectroscopy at low temperature (300 mK), we demonstrate that a double GQD acts as a two-level system with a resonance frequency in the THz frequency range. This is a milestone towards the development of THz quantum systems.

Another key objective of this thesis concerns the development of hybrid THz resonators, for exploiring the quantum interactions between THz light and a two-level system, such as a double GQD. Our approach relies on the ultra-strong coupling of a THz Tamm cavity to an LC-circuit metamaterial. We demonstrate that these hybrid resonators conciliate a high Q factor with sub-wavelength mode confinement. However, these hybrid THz resonators are not optimized for coupling to a discrete material system such as a double GQD. Our approach to overcome this issue is to reduce the in-plane spatial extension of the Tamm mode to thus enhance its interaction with a single LC resonator. Our strategy is to replace the plane metal mirror of the Tamm cavity with a finite-size metal disk. Using simulation and experiment, we characterize the properties of these original THz confined-mode Tamm cavities.

The outcomes of this thesis work are important for the development of future THz quantum devices. Indeed, coupling a double GQD, acting as a two-level system at THz frequencies, to hybrid THz resonators by leveraging various coupling regimes, from weak to ultra-strong, will enable the generation and detection of non-classical THz light states. Improving our understanding of light-matter interaction at THz frequencies should pave the way for major breakthroughs in THz quantum technologies.

Résumé

Cette thèse se concentre sur le développement de dispositifs quantiques fonctionnant dans la gamme des fréquences térahertz (THz), en relevant le défi de coupler un système à deux niveaux à un résonateur THz. La gamme spectrale THz, située typiquement entre 100 GHz et 30 THz, a longtemps été considérée comme un "fossé technologique" en raison du manque de solutions viables pour la génération et la détection des ondes THz. Toutefois, les progrès remarquables réalisés récemment dans le domaine de la technologie THz ouvrent de nouvelles possibilités pour la recherche fondamentale et les applications et aujourd'hui, le fossé THz se situe clairement dans les technologies quantiques. En effet, les technologies quantiques aux fréquences THz n'en sont qu'à leurs balbutiements, alors que les domaines spectraux voisins des micro-ondes et de l'optique ont connus un essor conséidérable. Cependant, les propriétés uniques des ondes THz sont très prometteuses pour de nombreuses applications quantiques, telles que la communication quantique sans fil sécurisée, les qubits à l'état solide et la détection quantique.

L'objectif principal de ce travail est d'évaluer le potentiel des doubles boîtes quantiques de graphène (doubles GQD) à agir comme un système à deux niveaux dans la gamme spectrale THz, et de les coupler à un résonateur THz. Les double GQDs sont très prometteurs pour le développement de dispositifs quantiques THz, car l'espacement de leurs niveaux d'énergie se situe dans la gamme THz, et ils présentent une sensibilité très élevée au rayonnement THz cohérent en raison de leur dipôle électrique THz particulièrement grand.

Cette thèse aborde un premier défi, à savoir la nanofabrication en salle blanche de dispositifs à base de double GQD physiquement gravés et leur intégration à des résonateurs LC. La nanofabrication implique l'exfoliation et le transfert de graphène et de nitrure de bore hexagonal (hBN), la caractérisation de l'hétérostructure, la lithographie par faisceau d'électrons et les étapes de gravure. En utilisant la spectroscopie de transport danbs l'obscurité à basse température (300 mK), nous démontrons qu'un double GQD agit comme un système à deux niveaux avec une fréquence de résonance dans la gamme de fréquences THz. Il s'agit d'une étape importante pour le développement de systèmes quantiques THz.

Un autre objectif clé de cette thèse concerne le développement de résonateurs THz hybrides, pour l'exploration des interactions quantiques entre la lumière THz et un système à deux niveaux, tel qu'un double GQD. Notre approche repose sur le couplage ultra-fort d'une cavité Tamm THz à un métamatériau à circuit LC. Nous démontrons que ces résonateurs hybrides concilient un facteur Q élevé avec un confinement de mode très sous-longueur d'onde. Cependant, ces résonateurs THz hybrides ne sont pas optimisés pour être couplés à un matériau discret tel qu'un double GQD. Notre approche pour résoudre ce problème est de réduire l'extension spatiale dans le plan du mode de Tamm et ainsi améliorer son interaction avec un résonateur LC unique. Notre stratégie consiste à remplacer le miroir métallique plan de la cavité Tamm par un disque métallique de taille finie. En utilisant la simulation et l'expérience, nous caractérisons les propriétés de ces cavités Tamm THz originales à modes confinés.

Les résultats de ce travail de thèse sont importants pour le développement de futurs dispositifs quantiques THz. En effet, le couplage d'un double GQD, agissant comme un système à deux niveaux aux fréquences THz, à des résonateurs THz hybrides en tirant parti de différents régimes de couplage, de faible à ultra-fort, permettra la génération et la détection d'états lumineux THz non classiques. L'amélioration de notre compréhension des interactions lumière-matière à THz devrait ouvrir la voie à des percées majeures dans les technologies quantiques à THz.

Contents

Introduction

Terahertz (THz) frequency domain of the electromagnetic spectrum is typically defined as electromagnetic waves with frequencies between 100 GHz and 30 THz (wavelengths 3 mm-10 μm). While electronic methods of generation and detection are typically associated with microwaves at the lower-frequency end of the THz band, optical and photonic methods are used for infrared light at the upper boundary. The THz band is where the fields of electronics and optics meet up and was referred for many decades as a technological gap in terms of the lack of viable solutions for the generation and detection of THz waves [1]. In the recent years, impressive developments have been made in terms of both emitters and detectors with commercial applications [2]. Indeed, the exploration and exploitation of the THz region of the electromagnetic spectrum has been ongoing continuously, leading to substantial scientific progress in recent years on new applications and technologies at the cutting edge of scientific progress [3].

Today, the actual THz gap clearly concerns quantum technologies that have been flourishing in the neighboring spectral domains. In the microwave, superconducting qubits are currently at heart of quantum computers developed both by academia as well as high tech startups and companies. In the visible and telecom domain, quantum cryptography protocols have been demonstrated with satellite links. The THz domain, however, has considerably lagged behind these impressive developments, despite this frequency range presents several potential benefits. For instance, quantum cryptography at THz frequencies holds significant promise for secure wireless communications, as THz wireless links exhibit attenuation levels several orders of magnitude lower than free-space optical links in the presence of dust, fog and atmospheric turbulences [4]. Additionally, shifting the transition frequency of solid-state qubits—whether in superconducting circuits or semiconductor spins—from the GHz to the THz range could allow for higher operating temperatures. This shift would make it possible to utilize a simple ^{4}He pumping system, lowering the scaling limitations imposed by the cooling power constraints of dilution refrigerators below 100 mK. Moreover, this transition to higher frequencies would also enable faster qubit manipulation. Nearly all polar molecules possess unique spectral signatures within the THz range, arising from transitions between rotational quantum levels [5]. Consequently, THz radiation can be used to manipulate the quantum states of these molecules, which are recognized as promising platforms for quantum computation and simulation due to their long-range interactions [6]. Finally, the ability of THz radiation to penetrate typically opaque materials and its resistance to Rayleigh scattering make it an invaluable tool for quantum applications like quantum telecommunications and quantum sensing [7].

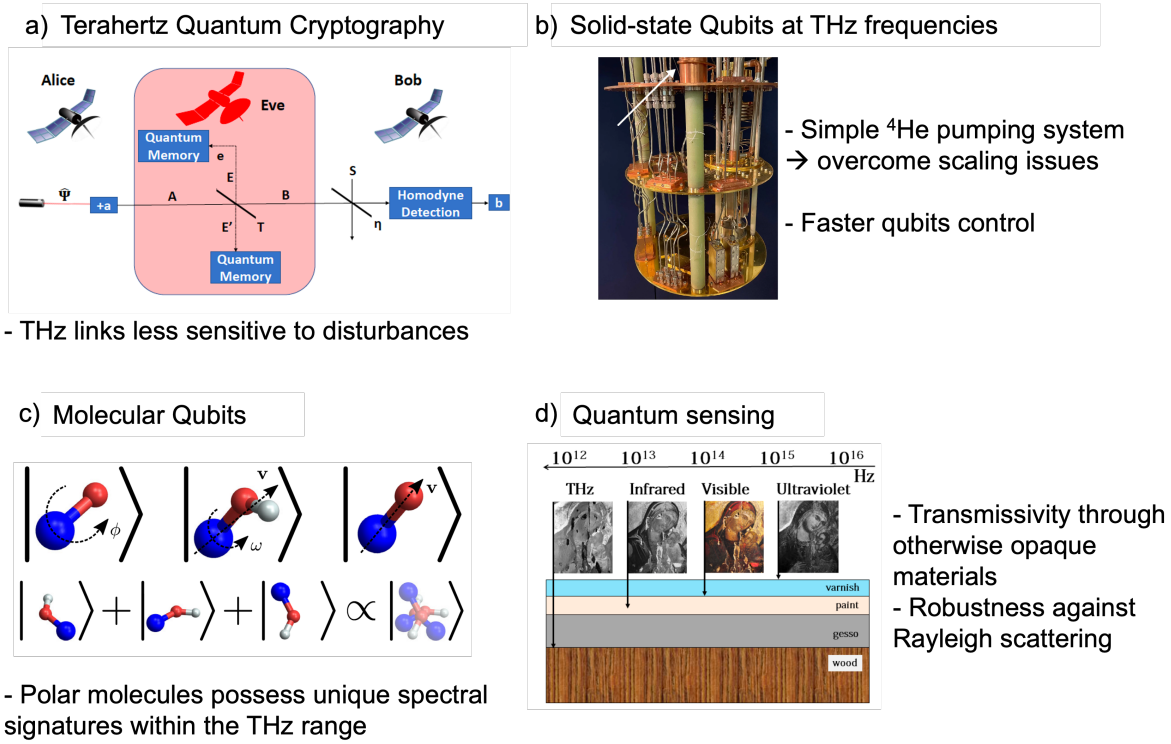

Figure 1: Illustration of key applications exploiting quantum technologies at THz frequencies: quantum cryptography (**a**), solid-state qubits (**b**), molecular qubits (**c**) and quantum sensing (**d**).

Despite these unique interests, quantum technology in the THz spectral range is still in its infancy mainly because THz technology is much less mature than that in microwave and optical domains. To date, the generation and detection of non-classical states of light [8, 9], which include single photon, squeezed light, Fock states and entangled photons, have seen very few achievements at THz frequencies. In theory, any nonlinear process can generate quantum light [10, 11] and a well-known approach to generate non-classical states of light is based on strong coupling between microcavity photons and quantum emitters, which in this specific case are required to be in the form of a two-level system. Squeezed light generation through strong coupling of a two-level system to a cavity has been successfully demonstrated in the optical range, for instance, using an InAs quantum dot coupled to a photonic crystal resonator [12], or a single Rb atom in a high-finesse optical resonator [13]. This technique has also been applied in the microwave range, using systems such as a Cooper pair box strongly coupled to a microwave coplanar resonator [14]. However, similar achievements in the THz spectral range remain elusive.

A main challenge is to achieve a two-level system with a resonance frequency in the THz spectral range. Quantum systems with a discrete energy spectrum whose energy spacing falls in the THz spectral range are mainly achieved in semiconductor quantum dots, molecules, impurities, and Rydberg atoms up to now. For example, graphene quantum dots (GQDs) with diameters of a few tens of nanometers, defined through physical etching [15], exhibit energy level spacings of a few meV. These GQDs are particularly promising for THz quantum optics due to their ultrasensitive response to THz photons [16, 17] and large THz electric dipole moment

[18]. Gate-defined QDs with THz frequency transitions have also been recently demonstrated in carbon nanotubes [19], InAs/InAsP quantum-dot nanowires [20], and AlGaAs/GaAs two-dimensional electron systems [21]. Alternatively, colloidal HgTe quantum dots with diameters around 100 nm, produced through bottom-up techniques, also show energy level spacings of a few meV [22]. Several molecules are also promising candidates as two-level systems in the THz range, thanks to their vibrational and rotational modes resonating at these frequencies. For instance, individual H_2 molecules have been demonstrated as two-level systems, with their coherent superposition being extremely sensitive to THz electric fields [23]. Similarly, low-energy vibrational modes of single C_{60} molecules [24] and quantum rotational excitations of water molecules have been observed in the few meV range [25].

The general context of this thesis is the development of quantum THz devices based on a two-level system coupled to a THz resonator under different coupling regimes, from weak to ultra-strong, for generating and detecting non-classical states of THz light.

To implement the two-level system with a resonance frequency in the THz spectral range, we will explore the potential of a double graphene quantum dot. Two-level systems based on double graphene quantum dots have been previously demonstrated by the Stampfer group at RWTH and the Ensslin group at ETH Zurich, with resonance frequency in the GHz spectral range. Their approach relies on gate-tunable band gap of bilayer graphene, which allows to electrostatically confine charge carriers. They investigated double quantum dot in bilayer graphene and demonstrated single electron occupation [26], as well as control over their tunnel coupling [27]. They also demonstrated a single-particle Pauli blockade in an ambipolar single electron-hole double quantum dot. Such a blockade may be utilized for either spin-to-charge or valley-to-charge conversion, and marks an important step towards realizing spin and valley qubits in graphene.

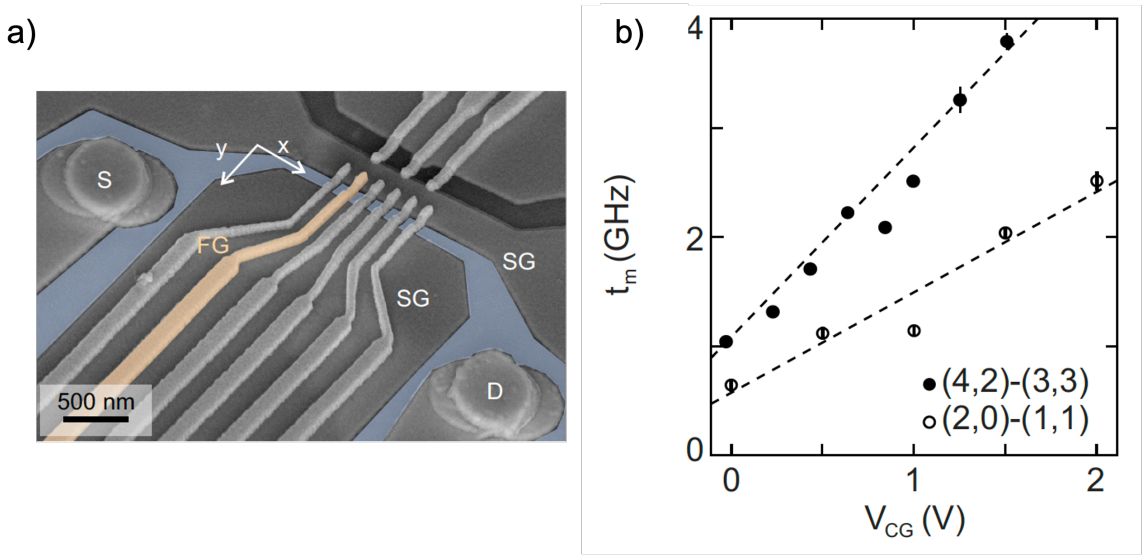

Figure 2: **(a)** SEM image of a bilayer double graphene quantum dot device. From [26]. **(b)** Tuning of the interdot coupling as a function of the central gate voltage in the GHz range. Adapted from Ref. [27].

In this PhD work, we investigate the potential of a double graphene quantum dot as a two-level system in the THz spectral range. Our approach relies of physically etched graphene quantum dots as this technological approach is mastered by the team and has been used successfully to fabricate single graphene quantum dot.

The realization of a THz resonator that efficiently couples its optical mode to a discrete structure such as a double GQD is difficult due to the substantial mismatch between the typical wavelength in the THz spectral range, $\lambda \sim 300$ μm at 1 THz, and the scale of the double graphene quantum dot of a few hundred nanometers. A main challenge is therefore to design a THz resonator that can store and concentrate the electromagnetic energy of the resonant mode in the small area of the discrete material system. THz resonators that efficiently store electromagnetic mode energy as well as those that confine electromagnetic mode energy on sub-wavelength volume are widespread today. However, THz resonators that meet both criteria simultaneously, -storing electromagnetic energy and confining it to sub-wavelength dimensions- remain elusive so far.

In this PhD work, we also investigate original hybrid THz resonators based on a Tamm cavity coupled to a LC circuit metamaterial that conciliate efficient storing of electromagnetic energy with sub-wavelength confinement.

In **Chapter 1**, we describe the fabrication of a single electron transistor based on a double GQD, physically etched, and encaspulated by hBN layers. In the first section, we outline the nanofabrication process of a 2D Van der Waals hBN-graphene-hBN heterostructure, along with its characterisation. In the second part, we detail the several steps and concerns involved in designing the double GQD through e-beam lithography, etching, and metallic deposition.

The **Chapter 2** concerns the characterization of the double graphene quantum dot based device using low temperature dark transport spectroscopy. The first part describes the state of the art of quantum dots in the THz spectral range. The second part presents the optical properties of graphene quantum dots in the THz spectral range and their THz quantum response. Finally, the third part presents dark transport spectroscopy measurements and analysis of the double graphene quantum dot based device. We use dark transport spectroscopy as a tool to probe the two-level system and quantify its resonant frequency.

In **Chapter 3**, we explore hybrid resonators based on Tamm cavities coupled to LC resonators. We will first present the basic of resonators and the state-of-the-art of resonators at THz frequencies. After, we will describe the properties and characterization of THz Tamm cavity. We will then report on our investigation of hybrid resonators based on Tamm-cavity coupled to LC circuit metamaterial and show that they combine efficient electromagnetic mode energy storage with electromagnetic mode energy confinement on sub-wavelength volume. Finally, we will present our research on the THz confined-mode Tamm cavity.

Bibliography

[1] Masayoshi Tonouchi. "Cutting-edge terahertz technology". *Nature Photonics*, 1, 2, pp. 97–105, 2007.

[2] S S Dhillon et al. "The 2017 terahertz science and technology roadmap". *Journal of Physics D: Applied Physics*, 50, 4, p. 043001, 2017.

[3] A Leitenstorfer et al. "The 2023 terahertz science and technology roadmap". *Journal of Physics D: Applied Physics*, 56, 22, 2023.

[4] Ke Su et al. "Experimental comparison of performance degradation from terahertz and infrared wireless links in fog". *J. Opt. Soc. Am. A*, 29, 2, pp. 179–184, 2012.

[5] D.M. Mittleman et al. "Gas sensing using terahertz time-domain spectroscopy". *Applied Physics B*, 67, pp. 379–390, 1998.

[6] Kaveh Najafian, Ziv Meir, and Stefan Willitsch. "From megahertz to terahertz qubits encoded in molecular ions: theoretical analysis of dipole-forbidden spectroscopic transitions in N2+". *Phys. Chem. Chem. Phys.*, 22, pp. 23083–23098, 2020.

[7] Mirco Kutas et al. "Terahertz quantum sensing". *Science Advances*, 6, 11, p. 8065, 2020.

[8] B. J. Lawrie et al. "Quantum Sensing with Squeezed Light". *ACS Photonics*, 6, 6, pp. 1307–1318, 2019.

[9] Vittorio Giovannetti, Seth Lloyd, and Lorenzo Maccone. "Quantum-Enhanced Measurements: Beating the Standard Quantum Limit". *Science*, 306, 5700, pp. 1330–1336, 2004.

[10] D. F. Walls. "Squeezed states of light". *Nature*, 306, 5939, p. 141, 1983.

[11] Ulrik L Andersen et al. "30 years of squeezed light generation". *Physica Scripta*, 91, 5, p. 053001, 2016.

[12] Andrei Faraon et al. "Coherent generation of non-classical light on a chip via photon-induced tunnelling and blockade". *Nature Physics*, 4, 11, pp. 859–863, 2008.

[13] A. Ourjoumtsev et al. "Observation of squeezed light from one atom excited with two photons". *Nature*, 474, 7353, pp. 623–626, 2011.

[14] Stojan Rebi ć, Jason Twamley, and Gerard J. Milburn. "Giant Kerr Nonlinearities in Circuit Quantum Electrodynamics". *Phys. Rev. Lett.*, 103, p. 150503, 2009.

[15] J Güttinger et al. "Transport through graphene quantum dots". *Reports on Progress in Physics*, 75, 12, p. 126502, 2012.

[16] Elisa Riccardi et al. "Ultrasensitive Photoresponse of Graphene Quantum Dots in the Coulomb Blockade Regime to THz Radiation". *Nano Letters*, 20, 7. PMID: 32470310, pp. 5408–5414, 2020.

[17] Abdel El Fatimy et al. "Epitaxial graphene quantum dots for high-performance terahertz bolometers". *Nature Nanotechnology*, 11, 4, pp. 335–338, 2016.

[18] Simon Messelot et al. "Large terahertz electric dipole of a single graphene quantum dot". *Phys. Rev. Res.*, 4, p. L012018, 2022.

[19] F. Valmorra et al. "Vacuum-field-induced THz transport gap in a carbon nanotube quantum dot". *Nature Communications*, 12, 1, p. 5490, 2021.

[20] Mahdi Asgari et al. "Quantum-Dot Single-Electron Transistors as Thermoelectric Quantum Detectors at Terahertz Frequencies". *Nano Letters*, 21, 20. PMID: 34618458, pp. 8587–8594, 2021.

[21] Kazuyuki Kuroyama et al. *Coherent interaction of a-few-electron quantum dot with a terahertz optical resonator*. 2023, 2023.

[22] Thibault Apretna et al. *Nanophotonics*, 10, 10, pp. 2753–2763, 2021.

[23] Likun Wang, Yunpeng Xia, and W. Ho. "Atomic-scale quantum sensing based on the ultrafast coherence of an H_2 molecule in an STM cavity". *Science*, 376, 6591, pp. 401–405, 2022.

[24] Shaoqing Du et al. "Terahertz dynamics of electron–vibron coupling in single molecules with tunable electrostatic potential". *Nature Photonics*, 12, 10, pp. 608–612, 2018.

[25] Shaoqing Du et al. "Inelastic Electron Transport and Ortho–Para Fluctuation of Water Molecule in H2O@C60 Single Molecule Transistors". *Nano Letters*, 21, 24. PMID: 34854686, pp. 10346–10353, 2021.

[26] Luca Banszerus et al. "Electrostatic Detection of Shubnikov–de Haas Oscillations in Bilayer Graphene by Coulomb Resonances in Gate-Defined Quantum Dots". *physica status solidi (b)*, 257, 12, p. 2000333, 2020.

[27] L. Banszerus et al. "Tunable interdot coupling in few-electron bilayer graphene double quantum dots". *Applied Physics Letters*, 118, 10, p. 103101, 2021.

Chapter 1

Fabrication of double graphene quantum dot based devices

For this first part of my PhD, I would like to thank the clean room team of the ENS - Michael Rosticher, José Palamo and Aurélie Pierret for helping me succeed the nano-fabrication part of a single electron transistor device based on graphene double quantum dot (double GQD). Romaine Kerjouan and Aurélien Schmitt also played a keen role in the graphene exfoliation and 2D materials assembly.

The nanofabrication of devices based on a double graphene quantum dot was very challenging and spanned about a full year. We carry out the nanofabrication mainly in the clean room at ENS, with the help of the people mentioned above. I was also kindly welcomed into the C2N team led by Rebeca Ribeiro, where I received support and advice on exfoliation and heterostructure stacking. I would like to sincerely thank her and all her team members for generously sharing their knowledge and expertise. It was a great help.

Since its isolation from graphite through exfoliation in 2004 [1], graphene has been a promising and inspiring one-atom thick 2D material with a wide range of applications, not only in physics and nanofabrication technology, but also in medecine or biology. Its unique structural, electronic, or mechanical properties, such as remarkable elasticity and high electronic mobility, have drawn widespread interest across multiple disciplines. As a result, the number of research publications on graphene has steadily increased since 2004, reflecting its growing importance in scientific and technological advancements.

This PhD research focuses on the exploration of a double GQD as an artificial two-level system with a resonance frequency in the THz range. Our objective is to develop a single-electron transistor device based on a high-quality double GQD. We also chose to insert the double GQD into the gap of a THz LC circuit resonator, with resonance frequency $\sim$350 GHz, in order to study the coupling of light and matter. These optical experiments could not be carried out within the framework of the thesis, but the fabrication of a device with a double GQD inserted into a THz resonator is a first key step towards the realisation of quantum devices based on a two-level system coupled to a resonator. However, this imposed significant geometric constraints, which made the technological implementation more complex.

To this purpose, we manually exfoliate graphene monolayer from a graphite sheet using the mechanical exfoliation technique to obtain a thin, high-quality monolayer graphene flake. This flake is then carefully aligned and encapsulated between two hBN layers to construct a two-dimensional Van der Waals heterostructure, ensuring high-quality and stability for the single-electron transistor [2]. The heterostructure has to be as clean as possible for optimum design and etching of the double GQD. In addition, the surface area of the heterostructure must be relatively large, as the pattern is quite large (12 x 8 μm). The heterostructure fabrication is very difficult, requiring relentless work to obtain large, clean heterostructures ready for further processing. The challenge is to exfoliate sufficiently large graphene and hBN flakes, with in addition a condition on the hBN flake thickness, and successfully assemble them to form clean and flat (without bubbles) 2D Van der Waals heterostructures.

Once a 2D heterostructure is assembled and its structure and surface characterized using Raman spectroscopy and Atomic Force Microscope (AFM) imaging respectively, electron beam lithography (EBL) and reactive ion etching (RIE) are used to define the double GQD, with two gates electrodes tuning energy levels in the right and left dot, and three other gates tuning the tunnel barrier between the two dots, and the dot and the reservoirs (source and drain). Another electronic lithography is performed to shape a THz LC resonator surrounding the double GQD, and form the ohmic 1D contacts for contacting the source and drain reservoirs, as well as the other five gates (see Fig. 1.1).

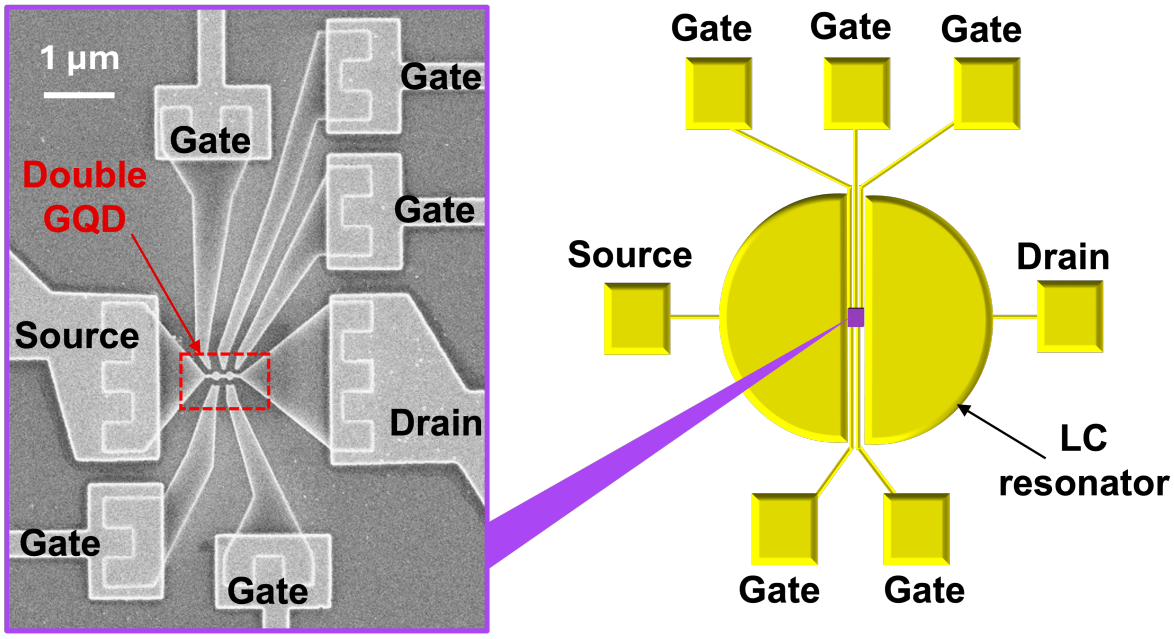

Figure 1.1: **Left:** SEM image of the double GQD connected to source and drain electrodes and of the five gates surrounded the quantum dots and constrictions. **Right:** Schematic of the device based on a double GQD in a single electron transistor geometry inserted in the gap of a LC resonator.

This chapter is solely dedicated to the nanofabrication of these novel samples, in a chronological manner. In the first section, we outline the nanofabrication process of a 2D Van der

Waals hBN-graphene-hBN heterostructure, along with its characterisation. In the second part, we detail the several steps and concerns involved in designing the double GQD through e-beam lithography, etching, and metallic deposition.

1.1 2D materials assembly

The first step preceding the design of the double GQD is to assemble the 2D materials, i.e. graphene monolayer and hexagonal Boron Nitride (hBN). It requires multiple steps which will be detailed below, ultimately resulting in clean and suitable heterostructures. For this purpose we will start with a general introduction of 2D based materials, before focusing on graphene and hBN mechanical exfoliation. Then we will explain how to actually assemble these 2D materials one on another by dry transfer. Please note that we completed everything detailed below, at the ENS clean room, or at C2N with the Rebeca Ribeiro's group .

1.1.1 2D materials : Graphene and hexagonal Boron Nitride

Graphene

In 2004, graphene was isolated by peeling off a block of graphite with adhesive tape [1]. For this PhD project, we use the same technique. Graphene is obtained through mechanical exfoliation (or micromechanical cleavage) from a large graphite crystal about 1 or 2 cm^2 in size and a few millimeters thick. The graphite is purchased from NGS Naturalgraphit GmbH, and the tape used is the Blue Low Tack tape from Semiconductor Equipement Corp, a dicing tape about 75 μm thick. We also use the Thick Clear Low Tack tape from the same company, which have the same adhesion level as the Blue one but is slightly thicker and clearer: it is sometimes easier to find large domains where potential graphene could hide. The procedure is detailed below and is depicted in Fig. 1.2a.

We place a block of graphite crystal on a 20x10 cm^2 piece of adhesive tape and apply light pressure with a pair of tweezers or thumb, see the first step of Fig. 1.2a. It is crucial to use a flat, relatively large and bright graphite crystal. We place it on the tape, apply pressure, then slowly remove it with tweezers. The goal is to obtain an area of clear greyish carbon zone on the tape. The thinner, clearer and denser the zones, the better. This may not be achieved on the first attempt. Further attempts can be made by placing the tape close to the first one, then starting to fold gently to obtain an area of around 1x1 mm^2 to search for graphene, as depicted in step 2 of Fig. 1.2a. After folding, the tape is gently unfolded to produce two zones of thinner carbon. This process is repeated several times until an area of grayish carbon is visible to the naked eye. One should stop before it begins to crackle, as this indicates potential damage for the graphene, resulting in multiple smaller graphene flakes. It is worth noting that the use of Clear Tape can be helpful, as it makes is easier to identify area.

Once a greyish dense and thin zone is found, the tape is stuck to the destination substrate. We use silicon covered by 280 nm oxide (SiO_2) to enhance the contrast when locating graphene flakes. The substrate is first cleaned with oxygen plasma for a few minutes to flatten its surface

at the nanometer scale, increasing the likelihood of the graphene adhering to it efficiently. When the tape is applied to the cleaned substrate, it is gently flattened using a soft plastic tool, such as the handle of a pair of scissors, to ensure proper adhesion. It is then baked on a hot plate. The tape is now ready to be gently removed from the substrate, see last step of Fig. 1.2a. In this way, on average around 4 of $\sim$ 20x20 μm^2 graphene flakes per substrate are obtained. Figure 1.2b is a microscope image of such graphene flake obtained using the mechanical exfoliation process.

(a) (b)

Figure 1.2: **(a)** Step by step mechanical exfoliation schematic representation. Adapted from [3]. **(b)** Microscope image of a typical exfoliated graphene flake, pointed by the red arrow, surrounded by multi-layers graphene with higher contrasts. The graphene flake is around 30 per 20 μm large and is sufficiently large for the following of the process.

Please note that there are alternative methods to obtain graphene besides mechanical exfoliation, such as Chemical Vapor Deposition (CVD) [4], which is also available at the ENS cleanroom or by epitaxial growth [5]. While both methods may be easier for obtaining larger graphene flakes (of a few square millimeters), their quality and electronic properties are nevertheless less interesting compared to the mechanical exfoliation technique.

Hexagonal Boron Nitride (hBN)

Despite its remarkable properties, graphene is affected by its surrounding due to its one-atom-thick 2D nature. Being exposed to the environment, especially to the SiO_2 layer in our case, can lead to various degradations, as the graphene surface may contain impurities that can cause charge scattering and charge traps, resulting in inhomogeneous doping and reduced carrier mobility. These issues can be solved by encapsulating graphene flakes in hBN layers. Indeed, the 2D material hBN is a suitable substrate for graphene flakes, as it has the same hexagonal crystalline structure as graphene. It is a wide bandgap semiconductor (around 6 eV) and its breakdown voltage is around 21 MV.cm^{-}1 [6] : thus hBN acts as an excellent insulating layer for graphene. By encapsulating the graphene with two hBN layers, graphene is less sensible to its environment [2], and is protected from potential sources of contamination during the fabrication process (lithographic polymers or solvants). This protection enhances the carrier mobility in graphene, limited by scattering on acoustic phonons ($\sim$ 100 000 cm^2/Vs at room

temperature), with a mean free path of up to 28 μm at cryogenic temperature [7, 8]. Nevertheless, previous works have shown that the carrier mobility depends on the bottom hBN thickness. According to [9], maximum carrier mobility in graphene is achieved when using heterostructures with a bottom hBN thickness greater than 15 nm. For a thickness below 15 nm, the underlying SiO_2 layer on silicon substrate still affects the hBN and graphene, as the roughness and charge impurities of the SiO_2 layers are not screened, impacting the overlaying graphene. The roughness of the hBN on the SiO_2 layers is reduced with hBN thickness, as its atomic flatness is only achieved for thickness above 15 nm. During the process, the thickness of the botton hBN is therefore of paramount importance. To ensure complete coverage of the graphene surface, hBN flakes larger than graphene flakes are needed, typically more than 20x20 μm^2 as a minimum. As with graphene, the cleaner, wrinkleless, more homogeneous the hBN flakes, the better. The bottom hBN layer should be flat and even, as the graphene surface follows its irregularities. Throughout this thesis work, the hBN layers we use were provided by Takashi Taniguchi and Kenji Watanabe from the National Institude for Material Science in Japan [10, 11].

To isolate the hBN flakes, we use PDMS wedges and exfoliated a few hBN crystals, which we manually place in-between the wedges and fold several times. Then we stuck a silicon wafer to one of the wedge surfaces. This process is supposed to lead to a large number of hBN flakes, more or less thick or large. However, it is quite hard to obtain the desired hBN flakes with this technique. This makes the process a real challenge. Fortunately, hBN exfoliation does not take long, allowing repeated attempts to find suitable hBN flakes relatively quickly.

Note that there are other ways to mechanically exfoliate graphene and hBN flakes, that we have encountered at the Rebeca Ribeiro's group at C2N laboratory. The technique involves regular scotch tape. An additional oven step at 380 °C is added to remove the residual tape glue on the chips. We do not follow this procedure at the ENS cleanroom as we do not have any permanent access to such an oven. With the additional oven step, the flakes are really thin and clean, with no wrinkles. We perform such process at C2N, and obtain large hBN flakes less than 10 nm thicks.

1.1.2 Transfer technique

To build a hBN-graphene-hBN heterostructure, the transfer technique is used. The principle involves Van der Waals forces between graphene and hBN. The Van der Waals attractive forces are stronger between the graphene and hBN flakes than with the SiO_2 substrate, making the heterostructure robust, yet still relocatable. The stacking technique can take weeks or months to master. Graphene and hBN are aligned by a stamp coated with a polymer, a kind of glue that sticks to the flakes, but the hBN and graphene flakes are fragile, almost invisible through the stamp. The success of the transfer depends on the polymer solution used and the temperature, which are not easily controllable, but we still managed to fabricate a large number of heterostructures. In the following section we will detail the one and only transfer process we use, developed by Columbia University. We call it the Columbia transfer method, as well as the Columbia stamp. We will explain the process of switching from 2D material layers to a

clean and bubbles-free 2D heterostructure. The last part will be dedicated to the (numerous) challenges we faced to fabricate such stacks. Please note that other transfer techniques exist, like the Aachen technique.

Columbia transfer method

At the ENS cleanroom, we use a custom-made transfer machine, consisting of a microscope with a long working distance objective, an XYZ stage for the positioning of the stamp, and a XY stage with an heating plate for the positioning of the substrate. Before my PhD, the set-up has been improved many times by former PhD students like Romaric LeGoff, Holger Graef, and during my PhD by Aurélien Schmitt.

Stamp fabrication

The Columbia-type stamps are fabricated using a small cube of PDMS ($\sim$ 2x2 mm^2). This cube is placed at $\sim$1 cm from the edge of a clean microscope glass side. The same cube can be used several times. Scotch tape (Duck HD Clear) is placed on top of the PDMS cube. Bubbles are removed with two glass slides: this way, there are no bubbles and the tape is well stretched over the cube, wrinklelessly. At this stage, the stamp is not yet sticky. To make it sticky, a thin layer of Polypropylene Carbonate (PPC) is deposited on the cube. The PPC is prepared by spin coating on a clean and heated SiO_2 layer on a silicon substrate. The thin layer of PPC is picked up with a piece of scotch tape with a hole of approximately the same size as the PDMS cube. The picking up technique may be tricky. If done properly, a PPC film should appear on the tape: the hole can be aligned with the PDMS cube, forming the stamp. Again, two slides are used to gently stretch the tape, before heating the stamp up to relax it, removing bubbles from the PPC-PDMS cube interface. Once the stamp has been fabricated, the transfer is ready to be carried out. Please note that heating the PPC seems to be a critical step, as the transfer process depends on the intensity of the PPC heating. As this layer is the interface between the hBN/graphene flakes and the buffer, the PPC fabrication step is really important.

Method using the transfer machine

The Columbia-type stamp on the glass side is mounted on the transfer station, between the microscope objective and the SiO_2 chip with hBN flakes previously exfoliated. The desired flake to be transferred should be aligned with the PDMS cube. Let us describe the transfer method :

- **Localize the touching point**, where the PPC is touching the substrate when lowering the stamp. It depends on how is prepared the stamp, and cannot be expected. When lowering the stamp, carefully bring into contact the PPC film and the wafer to localize the touching point.
- **Lower down the stamp** so that the PPC is a little bit in contact. Slowly increase the temperature to 45 °C. The PPC should start to become more fluidic and modulable, and

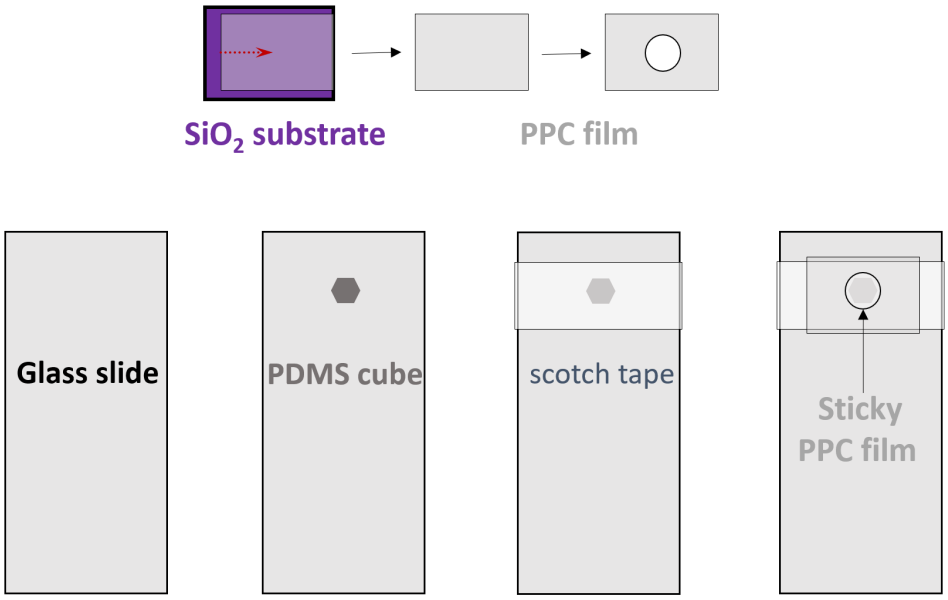

Figure 1.3: **Up :** Schematic process for PPC film fabrication. PPC is first spin coated on a SiO_2 substrate and heated (not represented). A thin PPC film can be extracted with a scotch tape (middle), and holed with a paper punching machine (right). **Down :** Columbia stamps fabrication process, consisting of a glass slide, a PDMS cube, scotch tape and a PPC layer.

reach the desired hBN flake: wait until the entire flake is covered with PPC. Heat up to 5 °C more if necessary, to help it cover the flake. This method prevents from excessive strain applied to the flake, as would happen during a mechanical way of covering the flake with PPC. See step 2 on Fig. 1.4.

- **Carefully lift the stamp** once the PPC does not move anymore. The flake should detach from the substrate and stay sticked to the stamp. The first lift up (top hBN) is generally the easiest compared to graphene and bottom hBN transfer. If it did not work (meaning if the flake has not moved from the substrate), it can be useful, before lifting the stamp, to lower the temperature from 45°C to the initial 40 °C, so that PPC cools down a bit and retracts on itself, to help the layer to stay sticked to the PPC. See step 3 in Fig. 1.4.
- **Remove the stamp from the transfer station** and put it on a hot plate at 95 °C for a few minutes so that any wrinkles that may have appeared on the PPC after last step disappear. Repeat the same step for graphene and bottom BN, aligning them as desired.
- **The sandwich is now on the stamp, ready to be deposited** on the desired substrate under the microscope. Lower it down until the touching point is reached, step 4 in Fig. 1.4, and start to heat at 120 °C (no need to go slowly here) beyond the melting point of PPC (which is around 60 °C). At this temperature, it is almost liquid, the adherence between PPC and the sandwich is lost : this is how you detach the sandwich from the stamp. Once 120 °C is reached, wait for the PPC to stop moving, step 5 in Fig. 1.4, and slowly lift the stamp up. "PPC arms" should appear while going up, meaning PPC residue are being left on the substrate. Those arms should also cover the sandwich, meaning it is also being deposited on the substrate. The sandwich is now left on the desired substrate, see step 6 in Fig. 1.4.

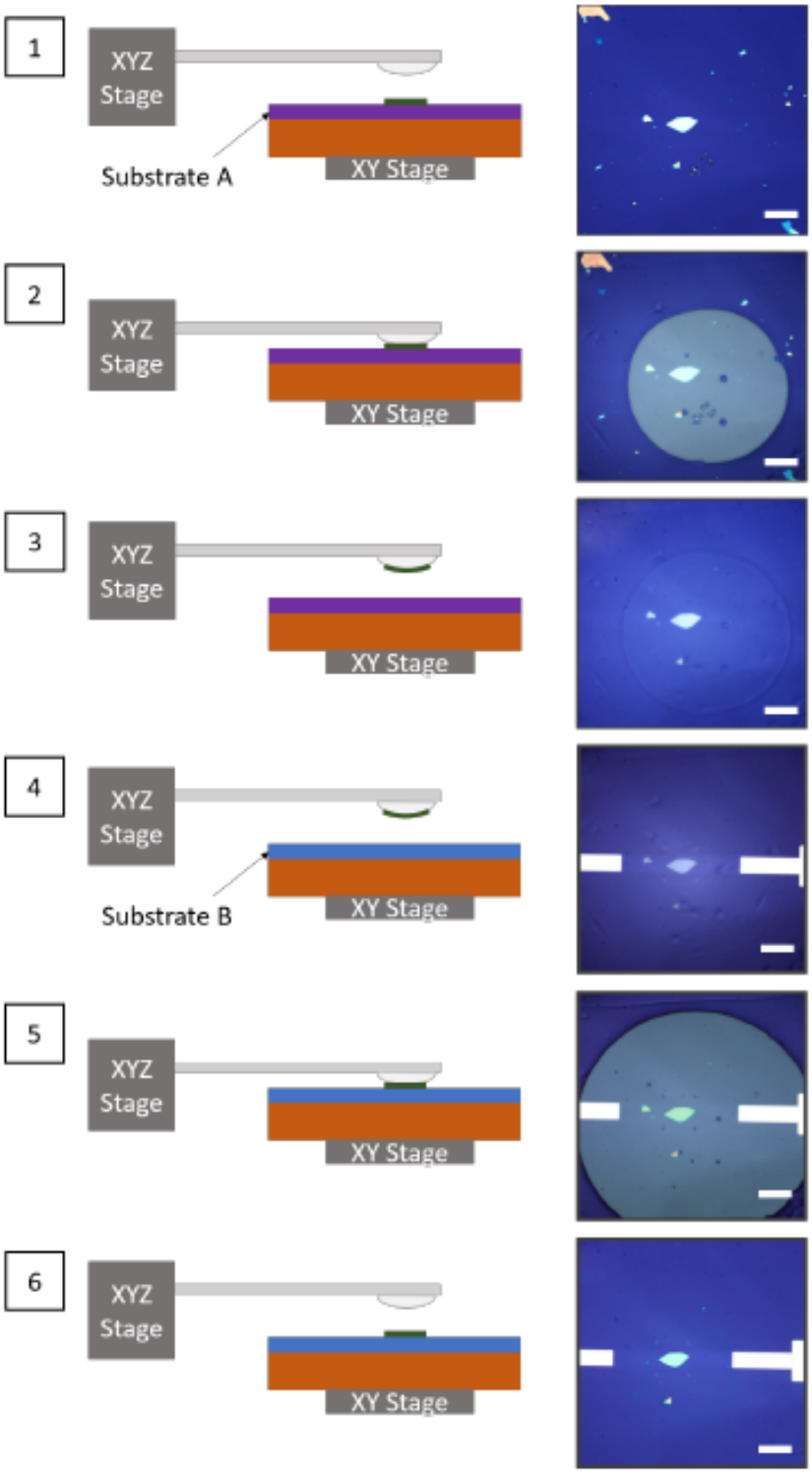

Figure 1.4: Dry transfer technique for 2D materials assembly using the transfer machine. On the left, step by step schematic of the transfer process. On the right, optical images of the contact zone for each step of the transfer of a hBN flake-scale bar 100 μm. Adapted from [3].

Cleaning PPC residue right after the transfer

As previously mentioned, the transfer of graphene and hBN flakes leaves residue of PPC on the substrate where the sandwich is deposited. Moreover, the sandwich is in direct contact

with PPC, whose residues can act as scatterers for graphene electrons, degrading the overall cleanliness and properties of the sample, particularly the electron mobility in graphene. It is thus necessary to clean the substrate containing the sandwich before moving forward in the process. For instance, it is possible to remove most of the PPC with acetone set at 50 °C for a few hours. This is what we mostly do. We also use to let the sample rest even longer in room temperature acetone, like an entire overnight, to ensure complete removal of PPC, as ultrasonic cleaning is forbidden once the sandwich is transferred to prevent any damage or detachment. After that, the substrate is rinsed in IPA and dried. Another way to clean the sample, which is more efficient and faster, involves a vacuum oven heating up to 350 °C. Unfortunately, no oven is available in the ENS clean room.

Post-transfer cleaning : bubbles removal

Once the initial cleaning is completed, the assembly of 2D materials is over and the heterostructure is now at our disposal, ready to be characterized. However, bubbles and other contaminants may still be trapped in the sandwich, even when the previously outlined method has been followed step by step. Fortunately, it is possible to remove them by a last transfer station step. A clean stamp with PPC heated slightly below its melting point (∼60 °°C) is used to push all the bubbles towards the edges of the heterostructure. At this temperature, the PPC is a relatively liquid but not excessively so. The user must then carefully move the PPC front line back and forth in a mechanical manner, the PPC front line responding really quickly at this temperature. Through this process, bubbles are visibly being pushed away by the front line, until it encounters a wrinkle or reaches the edge. On Fig. 1.5a, a considerable number of defects is visible on the Raman map of an heterostructure. The bubbles removal technique is used to push bubbles away, gathering them all into a large bubble, see Fig. 1.5b. The defects are moved away and gathered into reduced areas, with a lower Raman intensity. The entire surface of the heterostructure is cleaned.

Challenges and issues encountered during the transfer process

I would like to delve into the challenges encountered during the first part of the process, detailing why it was particularly difficult, especially considering the objectives of this PhD work. In the subsequent section, we will outline specific cases of these challenges and our strategies to overcome them.

Cleaning challenges in graphene pick up

As previously mentioned, the trick to obtaining larger graphene flakes during exfoliation is to clean the silicon/SiO_2 substrate for a few minutes with a plasma cleaner. This process flattens the substrate's surface, resulting in larger flakes. During this PhD, we first started to clean the silicon substrates with 10 or 20 seconds of plasma cleaner. However, the graphene flakes obtained were slightly too small : we had to start over. Therefore, we decided to extend the cleaning duration to a few minutes, resulting in larger graphene, as aimed. However, the more

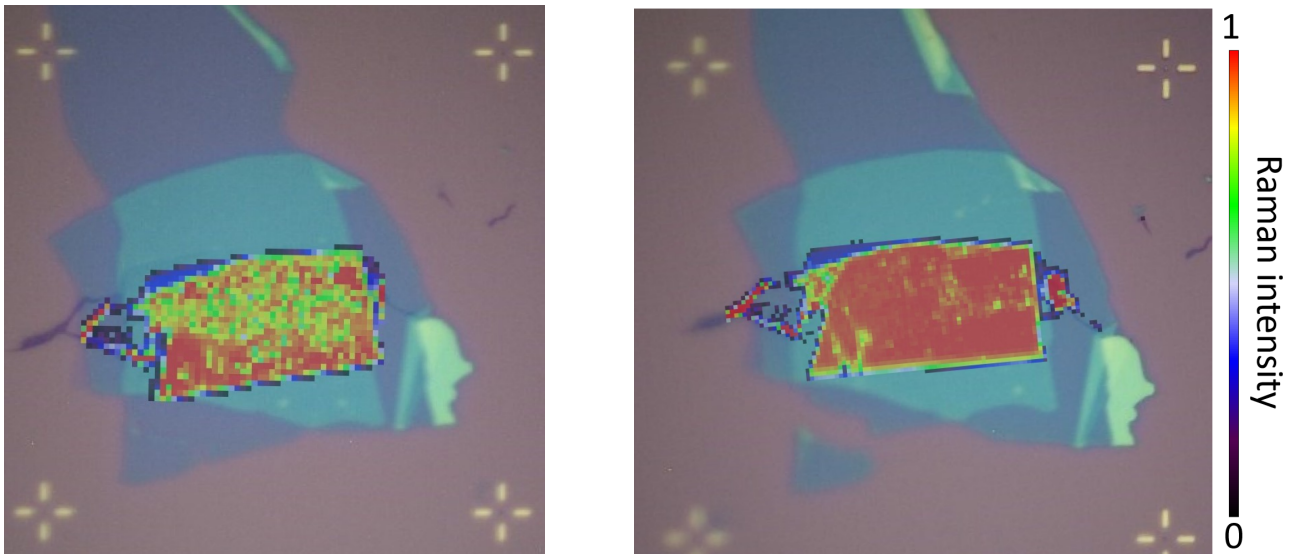

(a) (b)

Figure 1.5: **(a)** Mapping of the 2D peak intensity of an heterostructure that present defects due to the transfer process. Bubbles can clearly be seen . **(b)** Mapping of the 2D peak intensity of the same heterostructure as in **(a)**, but cleaned with the bubbles removal process. The heterostructure is now almost bubbles free. See part 1.1.3 for details on Raman spectroscopy.

the substrate is cleaned, the more challenging it becomes to transfer. Indeed, the substrate surface is clean and is as smooth as possible, with zero irregularities, making the stamp unable to detach the flakes. One has to find the right balance between the sizes of exfoliated flakes and cleaning time.

Challenges in stamp fabrication : another kind of stamp

Initially, we did not perform the Columbia method for fabricating stamps. Instead, we first used the droplet-PDMS-stamp fabrication technique. This stamp is made of a ∼5 mm droplet of liquid PDMS (the same PDMS used to build the PDMS cube in the Columbia method), again positioned at ∼ 1 cm from the edge of a glass side. It is then solidified, cleaned, spin-coated with a few drops of PPC, heated, and ready to use. This method is significantly easier (and cleaner), a large number of stamps can be made in a row, and they can be re-used several times. However, we found the PPC applications somewhat imprecise, as it consists in dropping a bit of PPC on the apex of the PDMS droplet before spin-coating. Sometimes, we felt that PPC thickness was not uniform, some domains on the droplet appeared to be PPC-free, making them non-sticky, or maybe half-sticky. Even when using brand new stamps, it did not change, indicating a problem with the PPC spin-coating process. This is why we turned to the Columbia stamp fabrication. With the same PPC, it appeared to work better. But it has to be done in a very appropriate way, as there is a higher risk of obtaining dirty stamps with large trapped bubbles that could reduce the stamp flatness and render the stamp unusable.

Choice of the optimum flake size for a successful transfer

The size of the hBN flakes must be larger than the graphene, so as to cover it completely, typically over $\sim$ 20x20 μm^2. This is the first requirement. The second is the size difference between the top and bottom hBN layers. For successful transfer, the top hBN layer must be larger than the bottom hBN layer, as this will facilitate the final step of transferring the hererostructure from the stamp to the target substrate. On the stamp, the heterostructure is positioned upside down, with the top hBN layer on its bottom. For deposition on the target substrate, the larger top hBN layer carries the graphene and bottom hBN layer, pushing them toward the substrate, ensuring their adherence. So, not only do we need to find hBN flakes that are larger than graphene, we also need to ensure that the top hBN is larger than the bottom hBN.

Challenges in aligning graphene with near-invisible hBN layers

During the transfer procedure, once a thin flake is transferred from the exfoliated substrate to the stamp, it appears almost invisible. The thinner it is, the less visible it becomes. It is already hard to observe through the stamp with the microscope. When dealing with graphene, an atomic thick layer that is inherently almost invisible and even less visible through the stamp, aligning it with an hardly visible hBN flake becomes a very tricky task. Once it is done, we still have to align the last hBN flake with the graphene flake on top of the actual bistructure hBN-graphene. Here, we face the same challenge : the graphene location is barely visible. As the thickness and cleanliness constraints significantly reduce the number of candidates for the bottom hBN layer, sometimes we ended up with a few options and decided to set our sights on one of them, despite its small size. Consequently, we did not have much margin for error when aligning the last hBN with the structure. As well as being a technical challenge, the transfer process requires a lot of training to acquire know-how and expertise.

Transfer machine set-up at the ENS

During the course of this PhD work, we had the opportunity to try out other transfer machines at the C2N laboratory. Compared to the ENS transfer machine, there is only a small conventional heating resistance serving as a heat source, provided by HQ Graphene company, which sells this transfer machine as a pack, and fits on a small table, providing a comfortable setting for the user.

1.1.3 Characterisation of graphene and 2D heterostructures

At this stage, the hBN/graphene/hBN heterostructure is deposited on the desired substrate, cleaned from PPC, ready for next step into the device fabrication process. To go further in the technological process, it is necessary to accurately determine the location of the graphene, its degree of cleanliness and freedom from defects, as well as the possible presence of unintended wrinkles. To this purpose, we characterize the heterostructure using AFM and Raman scanning

spectroscopy. These two techniques provide complementary information, which we detail in the following section.

Characterization of graphene monolayers using Raman spectroscopy

Raman spectroscopy offers detailed insights into the vibrational modes of samples, enabling the identification of the chemical and physical properties of graphene layers. It is a practical and non-destructive way to verify the monolayer character of an exfoliated graphitic flake. We mostly use Raman spectroscopy before and after the transfer of graphene.

After exfoliation, the first task is to identify potential candidates among the graphite flakes that appear thin and transparent enough to be a few graphene layers. Thanks to the 280 nm SiO_2 oxide on the silicon substrate, the optical contrast between graphene and the substrate is sufficient to determine their presence optically. However, it is difficult to distinguish monolayer graphene from bilayer or trilayer graphene, as they almost all look the same under the microscope. This is why Raman spectroscopy is used. All the Raman spectra and maps in this thesis were produced using a Renishaw inVia Raman microscope at an excitation wavelength of 532 nm, available at ENS cleanroom.

The Raman spectra are composed of several specific peaks, each corresponding to a microscopic process within the graphene band structure [12, 13]. The most prominent features in the Raman spectrum of graphene include the G-peak at ~ 1580 cm^{-1}, the 2D-peak at ~ 2700 cm^{-1}, and the D-peak at ~ 1345 cm^{-1}. The one-phonon scattering process in graphene is illustrated in Fig. 1.6a. An incoming photon of frequency ω_L excites an electron from the valance band to conduction band, creating an electron-hole pair. The excited electron then relaxes to another state by emitting a phonon of frequency ω_{phonon}, and recombines with the hole, emitting a photon of frequency $\omega_S = \omega_L - \omega_{phonon}$. Due to graphene gapless semiconductor nature, resonant electronic transitions are always possible. This results in the G-peak around 1585 cm^{-1}, appearing in any carbon-based material with a hexagonal structure.

All other microscopic processes in the graphene Raman spectrum involve more than one phonon. Here we focus on two-phonon process, represented in Fig. 1.6b. Momentum conservation requires the momenta of the two phonons to be opposite, allowing phonons from any part of the first Brillouin zone to participate. The Raman spectrum thus consists of a sum of Lorentzian curves, one for each possible combination of phonon branches. The 2D peak is one of these peaks, located at around 2700 cm^{-1}. The width and positions of these peaks are crucial, especially for the 2D-peak, as its shape varies significantly between monolayer and bi- or trilayer graphene. Specifically, the peak for monolayer graphene has the shape of a single thin Lorentzian, whereas for bilayer graphene it is broadened into a superposition of four different Lorentzian curves as the phononic branches are split due to the two layers [14]. The D-peak reflects the presence of defects in graphene, and is generally absent or very weak in exfoliated graphene. Another quality indicator is the ratio $\frac{I_D}{I_G}$ as the G-peak is not impacted by defects.

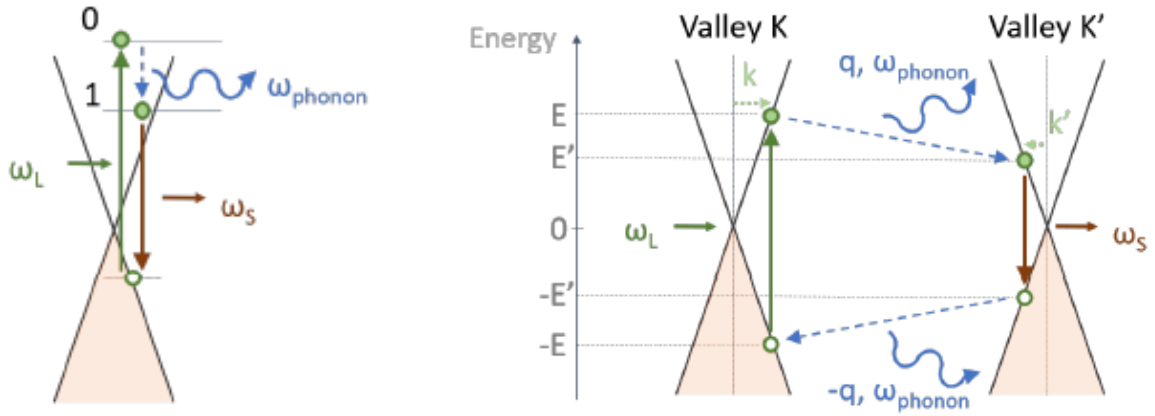

(a) (b)

Figure 1.6: **(a)** Schematic representation of the microscopic processes responsible for the G peak. The incident photon of frequency ω_L excites an electron up to an excited state, and relaxes to a lower state with the creation of a phonon of frequency ω_{phonon}. The electron recombines with a hole in its initial state by emitting a photon at frequency ω_S. **(b)** Schematic representation of the microscopic processes responsible for the 2D peak. An incoming photon of frequency ω_L creates an electron/hole pair in valley K, that scatters in valley K' by emitting two phonons of opposite wave vector. The electron recombines with a hole in its initial state by emitting a photon at frequency ω_S. Adapted from [3].

This ratio is therefore an indicator of the defects concentration in graphene [15]. To evaluate the quality of a graphene sample, one can also use the ratio $\frac{I_{2D}}{I_G}$, as the 2D peak intensity only comes from a double resonant Raman process, not from other electron scattering process, which would reduce the peak intensity. The higher the ratio is, the less the graphene is sensitive to other scattering effects. It should be greater than 1, and is generally the case for encapsulated graphene flakes [2]. For example, Figure 1.7 shows a the Raman spectrum of a high quality graphene flake.

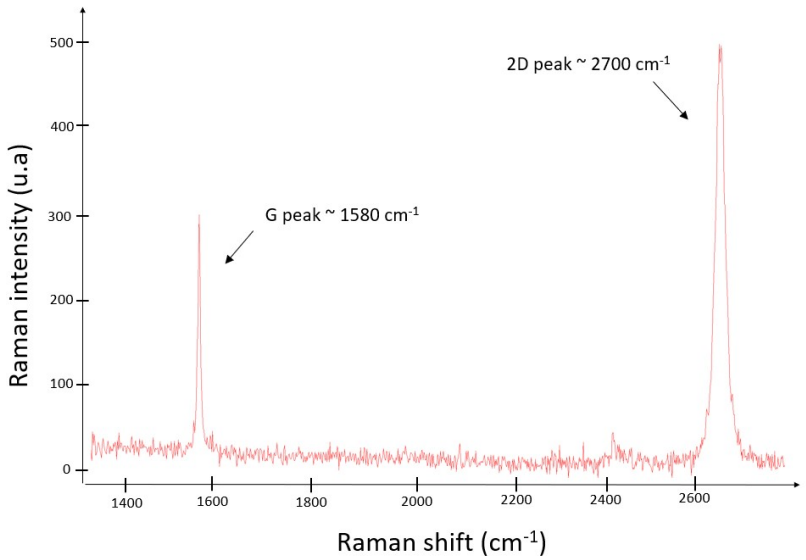

Figure 1.7: Raman spectrum of a high quality graphene flake. The defects D peak at $\sim$ 1385 cm^{-1} is not visible, indicating a high quality of the graphene flake, the G peak at $\sim$ 1580 cm^{-1} and the 2D peak at $\sim$ 2700 cm^{-1} are observed.

Characterization of hBN-graphene-hBN heterostructures using Raman spectroscopy

Raman spectroscopy is also used after the encapsulation step to check the quality of the graphene (which may be damaged, fold or torn during transfer) and observe its location by mapping the intensity of its 2D peak. This map is crucial as it will be used for the alignment during the lithography stage, which will be performed to pattern the double GQD.

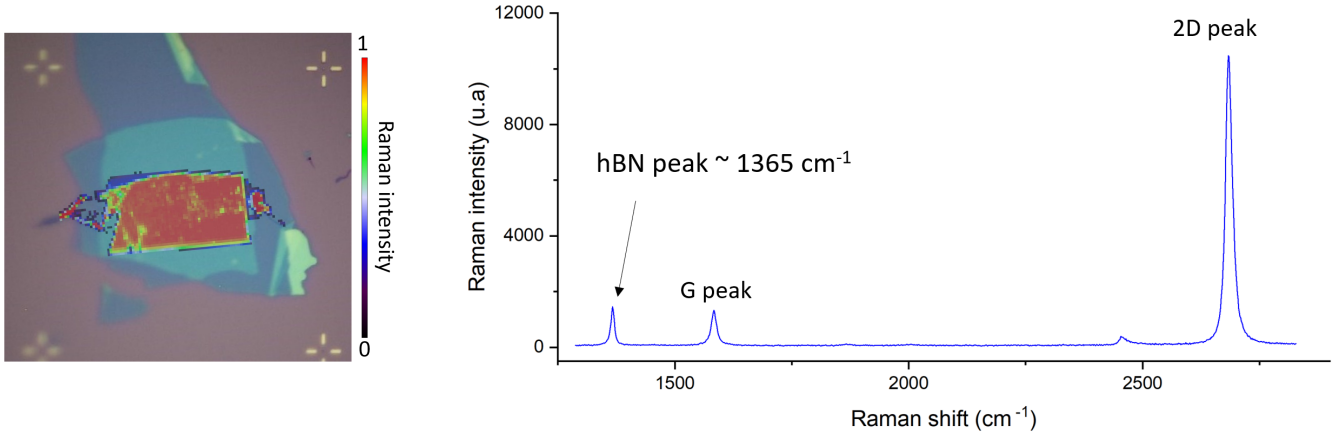

(a) (b)

Figure 1.8: **(a)** Map of the 2D peak intensity of the heterostructure at a specific position. It is crucial for the following of the process, as it will be used as an alignment layer. The double GQD pattern needs to be positioned within the large reddish area, ensuring a high-quality graphene. **(b)** The corresponding Raman spectrum recorded in the reddish area. Please note the appearance of the hBN peak at $\sim$ 1365 cm^{-1}.

When the graphene is encapsulated by two hBN layers, an additional peak appears on the Raman spectra, the hBN peak at $\sim$ 1365 cm^{-1} [16]. Its intensity is related to the thickness of the top and bottom hBN layers. The 2D-peak of graphene should still be a Lorentzian and the defect D peak should remain weak. The ratio $\frac{I_{2D}}{I_G}$ may be greater since the graphene is now encapsulated and protected from its environment. It is useful to generate different maps from a unique Raman scan, such as a 2D-peak intensity, a $\frac{I_{2D}}{I_G}$ ratio, or a D peak intensity, to determine the area of highest quality for the next step of the process.

Atomic Force Microscopy (AFM)

AFM provides high-resolution topographical imaging at the nanometer scale, allowing for precise measurement of surface roughness, thickness, and mechanical properties. It is particularly useful to check for residual surface contamination due to the transfer process, wrinkles, cracks or bubbles invisible to the microscope and thus avoid patterning the double GQD on a wrinkle or bubble. AFM measurements allow the surface of the heterostructure to be scanned, giving access to its shape and the thickness of the hBN layers. These parameters must be known in order to determine the desired depth of etching, see section 1.2.2. By examining the cut in the x-direction of the AFM scan, we observe that the top hBN layer extends beyond and rises above the bottom hBN, resulting in a tilted top hBN layer where it overlaps the bottom hBN.

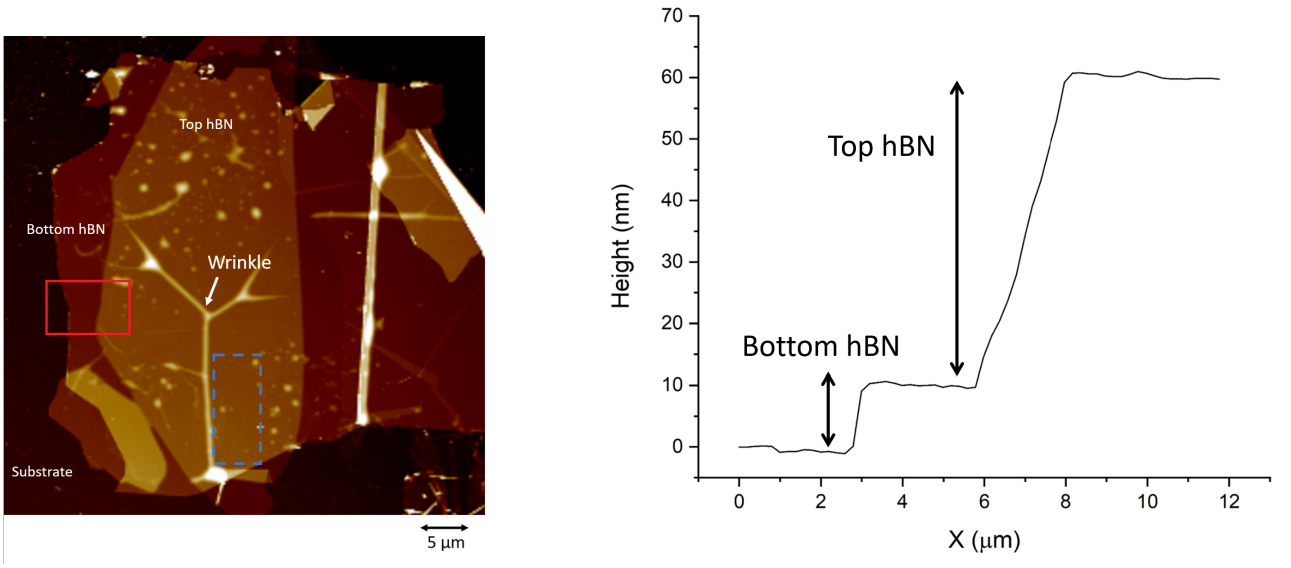

(a) (b)

Figure 1.9: **(a)** AFM scan image of a bottom hBN/graphene/top hBN heterostructure surface, revealing various irregularities such as wrinkles (indicated by the white arrow) or bubbles. The suitable area for patterning the double GQD is rather small (4 x 8 μm, see blue dotted rectangle), hence the importance of AFM scans. **(b)** Height profile cut along the horizontal direction in the red box in **(a)**, indicating the hBN sizes as a staircase profile. We extract a bottom hBN thixkness of about 10 nm and a top hBN thickness of about 50 nm. It is a necessary step in the fabrication process as it determines the etching time of the heterostructure after the patterning of the double GQD.

1.2 Fabrication of the double hBN/graphene/hBN quantum dot structure

In this section, we explain the final steps in the fabrication process for double GQD devices, which include lithographic patterning, reactive ion etching (RIE) and metal deposition. In a few words, electron beam lithography (EBL) is used to pattern a hard mask in the shape of the desired double GQD structure, protecting the materials beneath from the etch. During etching, anything not protected by the hard mask's protective layer is removed. The edges of the embedded graphene are then exposed, enabling one-dimensional contacts after metal evaporation.

1.2.1 Double GQD patterning

There are two types of lithography: optical lithography and electron-beam lithography. Both are used to pattern structures and provide a resist hard mask for further process. As explained above, the device comprises two GQDs with a radius of 60 nm and fine constriction of about 40 nm width, making laser lithography impossible to use due to its maximum resolution and realignment uncertainty, which are typically 1μm. Electron beam lithography (EBL), on the other hand, is much more efficient, with maximum resolution and uncertainty of the realignment procedure over 100 times finer, to the order of 10 nm.

To avoid wasting heterostructures, we perform dose tests on a similar hBN flake as those on the heterostructure. Dose tests are performed to fine-tune various parameters used during EBL process, such as exposure time during electron beam insolation, resist thickness or development. To preserve the resist mask obtained after electron beam exposure, a prior step is to spin-coat a few drops of Surpass 3000 on the chip. Surpass 3000 is an aqueous based priming agent used to reduce failure adhesion of photoresist on a wide range of materials, including SiO_2 layer and heterostructure [17, 18]. A scanning electron microscope image of the double GQD based structure, after resist development, is shown on Fig. 1.10. We use the Raith EBL at the ENS clean room, at 20 kV acceleration voltage and with the smallest 7.5 μm aperture. This step is preceded by the coating of the Hydrogen Silsesquioxane (HSQ) negative resist, see top right panel in Fig. 1.13. Negative and positive resists differences are depicted in Fig. 1.11. Following electronic exposure, HSQ resist undergoes chemical changes, solidifying and transforming into a material resistant to etching. Once developed and due to the negative tone of the lithography process, the patterned structure serves as a hard mask for etching. HSQ resist is commonly employed in semiconductor manufacturing, for the production of nanostructures and nanoscale devices, as it provides resolution less than 10 nm.

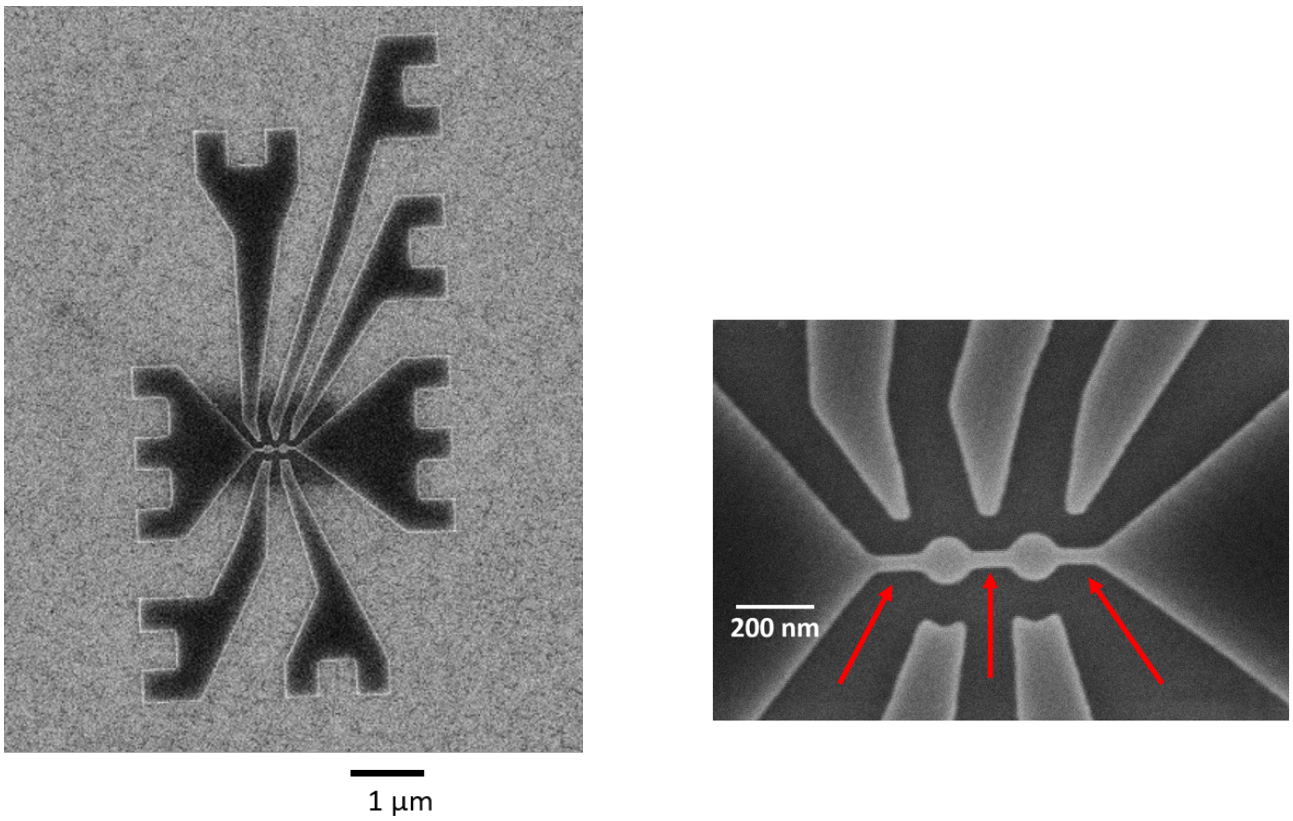

(a) (b)

Figure 1.10: **(a)** Scanning electron microscope (SEM) image of the double GQD structure after EBL and development, measuring 4.4 μm x 9 μm. A dark rectangle can be seen in the middle, on the dots, known as carbon contamination due to SEM observation on the dots [19]. **(b)** Close-up view of the quantum dots. As expected, their contours are sharp and well formed, as are the five lateral gates.

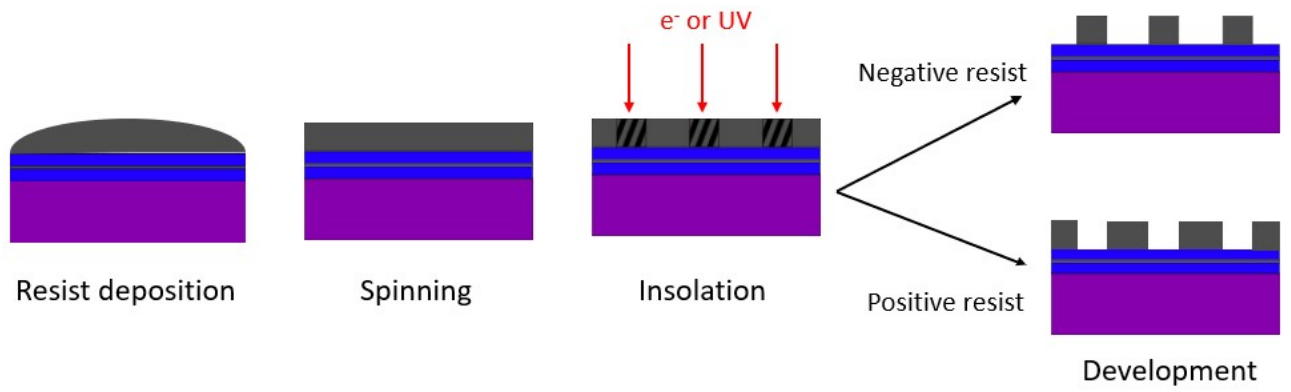

Figure 1.11: Diagram illustrating the differences in the development of negative and positive resists. After the development of negative resists, the insolated part is hardened and does not dissolve. On the contrary, the positive resist insulated part develops.

1.2.2 Reactive Ion Etching

Double GQD based structures

The desired hard resist pattern obtained in the first EBL step now serves as a protective mask to etch unprotected areas of the heterostructure. So, after EBL and resin development, an RIE is performed, directly removing the unprotected heterostructure area and enabling fabrication of the double GQD structure that includes the two quantum dots connected to each other and to the source and drain reservoirs by three constrictions, as well as the five gate electrodes.

All the samples fabricated are etched in the Corial 200R RIE at the ENS cleanroom, every time using the same RIE program, with CHF_3 and O_2 as agents used to etch hBN. RIE is a dry etching process in which a plasma is employed to chemically attack the material directly exposed to it, on the chip's surface. The accelerated gas in the RIE chamber also strikes the etched material and knocks off particles to physically remove them. The excess material is then pumped out of the chamber during the exhaust step, preventing contamination. Dry etching processes are intended to be anisotropic, controllable, and directional. Wet chemical etching processes are also used, such as HCl acid used to etch Chromium, but this type of etching is much less precise than dry etching and etches in an essentially isotropic way because the corrosive action occurs in all direction [20]. During this PhD work, we mainly use dry RIE process.

Edge contacts

The successful fabrication of the double GQD based device in a single electron transistor configuration critically depends on the ability to create electrical contacts, since the Ohmic resistance contact at the metal-graphene interface hinders the device performance, and needs to be as low as possible. Establishing direct contacts between the graphene layer (after opening by etching the top hBN layer) and metal electrodes would degrade the electrical properties of graphene in the vicinity of the 2D contact region [21, 22]. As depicted in Fig. 1.12a, this approach requires exposing a large graphene surface area for contact metallization, resulting in significant ohmic resistance [23, 24, 25]. In contrast, 1D edge contacts, as discussed in [8], demonstrate

significantly lower contact resistances [26]. This is due to the formation of covalent bonds between the metal atoms and the carbon atoms, as opposed to weak Van der Waals bonds, reducing contact resistivity. Consequently, the current flows predominantly along the edge of the graphene/metal interface, achieving low contact resistances [27, 28]. In this thesis, electrical contacts are established using the edge contact method from [8], hence the need to etch the entire unprotected heterostructure. A 1D edge contact is schematized in Figure 1.12b.

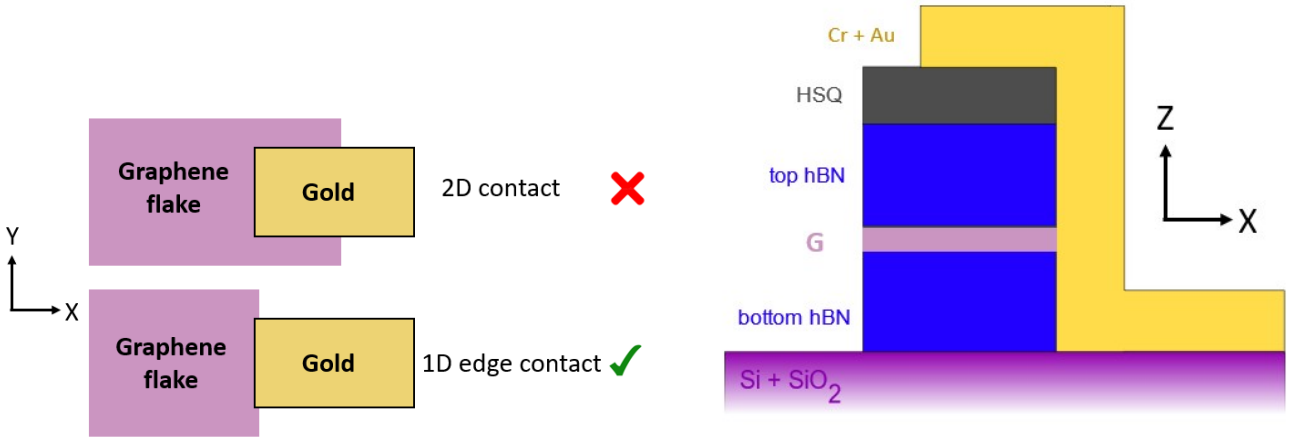

(a) (b)

Figure 1.12: **(a)** Schematic representation of the top view of the 2D and 1D contacts. **(b)** Cut view of the 1D edge contact achieved by metallization. See section 1.2.3 for details of the metallization process.

The required etch depth depends on the heterostructure height and must be at least smaller than the top hBN thickness, so that the buried graphene is exposed to the current flow after metallization. Graphene must be exposed at the edge of the structure to achieve 1D edge contacts, as shown in [8] (see bottom right panel in Figure 1.13). In this type of contact, electrical conduction occurs along the 1D atomic edge of the graphene layer after metallization. It is called 1D contact because a 1D line of the graphene edge is in contact with the metal after hBN etching, and so a 1D line is used for conduction (see Figure 1.10a). For this reason, we designed the comb-shaped structure to maximize the length of the 1D graphene line, thereby increasing the probability of making contact and achieving low contact resistance.

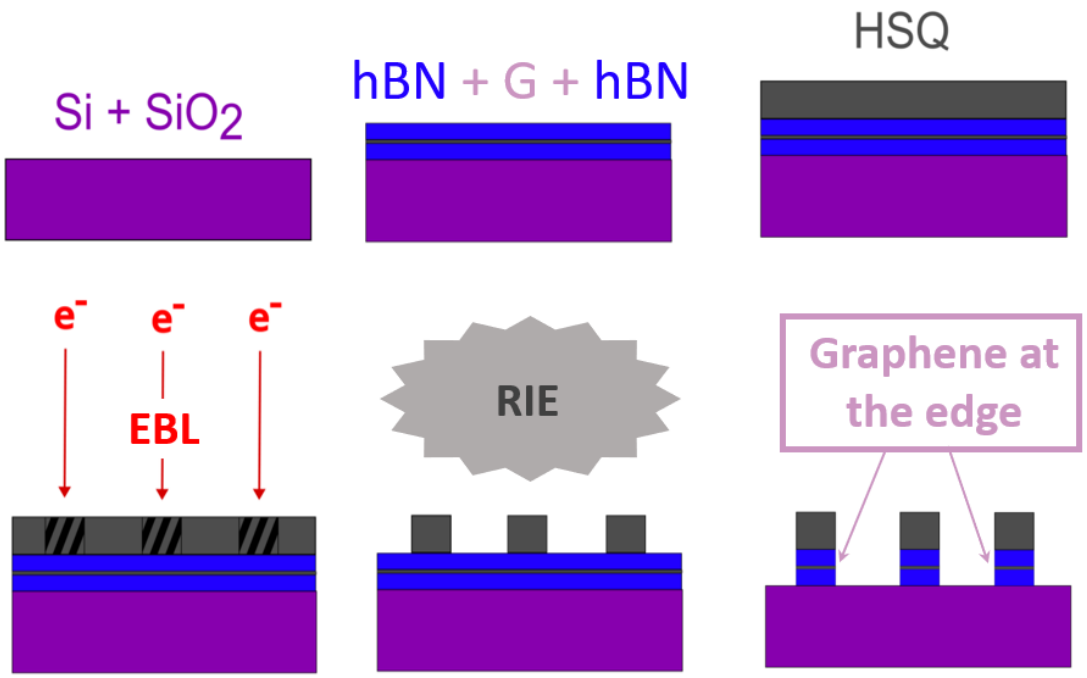

Figure 1.13: Schematic representation of the patterned structure achieved using EBL and RIE techniques. This is used for 1D edge contact metallization to provide current flowing through the device, as graphene is exposed at the edge of the structure.

The etching issue

The etching step is particularly critical as it determines the ability of electrons to flow through the double GQD based transistor. Etching too deeply, however, risks destroying the very fine constrictions (see red arrows in Figure 1.10b). In the course of this thesis work, we often encountered this problem. To overcome this problem, it is crucial to determine the optimum etching depth 1.14 and to assemble thinner heterostructures, in particular with a thinner bottom hBN layer, so that the remaining hBN height to be etched is low, thus reducing the etching time of exposed buried graphene. It is therefore critical to exfoliate very fine hBN flakes which makes heterostructure assembly very challenging.

We confirmed this interpretation by fabricating a simple test structure comprising the source/drain electrodes and a single thin constriction (without quantum dots or gates). The comb shape of the source and drain contacts and the width of the constriction remained unchanged. An initial etching step is carried out which provides a correct electrical connection between the source and drain electrodes. However, an additional 60-second etching process, using the same recipe, resulted in an open circuit. The graphene is already in contact with 1D, and the only critical region is the 40 nm width constriction line. From this test, we qualitatively conclude that the anistropy of the etch is not sufficient, and that a further 60 seconds of etching laterally etches all the graphene into the thin constriction line.

Another solution would be to etch only the top hBN layer, so that the graphene is accessible but not etched, regardless of the height of the bottom hBN. This would lead to a half-etched heterostructure, but would reduce the adherence of bottom hBN layer to the SiO_2 substrate.

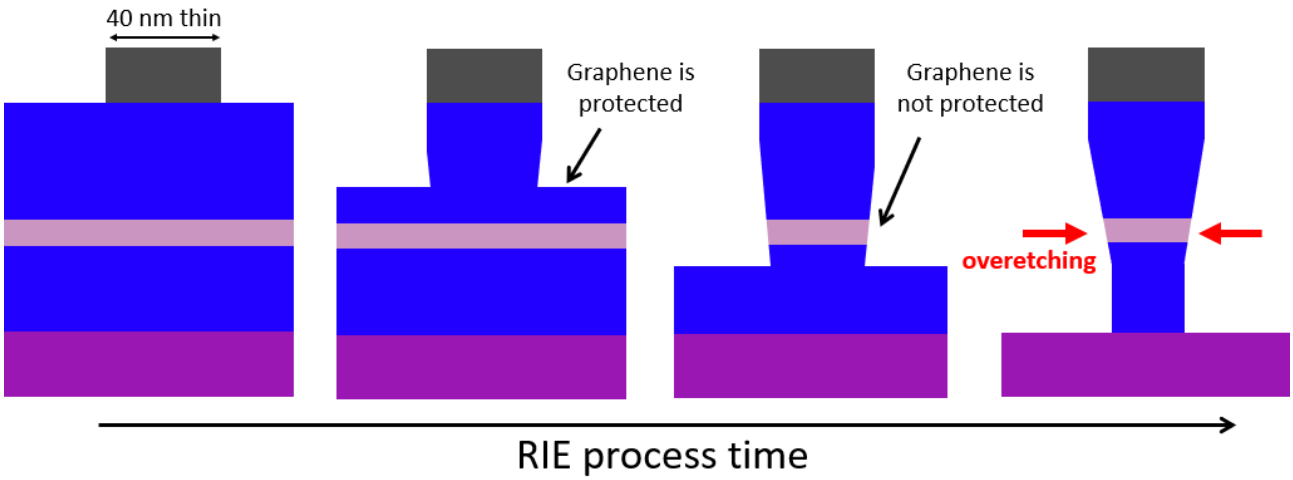

Figure 1.14: Graphene beneath the thin HSQ constrictionat the red arrow from Fig. 1.10b. Overetching kills the graphene underneath due to unintentional lateral overcut etching, destroying the constriction and the device.

We carried out several tests and adherence was not the main problem. Electrical tests revealed that our samples were either shunted, opened or both. Assuming a perfect fabrication process with the exception of this step, the reason for the open circuit between the source and drain electrodes would be that we may not have etched the top hBN layer sufficiently (see the second panel in Fig. 1.14). As a result, the top hBN layer is not fully etched and the graphene is still protected and inaccessible for 1D edge contact. In this situation, 1D edge contact fails, and no current can flow through the device. We therefore did not pursue this direction.

1.2.3 Pads and contacting wires patterning

A metallization step is then performed to fabricate metallic wires to connect the graphene structure to large metallic pads for further bonding. Initially, we pattern the wires and pads using positive laser lithography. We use AZ5214 as a positive resist and develop with AZ726 MIF. Alternatively, we perform electron-beam lithography, using PMMA (Polymethyl methacrylate) positive resist and developing with MIBK (Methyl isobutyl keton) diluted in IPA. 10 kV acceleration voltage and a 120 μm aperture is used. Although electron-beam lithography requires a lot of time (up to 6-7 hours, compared to only half an hour for laser lithography), it turns out to be a better process. After describing the gold metallization process, we will discuss why.

Chromium / Gold metallization and lift-off

Before loading the sample into the evaporator vacuum chamber for the metal deposition, a brief stripping step using O_2 as agent gas in the RIE is performed to clean residual resin on the sample. Then, we conduct almost all the metal depositions in the vacuum chamber of a Joule evaporator, at low pressure. Metal ingots are placed on a conductive crucible, which is coiled with a tungsten wire and heated by a current. The metal starts to heat up and evaporates by increasing the current. Due to high vacuum environment, metallic particles travel directly to the chip without colliding with other particles ballistically, ensuring a clean deposition. The desired thickness of metal deposit and its rate are monitored by a quartz sensor.

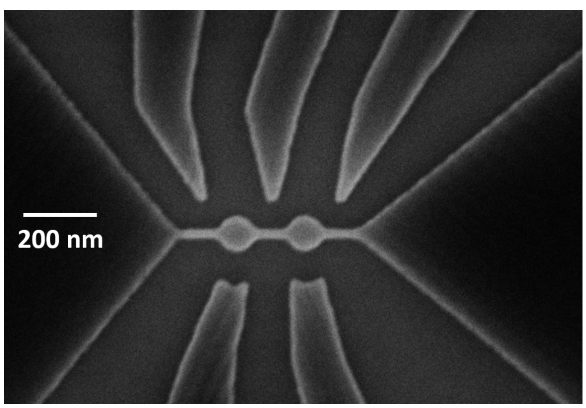

(a)

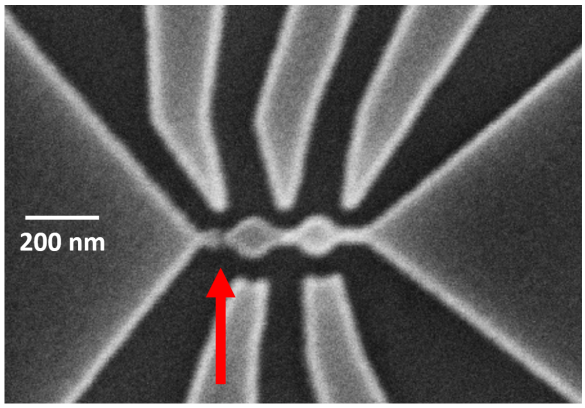

(b)

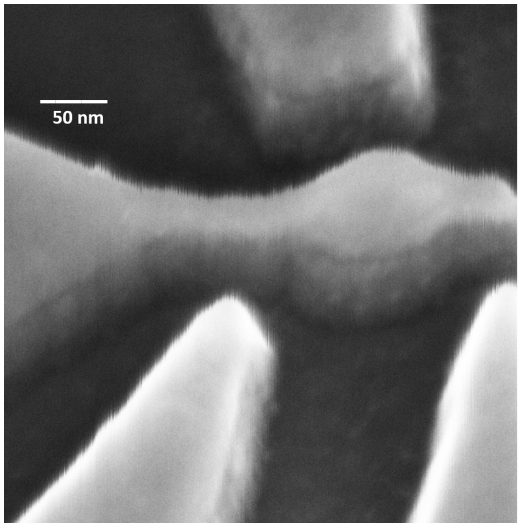

(c)

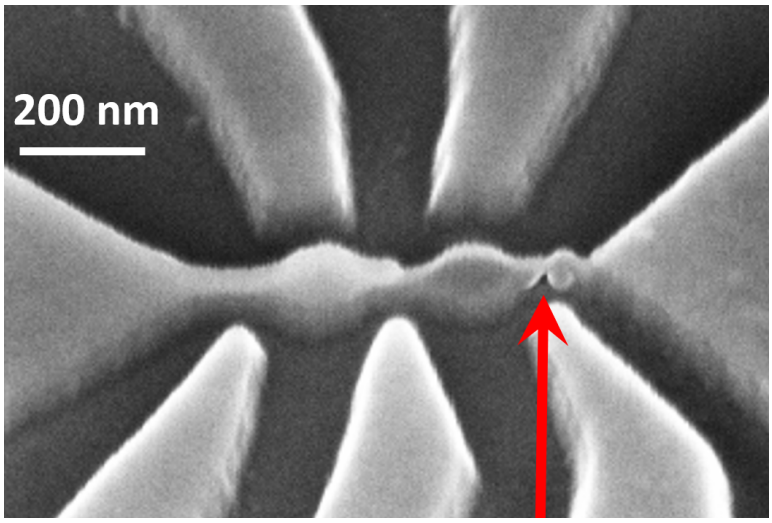

(d)

Figure 1.15: **(a)** SEM image of a double GQD patterned after EBL, before the etching step. The dots, constrictions, and gates are well defined. **(b)** SEM image of the same sample after 100 seconds of etching. A visible defect can be seen on the left connection, see red arrow, confirming the fact that RIE can damage the thin constrictions. **(c)** The same tilted and rotated double GQD through tilted SEM observation, showing the HSQ resist, the bottom and top hBN layers, and the graphene. The image shows the right constriction from (b), no defect nor gap is visible. **(d)** Same tilted observation of the double GQD, showing the same defect as seen in **(b)**. The red arrow highlights a visible gap in the graphene constriction, opening the conduction path. This is the reason for zero conductance between source and drain electrodes, as the corresponding electrical circuit is opened here.

First, a thin layer of a metal that adheres well to the substrate and HSQ resist is deposited. The best candidate for 1D edge contact with graphene is Cr, as the contact is less damaged by RIE-induced contamination [29, 8]. All our deposits start with a 10 nm Cr deposit at a speed of 0.3 $\mathring{A}.s^{-1}$. This is followed by 150 nm Au deposition at 3-4 $\mathring{A}.s^{-1}$. It is important that the Au deposition rate is less than 5 $\mathring{A}.s^{-1}$ to avoid the deposition of unwanted large aggregates of Au bubbles, resulting from collisions of several Au particles. Figure 1.16d illustrates such a case, where a gold-like particle is unintentionally deposited between two conductive lines, leading to a detrimental short-cut. Once deposition is complete, the chip is immersed in a hot acetone bath for an hour to remove the excess PMMA/Cr/Au layer, revealing the conductive lines and

the entire device.

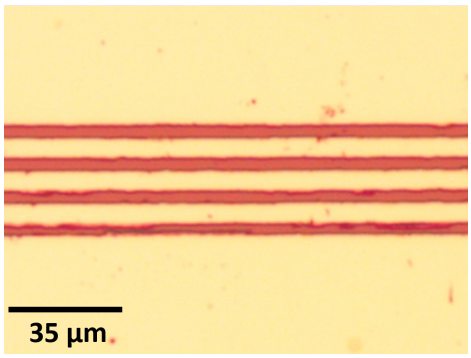

(a)

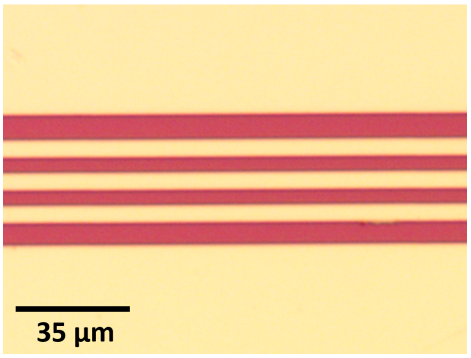

(b)

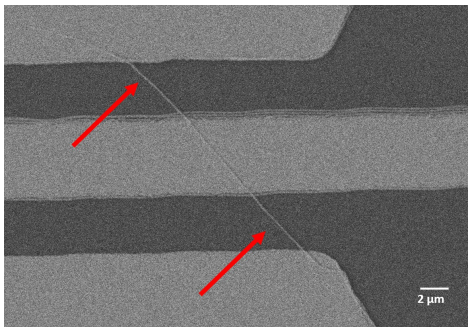

(c)

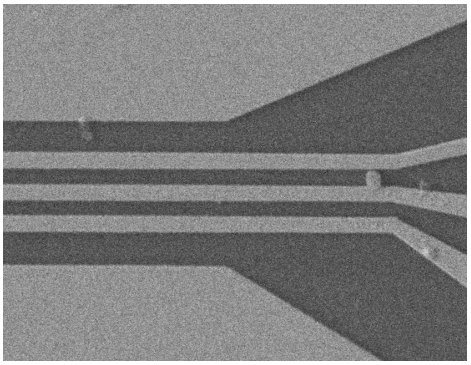

(d)

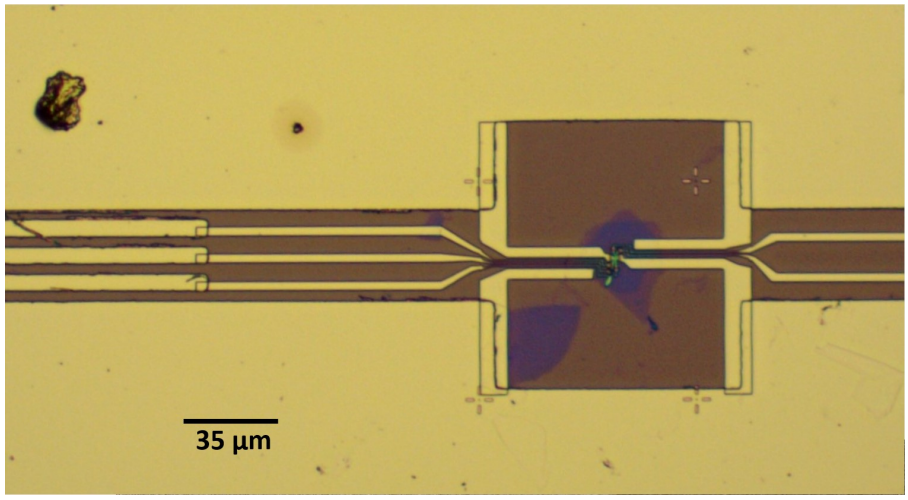

(e)

Figure 1.16: **(a)** A close-up microscope image of the three conducting wires patterned by laser lithography and covered by gold, after lift-off. They are not straight and clean, and seem to be on the verge to shunt, particularly for the two upper ones. **(b)** Same close-up view of the three conducting lines but patterned by e-beam lithography, after gold deposition. In this case, the lines appear perfectly straight and clean, with no visible defects or zig-zags. The difference with **(a)** is clear, and becomes even clearer through SEM observation. **(c)** SEM image of a shunted wire because of a mixture of PMMA, chromium and gold defect line, highlighted by the red arrow. **(d)** SEM image of an aggregate of gold-lookalike particle due to an excessive gold deposition rate. **(e)** Microscope image of a large area showing the double GQD and multiple defects, aggregates, gaps around it. Laser lithography was used for patterning the metallic wires.

Role of the lithography process in the metallization

The metallization step is always conducted in the same way, regardless the prior process is laser or electron-beam lithography. We observe several differences between the two approaches, which only became apparent after lift-off, the most striking being the straightness of the wires. The wires produced by laser lithography, as shown in Fig.e 1.16b after lift-off, lack clarity, definition, cleanliness and straightness. The distance between the lines appears to vary with position, exhibiting pattern distortion that makes the process difficult to control. Additionally, visible defects suggest that the lines are on the verge to shunt. Closer examination with SEM, depicted in Fig. 1.16c, reveals thin gold scratches, shunting three lines. By comparison, the lines patterned using electron-beam lithography in Fig. 1.16b are perfectly straight, clear and well defined wires. This problem only appears after metal deposition and lift-off, meaning that it is not due to the laser lithography itself. We attribute the distorted lines to the sidewall of the photoresist on the edges of the lines, which are in fact not perfectly sharp and vertical. The top layer of the coated photoresist undergoes a higher exposure dose than the bottom layer, resulting in an inverted pyramidal pattern, or undercut sidewall profiles after development of the positive photoresist [30]. The sketch in Fig. 1.17a illustrates both the lateral undercut profile and the overcut profile, which is the reverse, obtained with negative lithography. During the metallization process, gold tends to accumulate on the sidewall profile, making lift-off difficult and less accurate (see top right panel in Fig. 1.17b and [31]), resulting in distorted lines. The resist layer can also be heated by radiation from the evaporation source or by the kinetic energy of striking particles above its softening point, which tends to round it off even further, attenuating the slope of the resist step [32], further complicating lift-off.

We therefore chose to replace the laser lithography step with a second electron-beam lithography step. Since EBL resolution is much lower, pyramidal patterns are smaller, and the effect of metal build-up is reduced, resulting in almost perfectly straight lines after lift-off.

Once the lift-off process is completed, the process of the double GQD based device is over. Throughout this PhD work, numerous stacked heterostructures were abandoned before the first EBL step due to their low quality and small size. More than fifteen of them were completed. All this work carried out has led to the development of a complete, validated protocol for the fabrication of single electron transistors based on double hBN/graphene/hBN quantum dots.

This unique protocol, which involves exfoliation, stamping, transfer, e-beam lithography, etching and evaporation has led to the success fabrication of 3 samples. This technological development represents an important support for my thesis team in its future research related to graphene-based devices. We then investigate the transport through the fabricated double GQD devices using low-temperature transport spectroscopy measurements, which is the subject of the next chapter.

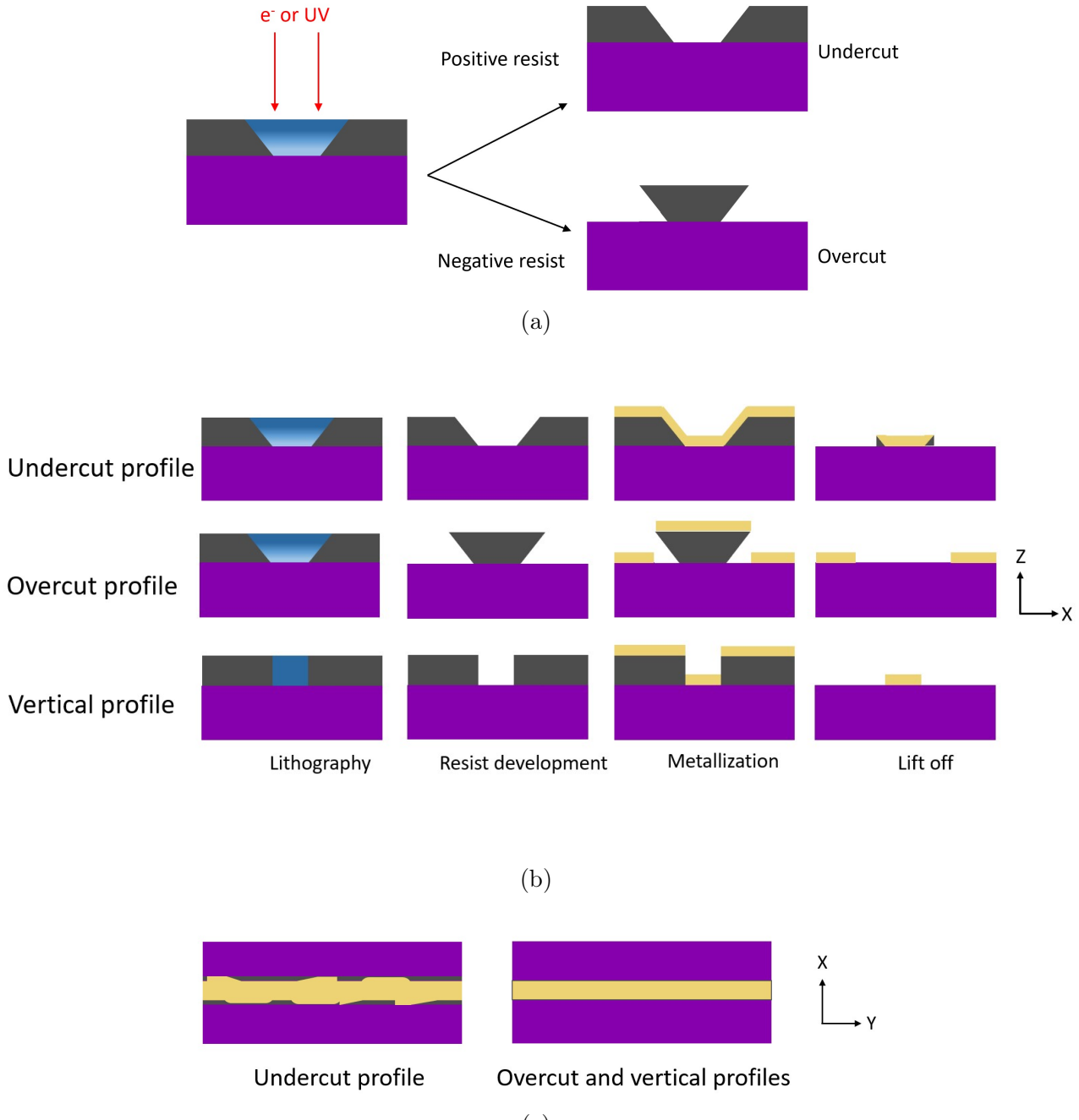

Figure 1.17: **(a)** Schematic representation showing the difference in the resist sidewalls after development, depending on the resist's tone. A positive resist leads to undercut profile edge. **(b)** Side cut representation of undercut, overcut and vertical profiles of the lithography resist side walls, due to different lithography processes. The metallization and lift-off are also represented, giving sharp and straight wires for wires with overcut and vertical profiles, but not for undercut profiles. In this case, gold tends to accumulate on the side wall profile, resulting in a less controllable lift-off and distorted lines **(c)** Top view of the wires after lift-off for undercut and overcut/vertical profiles. Due to uncontrollable gold accumulation on the edge of the side wall of the resist, the wires are not sharp and straight for undercut profile (left panel), compared to the case of an overcut/vertical profiles of the resist (right panel).

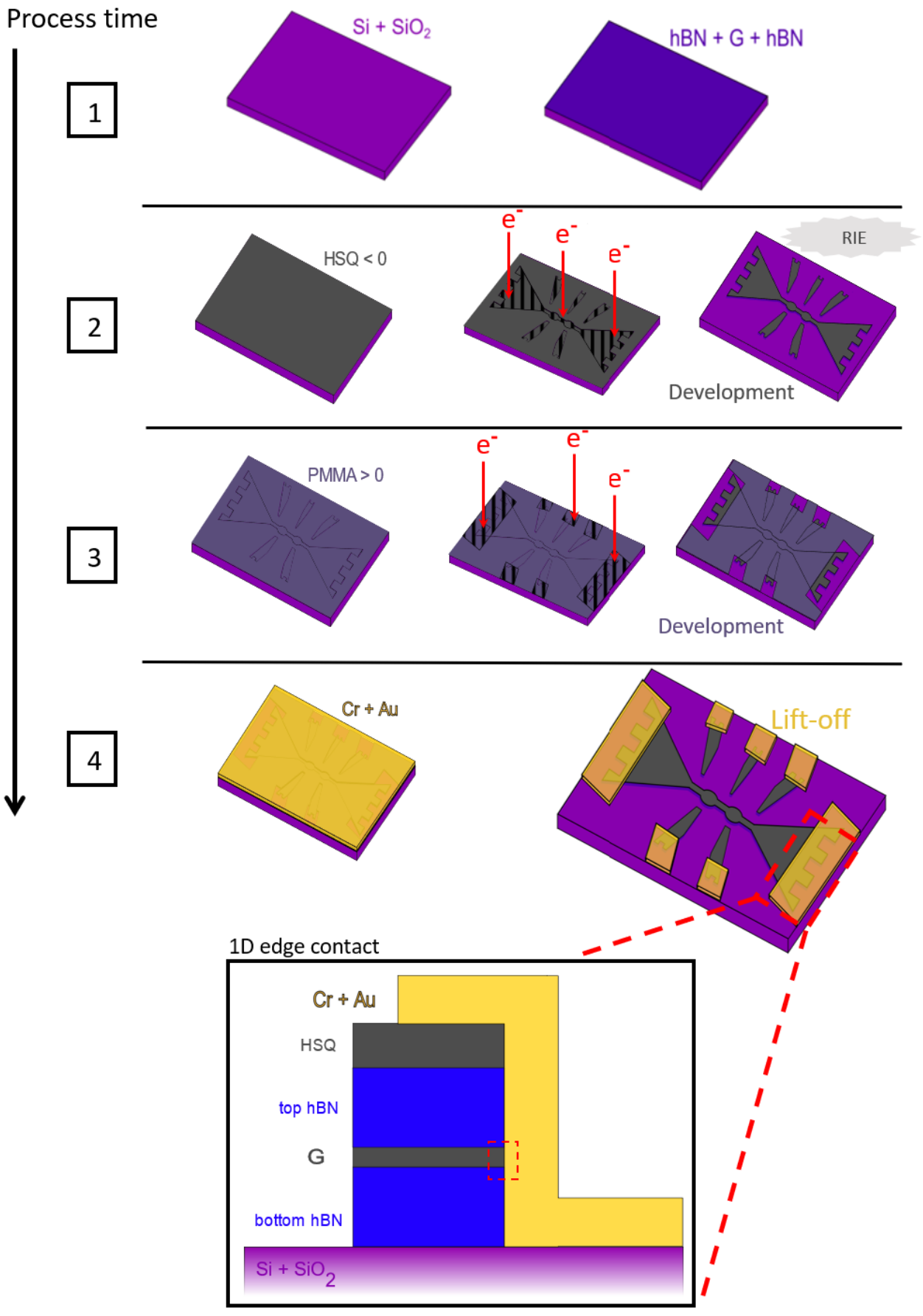

Figure 1.18: Main steps in the novel nanofabrication process for devices based on double GQD in a single-electron transistor configuration that we develop as part of this thesis work.

Bibliography

[1] Kostya S Novoselov et al. “Electric field effect in atomically thin carbon films”. *science*, 306, 5696, pp. 666–669, 2004.

[2] Lei Wang et al. “Negligible Environmental Sensitivity of Graphene in a Hexagonal Boron Nitride/Graphene/h-BN Sandwich Structure”. *ACS Nano*, 6, 10. PMID: 23009029, pp. 9314–9319, 2012.

[3] Romaine Kerjouan. “Rayonnement synchrotron THz dans le graphene ondulé”. s208475. PhD thesis. 2022, 2022.

[4] Xuesong Li et al. “Large-Area Synthesis of High-Quality and Uniform Graphene Films on Copper Foils”. *Science*, 324, 5932, pp. 1312–1314, 2009.

[5] J. Hass et al. “Highly ordered graphene for two dimensional electronics”. *Applied Physics Letters*, 89, 14, p. 143106, 2006.

[6] Alok Ranjan et al. “Dielectric Breakdown in Single-Crystal Hexagonal Boron Nitride”. *ACS Applied Electronic Materials*, 3, 8, pp. 3547–3554, 2021.

[7] Luca Banszerus et al. “Ballistic Transport Exceeding 28 m in CVD Grown Graphene”. *Nano Letters*, 16, 2. PMID: 26761190, pp. 1387–1391, 2016.

[8] L. Wang et al. “One-dimensional electrical contact to a two-dimensional material”. English (US). *Science*, 342, 6158, pp. 614–617, 2013.

[9] D. Purdie et al. “Cleaning Interfaces in Layered Materials Heterostructures”. *Nature Communications*, 9, 2018.

[10] Kenji Watanabe, Takashi Taniguchi, and Hisao Kanda. “Direct-bandgap properties and evidence for ultraviolet lasing of hexagonal boron nitride single crystal”. *Nature materials*, 3, 6, pp. 404–409, 2004.

[11] Kenji Watanabe, Takashi Taniguchi, and Hisao Kanda. “Ultraviolet luminescence spectra of boron nitride single crystals grown under high pressure and high temperature”. *physica status solidi (a)*, 201, 11, pp. 2561–2565, 2004.

[12] A. C. Ferrari et al. “Raman Spectrum of Graphene and Graphene Layers”. *Phys. Rev. Lett.*, 97, p. 187401, 2006.

[13] Andrea Ferrari and Denis Basko. “Raman spectroscopy as a versatile tool for studying the properties of graphene”. *Nature nanotechnology*, 8, pp. 235–46, 2013.

[14] Felix Herziger et al. “Two-Dimensional Analysis of the Double-Resonant 2D Raman Mode in Bilayer Graphene”. *Phys. Rev. Lett.*, 113, p. 187401, 2014.

[15] L. G. Cançado et al. “Quantifying Defects in Graphene via Raman Spectroscopy at Different Excitation Energies”. *Nano Letters*, 11, 8. PMID: 21696186, pp. 3190–3196, 2011.

[16] R. Geick, C. H. Perry, and G. Rupprecht. “Normal Modes in Hexagonal Boron Nitride”. *Phys. Rev.*, 146, pp. 543–547, 1966.

[17] DisChem. *SurPass 3000 Microlithography Adhesion Promoter technical data sheet*. 2020. URL: `https://apps.mnc.umn.edu/archive/ebpgwiki/rsrc/EBPG/Datasheets/surpass3000_datasheet.pdf`, 2020.

[18] Wilfried Erfurth, Andrew Thompson, and Nezih Ünal. "Electron dose reduction through improved adhesion by cationic organic material with HSQ resist on an InGaAs multilayer system on GaAs substrate". *Advances in Resist Materials and Processing Technology XXX*. Vol. 8682. SPIE. 2013, pp. 513–519, 2013.

[19] András Vladár and Michael Postek. "Electron Beam-Induced Sample Contamination in the SEM". *Microscopy and microanalysis : the official journal of Microscopy Society of America, Microbeam Analysis Society, Microscopical Society of Canada*, 11, pp. 764–765, 2005.

[20] Dachuang Shi et al. "Anisotropic Charge Transport Enabling High-Throughput and High-Aspect-Ratio Wet Etching of Silicon Carbide". *Small Methods*, 6, 8, p. 2200329, 2022.

[21] Salvador Barraza-Lopez et al. "Effects of Metallic Contacts on Electron Transport through Graphene". *Phys. Rev. Lett.*, 104, p. 076807, 2010.

[22] G. Giovannetti et al. "Doping Graphene with Metal Contacts". *Phys. Rev. Lett.*, 101, p. 026803, 2008.

[23] François Léonard and A. Talin. "Electrical contacts to one- and two-dimensional nanomaterials". *Nature nanotechnology*, 6, pp. 773–83, 2011.

[24] Fengnian Xia et al. "The origins and limits of metal-graphene junction resistance". *Nature nanotechnology*, 6, 3, pp. 179–184, 2011.

[25] Tao Chu and Zhihong Chen. "Understanding the Electrical Impact of Edge Contacts in Few-Layer Graphene". *ACS Nano*, 8, 4. PMID: 24593155, pp. 3584–3589, 2014.

[26] Sungwon Lee et al. "Contact Resistivity in Edge-Contacted Graphene Field Effect Transistors". *Advanced Electronic Materials*, 8, 5, p. 2101169, 2022.

[27] K. Nagashio et al. "Contact resistivity and current flow path at metal/graphene contact". *Applied Physics Letters*, 97, 14, p. 143514, 2010.

[28] Joshua T. Smith et al. "Reducing Contact Resistance in Graphene Devices through Contact Area Patterning". *ACS Nano*, 7, 4. PMID: 23473291, pp. 3661–3667, 2013.

[29] Bernhard Kretz et al. "Atomistic Insight into the Formation of Metal-Graphene One-Dimensional Contacts". *Phys. Rev. Appl.*, 10, p. 024016, 2018.

[30] Rabih Zaouk, Benjamin Park, and Marc Madou. "Introduction to Microfabrication Techniques". *Methods in molecular biology (Clifton, N.J.)*, 321, pp. 5–15, 2006.

[31] Giovanni Marin. *Inclined lithography and photoresist optimization for fabrication of 3D mesh structures*. Master's thesis. Dec. 2014, 2014.

[32] MicroChemicals. *Lift-off Processes with Photoresists*. `https://research.engineering.ucdavis.edu/cnm2/wpcontent/uploads/sites/11/2014/07/lift_off_photoresist.pdf`. 2009-12-15, 2009-12-15.

Chapter 2

Double GQD as a two-level system in the THz spectral range

In the first chapter of this thesis, we have detailed the fabrication process of a high-quality device based on a double graphene quantum dot. Quantum dots are promising devices for the development of quantum devices but are very few explored in the THz range. A main reason is the huge difference of scale between the typical size of the quantum dot (< 100 nm) and the wavelength (300 μm at 1 THz), making very challenging to probe characteristics of quantum dot in this spectral region. A main objective of this PhD work is to evaluate the potential of double graphene quantum dot to act as a two-level system in the THz spectral range and anticipate further experiments exploring THz light-matter interaction from weak to ultra-strong coupling regime.

In this chapter, we characterize and analyze the properties of the double graphene quantum dot based devices. The first part describes the state of the art of quantum dots in the THz spectral range. The second part presents the optical properties of graphene quantum dots in the THz spectral range and their THz quantum response. Finally, the third part presents dark transport spectroscopy measurements and analysis of the double graphene quantum dot based device. We use dark transport spectroscopy as a tool to probe the two-level system and quantify its resonant frequency.

2.1 Quantum dots in the THz spectral range

Technologies based on bulk (3D) semiconductors have been extensively developed for over half a century now, starting from the first handmade transistor in 1947 to the automated manufacture of millions of transistors on a single millimeter-sized chip. The energy dispersion in bulk semiconductors is continuous, allowing for efficient electron transport and device operation at macroscopic scales. However, the continuous energy spectrum limits the ability to control individual quantum states, explore quantum coherent effects, and tailor electronic properties at the nanoscale. In contrast, quantum dots represent a paradigm shift in semiconductor technology [1]. These nanoscale structures confine electrons in all three dimensions and the quantum confinement effects result in discrete energy levels [2, 3], as in an isolated atom. Thus, quantum dots are often referred to as 'artificial atoms'. Quantum dots have unique characteristics that are very attractive for fundamental and applied research. Indeed, discrete energy levels and

the ability of designing their distribution through the size, edge and general shape of quantum dots [4] allow their electronic and optical properties to be engineered, making quantum dots versatile and flexible. These features enable the development of quantum dot-based devices with advanced functionalities, such as single-electron transistors, quantum computing building blocks and tunable optoelectronic devices. Also, the confinement of electrons in quantum dots enhances their coherence time and reduce their coupling to their environment, paving the way for coherent manipulation and coherent coupling to other quantum systems, which is essential for quantum technology applications. Moreover, miniaturized and integrated solutions with existing semiconductor technology are available. In addition, quantum dots provide a means of exploring the quantum interaction of light with matter, which is essential for furthering understanding of fundamental physics and developing applications in electronic, photonic, optoelectronic and quantum technologies.

Therefore, quantum dots have been widely studied over the years in various topics, and are currently used in domains that impact our everyday life [5]. For example, they are used in biology to improve the resolution of cell imaging [6], in medicine for research into cancer treatment [7], in the display industry with LED display technologies [8] offering a better color range and higher brightness, in the energy field to improve battery efficiency [9], and, of course, in quantum technologies. Quantum dots are composed of various material systems. The first quantum dots in the end 80's were synthesized with CuCl. More than 40 years later, quantum dots based on Cd, In, Ga, As, Zn, Pb, or Si have been studied. The choice of their component depends on the application and the desired optical and electronic properties. There are two main methods for fabricating quantum dots: bottom-up and top-down techniques. The former starts from the bottom, i.e., atoms or molecules, to synthesize quantum-sized materials through chemical interactions, while the latter involves tailoring bulk materials into quantum-sized materials by breaking their internal chemical bonds.

In quantum dots, the bandgap energy is the sum of the bandgap of the bulk material, the confinement energy of the electron and hole, and the Coulombic attraction between the hole and electron. Regarding the energy spacing between the discrete energy levels of a quantum dot, smaller quantum dots feature a larger separation between energy levels due to greater electronic confinement. For the visible and infrared range, quantum dots made of III-V, II-VI, IV-IV and IV-VI semiconductors with a typical diameter of a few nanometers are used, as the separation of energy levels and the band gap is of the order of eV. To reach the THz spectral range, the energy level spacings and band gaps should be reduced to a few meV. Such low energy level separations are possible with large quantum dots, typically around a hundred nanometers in diameter. In addition, the use of semiconductor materials limits the band gap of the quantum dot to large values. Therefore, semi-metals are candidates of choice to cover the THz spectral range. Quantum dots with spectral features in the THz spectral range remain largely unexplored today, due to several technological and instrumental challenges associated with the very low energy of THz photons and the large scale difference between the optical wavelength (300 μm at 1 THz) and the dimensions of the quantum dot ($\sim$ 100 nm). The main developments of quantum dots at THz frequencies reported so far are HgTe nanocrystals and graphene quantum dots, which we will present in the next sections.

2.1.1 HgTe quantum dots

Large quantum dots (Nanocrystals) of mercury telluride (HgTe), a semi-metal in its bulk form, have recently attracted considerable interest for the development of novel THz devices. This interest follows the work of Goubet *et al.*, who developed a high-temperature bottom-up method to increase the size of HgTe NCs, thereby extending their absorption from infrared range to 200 µm (i.e., 1.5 THz) [10], as illustrated in Fig. 2.1a). My thesis group, in collaboration with E. Lhuillier (INSP), has recently demonstrated a broad resonant absorption of large HgTe quantum dots in the THz frequency range, centered at $\sim$ 4.5 THz [11], as shown in Fig. 2.1b). This broad absorption is fully described by multiple intra-band transitions of single carriers between quantized states. The carrier recombination times in these HgTe quantum dots are $\sim$ 6 ps, a promising features for applications in THz light emission and detection (see Fig. 2.1c). The potential of these large HgTe quantum dots as THz emitters was also revealed by the demonstration of coherent THz emission from HgTe quantum dots under femtosecond optical excitation (see Fig. 2.1d) resulting from second-order nonlinear processes that are the photo-galvanic and photon-drag effects [12].

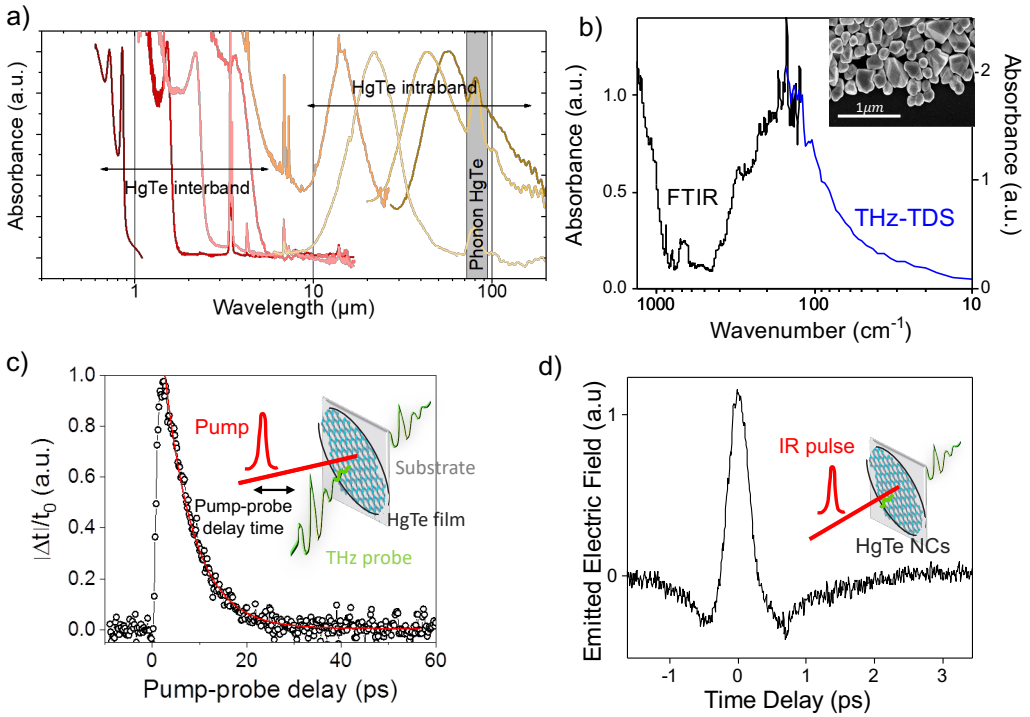

Figure 2.1: (**a**) Absorption spectra of undoped HgTe NCs and doped HgTe NCs are shown for different sizes, highlighting the extreme tunability of this material, from Ref. [10]. (**b**) Experimental intraband absorption of large HgTe quantum dots obtained from THz-TDS and FTIR measurements. Inset : SEM image. (**c**) Pump-probe measurements of the non-equilibrium carrier dynamics in large HgTe quantum dots. (**d**) Temporal waveform of the emitted THz field from HgTe quantum dots excited by femtosecond infrared pulses.

2.1.2 Graphene quantum dots

As a semi-metal, graphene is also very attractive for the development of quantum dots in the THz spectral range. One of the main advantages of this nanomaterial system is the possibility of fabricating graphene quantum dots of controlled size and shape using top-down techniques. Although previous studies on graphene quantum dots at THz frequencies are limited, some striking results have been reported. El Fatimi *et al.* demonstrated high-performance THz detectors made of quantum dots based on epitaxial graphene [13, 14]. The detection mechanism was relying on the bolometric effect, i.e. the increase in tunnel current through a quantum dot due to THz light absorption and electron temperature rise (see Fig. 2.2a and b). In addition, my thesis group recently demonstrated ultrasensitive THz photoresponse from a single hBN-encapsulated graphene quantum dot relying photogating effects [15] (see Fig. 2.2c). The device structure based on a single electron transistor in Coulomb blokade regime is shown in Fig. 2.2d).

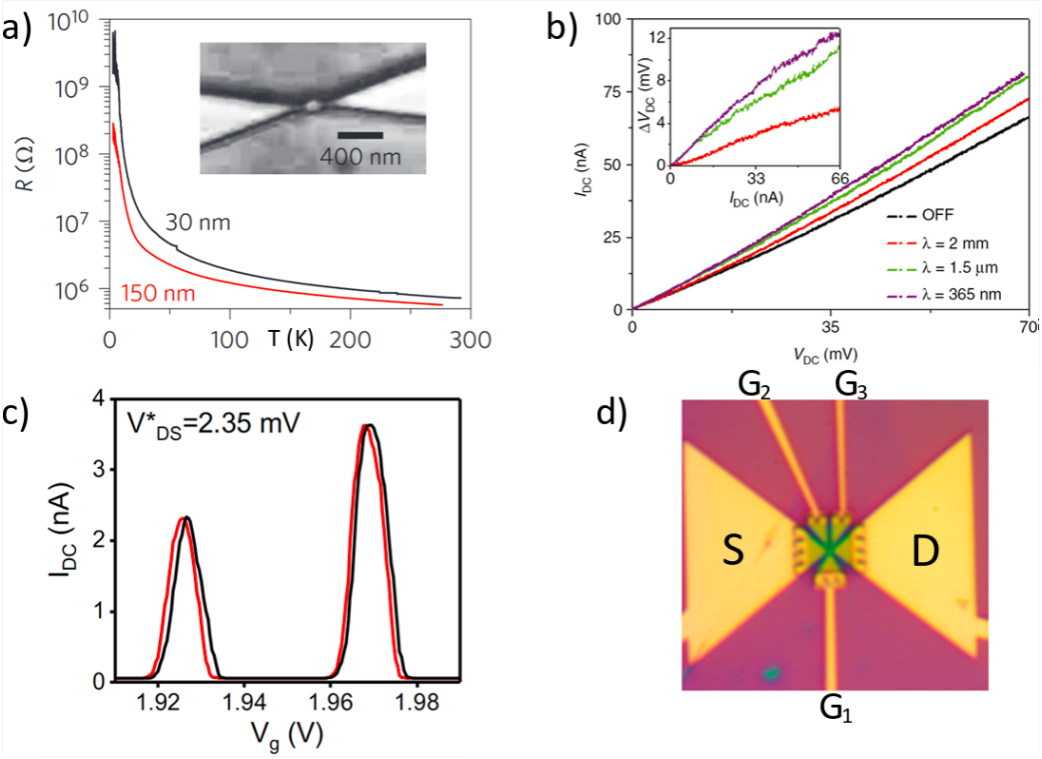

Figure 2.2: (**a**) DC resistance of graphene quantum dot device versus temperature for two dot diameters. Inset: SEM picture of the 150 nm epitaxied graphene quantum dot based device. Reproduced from [14]. **b**) DC I-V characteristics without (black) and with illumination on the graphene quantum dot sample for different wavelengths. Inset: Voltage drop as the illumination is turned on versus tunneling current. Reproduced from [14]. (**c**) Coulomb peak shift due to photogating effect in a single electron transistor based on a single graphene quantum dot. Black curve is without and red curve is with THz illumination. Reproduced from [15]. (**d**) Optical microscope picture of the single electron transistor device from [15]. The yellow area are the gold electrodes, purple is the Si/SiO2 substrate and the center green part is the hBN-graphene heterostructure.

These previous works on THz light coupling to graphene quantum dots have involved only classical interactions. In the next section, we will present the studies in the quantum regime,

starting with the calculation of the optical absorption at THz frequencies of large graphene quantum dots and their interaction with THz photons.

2.2 Optical properties of graphene quantum dots at THz frequencies

In this section, we introduce graphene and its peculiar linear band structure at low energy, and then describe the structural and electronic properties of large circular graphene quantum dots (QDs). Finally, we show the absorption spectra of large GQDs that highlight their potential for THz technology.

2.2.1 Basics on electronic properties of monolayer graphene

Graphene is a 2D material composed by carbon atoms arranged in a honeycomb lattice as represented in Fig.2.3a. Carbons atoms have 4 valence electrons. Three of them form σ-bonds with neighboring atoms and are responsible for the mechanical properties of graphene. The remaining electron occupies a p_z orbital, which is oriented perpendicular to the plane, and forms weaker π-bonds. The only electrons contributing to the electronic properties of graphene are those in the π-bonds. They are delocalized over the whole graphene sheet, which enables a high electronic mobility.

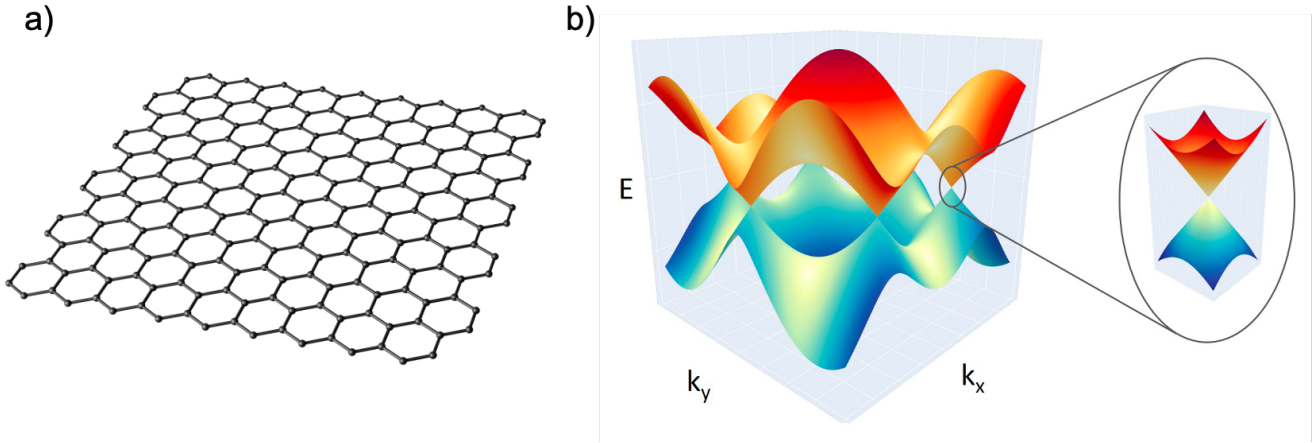

Figure 2.3: (**a**) Representation of hexagonal honeycomb lattice of graphene. (**b**) Graphene band structure within the nearest neighbour tight-binding model plotted within the first Brillouin zone.

The electronic properties are captured by a tight binding Hamiltonian, with electrons hoping between nearest neighbor :

$$H = -t_{Gra} \sum_{<i,j>} c_i^{\dagger} c_j + h.c \tag{2.1}$$

Where t_{Gra} describes the hoping rate between nearest neighbors atoms i, j, and $c_i\dagger, c_i$ are creation and annihilation operators. Using the tight-binding approximation, it is possible to derive the dispersion relation of a graphene monolayer, which writes [16] :

$$E_{\pm}(\mathbf{k}) = \pm t\sqrt{1 + 4\cos\left(\frac{\sqrt{3}k_y a}{2}\right)\cos\left(\frac{k_x a}{2}\right) + 4\cos^2\left(\frac{k_x a}{2}\right)} \tag{2.2}$$

with $t \approx 2.\text{eV}$ is the transfer integral between first neighbors p_z-orbitals, $a = \sqrt{3}a_{CC}$ and $a_{CC} = 0.142$ nm the carbon-carbon distance in graphene. The band structure of graphene is plotted in Fig.2.3. Like usual semiconductors, the band structure is mainly separated in two bands. The lower energy one corresponds to the valence band and the higher energy one to the conduction band. Both bands are symmetrical with respect to E=0 eV, where they touch each other at six points: **K**, **K'**, and the equivalent points obtained by $2\pi/3$-rotations. These 6 contact points are called the Dirac points.

In neutral graphene, the Fermi energy, E_F, lies exactly at the Dirac points since each atom brings one electron, and each level is spin degenerated. Thus, the valence band is full and the conduction band is empty at T = 0 K and no carrier is able to take part in the charge transport even though there is no energy gap between the bands. Therefore, the graphene is often described as a semimetal or as a gapless semiconductor. It is interesting to expend the Equation 2.2 in the vicinity of the points **K** and **K'**:

$$\mathbf{K}/\mathbf{K'} = \frac{4\pi}{3a}(\eta, 0) \text{ with } \eta = 1(-1) \text{ for } \mathbf{K}(\mathbf{K'}) \tag{2.3}$$

The first order development in $\mathbf{k}$ gives :

$$E_{\pm}(\mathbf{q}) = \pm\hbar v_f|\mathbf{q}| \tag{2.4}$$

where $\mathbf{q} = \mathbf{k} - \mathbf{K}(\mathbf{K'})$ and $v_f = \frac{\sqrt{3}ta}{2\hbar} \approx 10^6 \text{m.s}^{-1}$ is defined and referred to as the Fermi velocity. One can note that the dispersion relation in Equation 2.4 is linear in $\mathbf{q}$ in contrast with the usual parabolic dispersion relations of semiconductors. The low-energy band structure is then conical around the Dirac points, and is often referred to as the Dirac cones. From the computation of the density of states per unit area, it is possible to derive the charge carrier density n in graphene given by:

$$n = \frac{1}{\pi}\left(\frac{E_F}{\hbar v_F}\right)^2 \tag{2.5}$$

n is usually expressed in cm^{-2} and referred to as doping. The charge neutrality is reached when n=0, which corresponds to the energy level of the Dirac points (E=0). By applying a gate voltage, it is possible to control the Fermi energy and tune the carrier density over large range. Such electric field effect in graphene could be very practical in our context as the interaction between graphene and THz photons strongly depends on the doping level, enabling to control the strength of optical transitions through electrical gating.

2.2.2 Electronic energy states of graphene quantum dots

By reducing the dimensions of the graphene layer, the graphene dispersion relation can be shaped due to the additional spatial confinement of the carriers. The spatial confinement of carriers in both directions of the plane of the graphene sheet leads to graphene quantum dots,

whose energy spectra are described in this section.

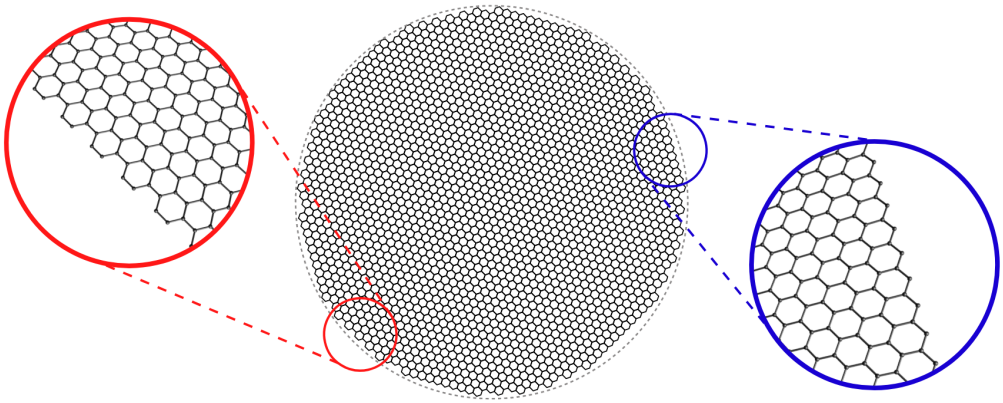

Figure 2.4: Schematic representation of a circular graphene quantum dot. Red inset exhibits an armchair edge configuration, and blue inset a zigzag edge configuration.

A circular graphene quantum dot (QD) with a radius R can be modeled as a quantum well in a 2D space exhibiting circular symmetry (see Fig. 2.4). This system can be described by a continuous wavefunction $\Psi(\vec{r})$, and the low-energy Hamiltonian reduces to the Dirac Hamiltonian form [17]:

$$H = \hbar v_F \begin{pmatrix} 0 & -i\left(\frac{\partial}{\partial x} + i\frac{\partial}{\partial y}\right) \\ -i\left(\frac{\partial}{\partial x} - i\frac{\partial}{\partial y}\right) & 0 \end{pmatrix} \tag{2.6}$$

and

$$\Psi(\vec{r}) = \begin{pmatrix} A(\vec{r}) \\ B(\vec{r}) \end{pmatrix} \tag{2.7}$$

Here, $\Psi(\vec{r})$ is a two-component vector representing the two atoms A and B in the graphene unit cell. The eigenvalue equation for the Dirac Hamiltonian, which determines the state energy E is a straightforward differential equation :

$$\Delta A(\vec{r}) = -\left(\frac{E}{\hbar v_F}\right)^2 A(\vec{r}) \tag{2.8}$$

Due to the circular symmetry, we can assume a specific form for the function $A(r, \varphi)$:

$$A(r, \varphi) = a(r)e^{im\varphi} \tag{2.9}$$

The periodic angular dependence requires that m be an integer, representing the angular momentum quantum number. The solutions for the radial part $a(r)$ are then given by the m-th Bessel function of the first kind:

$$a(r) = J_m\left(\frac{Er}{\hbar v_F}\right) \tag{2.10}$$

Quantum confinement effects arise from boundary conditions applied to the wavefunction. At the edge of the graphene QD, we have:

$$a(r = R) = J_m\left(\frac{ER}{\hbar v_F}\right) = 0 \tag{2.11}$$

This boundary condition leads to the quantization of the energy spectrum, allowing us to determine the possible eigenvalues of the system E_m:

$$E_m = \frac{\hbar v_F \theta_1^m}{R} \tag{2.12}$$

where θ_1^m is the first zero of the m-th Bessel function of the first kind J_m. This energy spectrum as a function of the graphene QD radius is illustrated in Fig. 2.5. The simple $\frac{1}{R}$ dependence is derived from a quick estimation of the linear dispersion relation quantized due to the discrete wavevector $k_n \sim \frac{n\pi}{R}$ where n is an integer.

The energy levels estimated using this continuous wavefunction model indicate that large graphene QDs, typically in the range of 100 nm, are suitable candidates for THz technologies due to their energy level spacing in the THz range. For instance, the energy level spacing for a 50 nm radius graphene QD is approximately 17 meV, which corresponds to ∼4 THz.

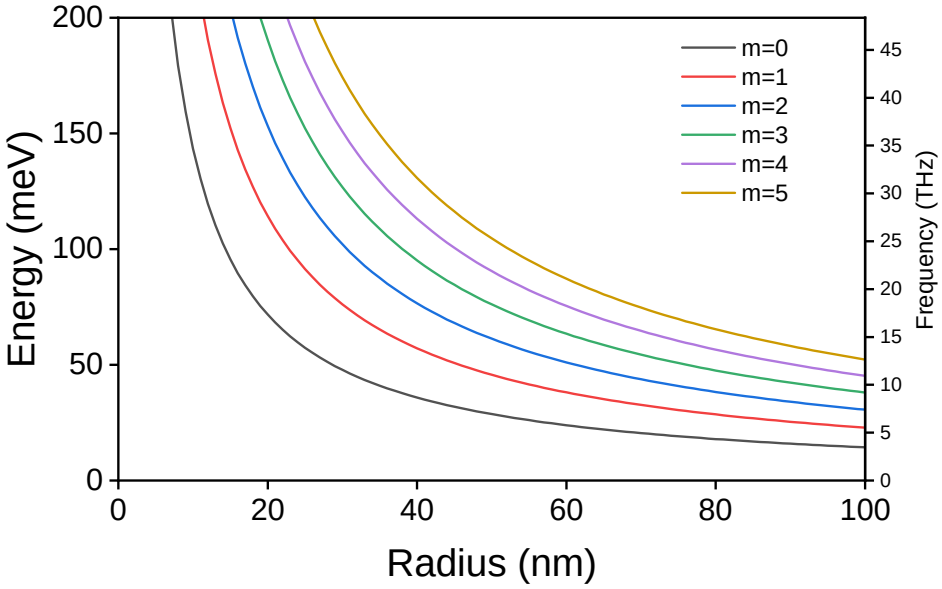

Figure 2.5: Eingenvalues E_m as function of radius from Equation 2.12 with increasing angular momentum m from bottom to top.

The continuous model discussed earlier addresses the influence of the finite size of the graphene QD on the infinite graphene band structure but fails to consider the microscopic structure of the graphene QD, particularly the significant edge effects. The edge configuration of a graphene QD, whether armchair, zigzag (as illustrated in Fig. 2.4), or disordered, significantly impacts the electronic structure of energy states near the Dirac point, or close to zero energy [18]. To accurately capture the contribution of edge effects on electronic energy states, S. Massabeau reports in his PhD thesis [4] the calculation of the GQD energy spectrum of circular graphene QDs via direct numerical diagonalization of the tight-binding Hamiltonian described in Eq. 2.1.

However, this method is extremely computationally intensive since the Hamiltonian matrix is of size N × N, where N represents the number of carbon atoms in the graphene QD. Consequently, the maximum radius studied was limited to 25 nm. Fig.2.6 presents the energy spectra obtained for radii of the graphene QD ranging from 17 nm to 25 nm. We observe a complex dispersion of energy levels. The colors of the states correspond to the spatial extension of their wavefunctions, leading to the classification under three relevant categories : edge states, mixed states and bulk states. The higher energy states, or bulk states, follow the energy evolution predicted by Eq. 2.12 (dashed lines in Fig. 2.6) for m=1 and m=2, closely aligning with the continuous model's predictions and exhibit smooth, large lobes predominantly away from the graphene QD edges, consistent with the boundary conditions in Eq. 2.12. However, the spectra also include many low energy states: edge states near the Dirac point and mixed states that lie between edge and bulk states. The lower energy states, the edge states, are mainly localized at the graphene QD borders and are supposed to result from the complex coupling of localized orbitals. At intermediate energy lie the mixed states, which are also localized at the graphene QD edge but with a notable electronic density at the center of the dot.

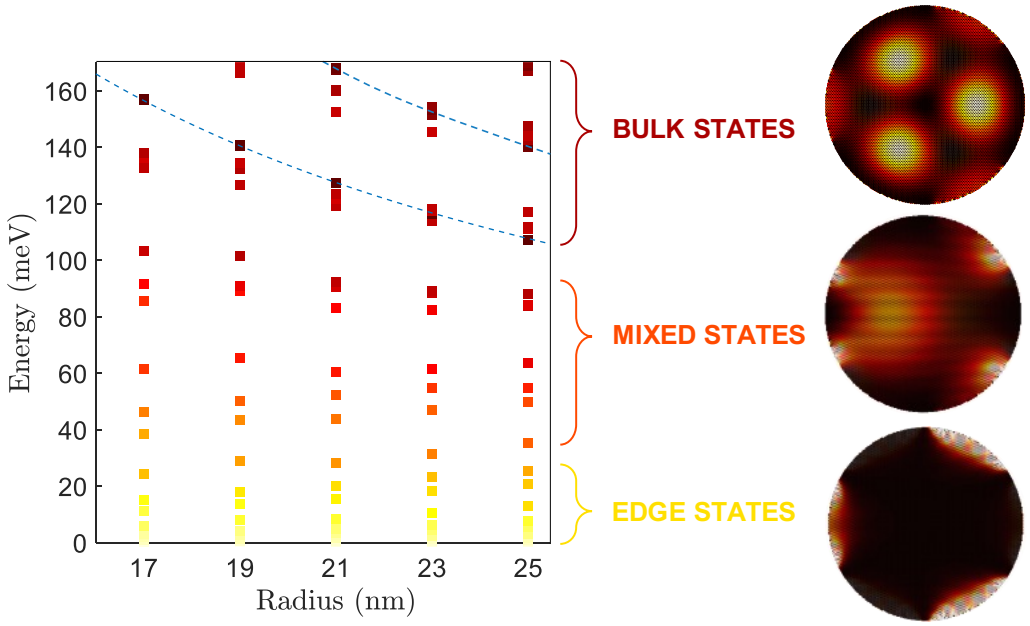

Figure 2.6: Energy spectra of graphene QDs as function of their radius obtained from direct diagonalization of the tight-binding Hamiltonian. The color scale describes the spatial extension of the wavefunctions, from yellow (localised on the edge) to dark red (localised at the center). The electronic states can be classified into three categories : Bulk, Edge and Mixed States. Typical wavefunction density profiles for each type are depicted on the right. Dashed lines corresponds to the eigenvalues for m=1 and m=2 from Equation 2.12. Adpated from [4]

2.2.3 Absorption spectra of graphene quantum dots

With the electronic states identified, calculation including the dipole interaction potential as a perturbation can predict the coupling of electronic transitions between these electronic states and low-energy photons, thereby determining the optical properties of graphene QDs at THz frequencies. The absorption is computed from the dipolar interaction Hamiltonian $H_I = \frac{e}{c}\vec{P}\cdot\vec{A}$,

where $\vec{P}$ is the impulsion operator and $\vec{A}$ the vector potential of a plane wave at normal incidence. The dependence of the graphene QD absorption properties on their size is illustrated in Fig. 2.7a, which shows the absorption cross-section of a graphene QD, normalized by its surface area, for various radii and a doping value of E_F=200 meV. The principal transitions involved in the absorption resonance are between successive energy states, indicating intraband transitions, while interband transitions have larger transition energies and weaker absorption contributions. The absorption spectra exhibit an intense peak with a center frequency scaling like $\frac{1}{R}$ (see Fig. 2.7b). This broad resonant absorption demonstrates the quantization of electronic energy levels in graphene QDs, unlike infinite graphene, which shows a distinct tendancy from THz to visible range [19].

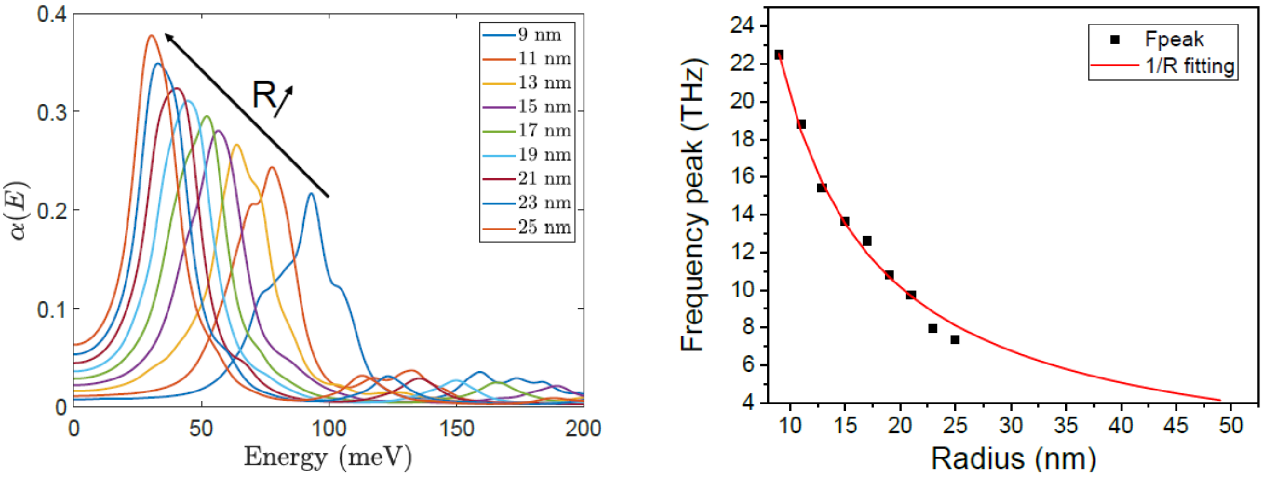

(a) (b)

Figure 2.7: **(a)** Theoretical absorption spectra of a circular graphene QD with a chemical potential of 200 meV for various radii. **(b)** Frequency of the absorption maximum from fitting of theoretical curves in (a). Adapted from [4].

2.2.4 THz quantum response of a graphene quantum dot

The experimental and theoretical study of the interaction of THz photons with a graphene quantum dot in the quantum regime was first reported by S. Messelot and *al.*, PhD student in my group. We will describe here the main results obtained [20].

For this study, a single-electron transistor based on an exfoliated graphene monolayer encapsulated by two hexagonal boron nitride (hBN) layers was fabricated in the LPENS clean room, by E. Ricardi. The device consists of a large graphene QD of 120 nm diameter, connected to electron reservoirs (source and drain electrodes) via two narrow constrictions (40 nm width) that act as tunneling barriers, as presented in Fig. 2.8. PG gate eletrodes enables to control the chemical potential of the quantum dot and G1 and G2 gate electrodes the tunneling rates of the barriers (constrictions). If the tunneling rate to the electron reservoirs is small enough, the electronic lifetime in the quantum dot can become higher than the inverse energy level spacing, the conduction enters the sequential tunneling or Coulomb blockade regime, where electrons can only tunnel one-by-one in and out of the quantum dot. At low source-drain bias, if the

energy levels of the GQD are not aligned with source and drain chemical potential, there is no possibility for conduction through the quantum dot. However, the absorption of a THz photon enables tunneling if its energy $h\nu$ matches the energy difference between the level of the QD and the chemical potential of the electrode chemical potential, see Fig. 2.8. This describes the photon assisted tunneling (PAT) that designate tunneling events enabled by photon absorption in a system in the Coulomb blockade regime. For fixed bias voltage, the photon energy that can promote PAT only depends on the energy difference between the QD level and the electrode chemical potential, tunable with gate voltage. Thus, during gate voltage scans, the PAT process causes satellite peaks to appear on either side of the DC Coulomb peak, as shown in Fig.2.8. Their position is given by the energy difference between the GQD energy level and the electrodes chemical potentials, hence the photon energy.

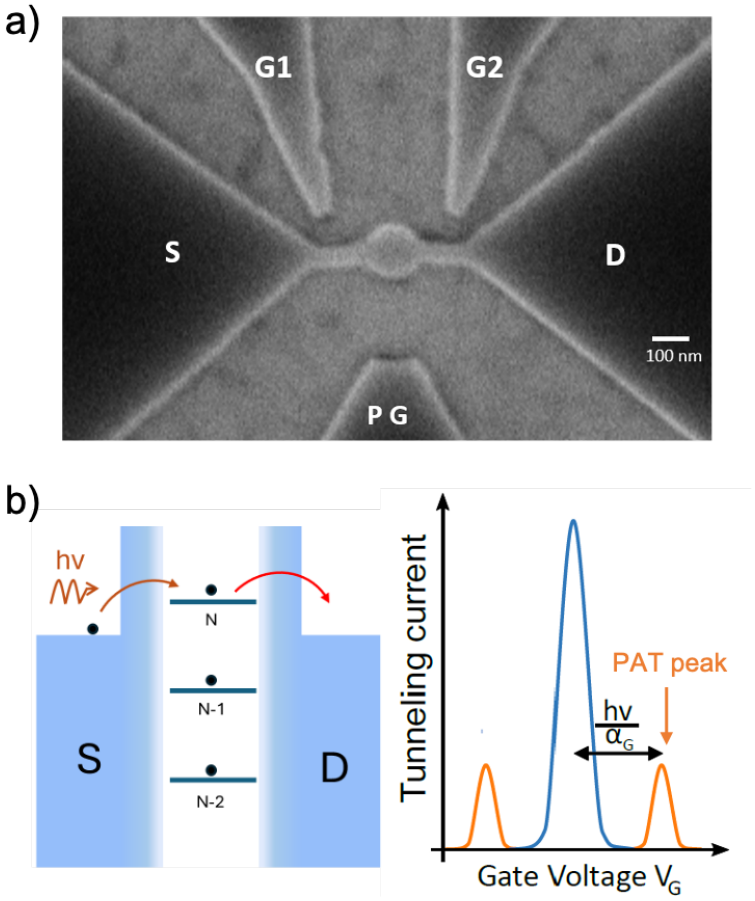

Figure 2.8: **(a)** SEM close up view of the GQD at the center, connected via narrow constrictions to source and drain electrodes, and surrounded by 3 gate electrodes G1, PG and G3.**(b)** Schematic illustration of PAT process. The electron cannot tunnel to the QD, unless if the absorbance of a THz photon with the required energy occurs (left). Schematic profile of the tunneling current through the QD under Thz illumination. Satellite peaks (orange) appear next to the main DC Coulomb peak (blue), shifted from the incoming photon energy (right).

Fig.2.9a reports the measured tunneling current as a function of gate voltage for V_{SD}=0.1 mV when the graphene single QD is illuminated by a coherent THz radiation with frequency ranging from 0.24 to 0.38 THz (color lines) and without illumination (black curve). We observe additional satellite peaks appear on the right side of the principal Coulomb peak under THz illumination. They also shift in positive gate voltage as the incoming wave frequency increases

(see Fig.2.9b). Converting the gate voltage shift in energy unit using the gate lever-arm reveals that the gate voltage shift matches the energy of the THz photons. This is a signature of PAT process [21, 22]. Quantitative analysis of the satellite peaks was performed to extract the intensity dependence of the amplitude of the modulation of the chemical potentials of the electrodes induced by the incoming THz wave, V_{THz}, as reported in Fig. 2.9c. As, V_{THz} characterises the interaction strength of the graphene single QD with the incident THz wave, from this study, the electric dipole moment length d of the graphene QD, given by this relation $V_{THz} = E_{THz}.d$, was estimated. An average THz electric dipole moment length as large as $d \approx 230nm$ was demonstrated. Such large THz electric dipole for a quantum system that involves single-electron tunneling is suitable for future quantum optics experiments using graphene quantum dots strongly coupled to a THz resonator.

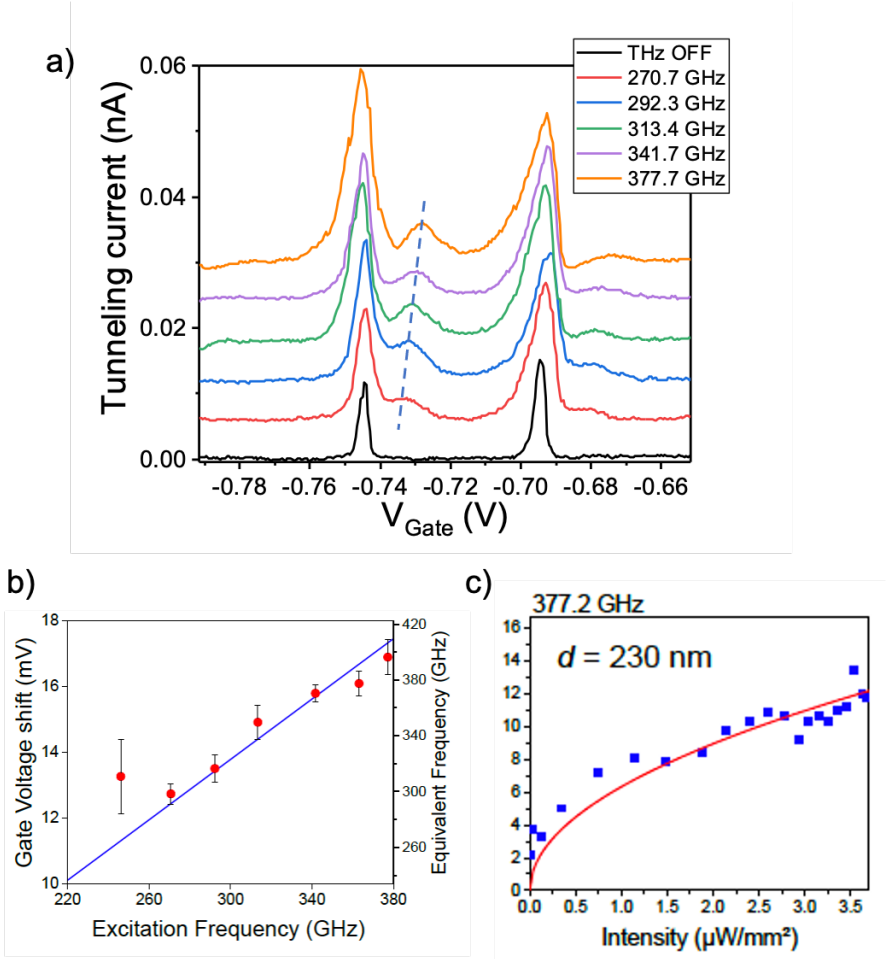

Figure 2.9: **(a)** Source-drain current vs gate voltage observed without (black curve) and with THz radiation at several frequencies (color curves). The curves are offset for clarity. The dashed lines show positions of satellite peaks due to PAT process. **(b)** Energy spacing between the original DC Coulomb peak and its associated satellite peak as a function of the photon frequency. The right scale indicate the gate voltage shift in equivalent frequency. The blue is a linear fit with a slope in frequency of ≈1, indicating PAT process occurs. **(c)** THz intensity dependence of the amplitude V_{THz} at frequency 0.377 THz. The red line is a square root fit from which is deduced the indicated dipole moment length d.

2.3 Transport spectroscopy of graphene double quantum dots

Thanks to their large absorption in the THz spectral and their large interaction dipole with THz photons, graphene QDs are very promising nanomaterials for the development of THz quantum devices. To further evaluate the potential of graphene QDs for THz quantum technology, the aim of my thesis is to build a two-level system based on graphene QDs in the THz spectral range. Implementing a two-level system in the THz spectral range is a major current challenge for the development of THz quantum technologies, as two-level systems are building blocks for many quantum devices, such as single-photon sources, single-photon detectors and qubits. However, a two-level system at THz frequencies in condensed matter remains elusive so far. A double quantum dot (DQD) system is often considered more appropriate as a two-level system compared to a single quantum dot as in DQD system, the energy separation of the two-level system can be precisely controlled by adjusting the interdot coupling (tunnel coupling). Indeed, depending on the strength of the inter-dot coupling, the two dots can form ionic-like or covalent-like bonds. In the first case, the electrons are localized on individual dots, while in the second case, the electrons are delocalized over both dots. The covalent binding leads to a symmetric and anti-symmetric state, i.e. a two-level system, whose energy difference is proportional to the degree of tunneling. Multiple-gated structures for the DQD allow to independently control their energy levels, the coupling strength between the two QDs, as well as the tunneling rate to the leads. This tunability allows for a large manipulation of the two levels, which is essential for many applications such as quantum computing and for coupling the DQD to a resonator for quantum electrodynamics in cavity. Also, the DQD system offers more flexibility in creating and controlling different charge and spin configurations, which can be used to encode and manipulate the two-level system as qubits. These features make DQDs a robust and versatile platform for quantum technology.

In the following sections, we will present the study of quantum transport in a graphene DQD that we have carried out using dark transport spectroscopy measurements at low temperature. First, we start by introducing the basics of transport in quantum dots.

2.3.1 Basics on transport in quantum dots

Quantum transport in a single quantum dot

As opposed to real atoms with properties determined by their intrinsic characteristics, quantum dots can be tuned and modeled as desired with design and DC voltages. The trapped electrons can be exchanged with the reservoirs, called source and drain, at a rate of $\Gamma_{S/D}$; the reservoirs being modelled as Fermi seas with electrochemical potentials $\mu_{S/D}$ that can be tuned by applying a voltage. The quantum dot's potential $\mu_{dot}(N)$ can be tuned the same way through a capacitive coupled plunger gate. If the tunneling rate to the reservoirs is small enough, the conduction enters the sequential tunneling, or Coulomb blockade regime where, due to Coulomb repulsion, the electrons tunnel one-by-one in and out the QD (see Fig. 2.10). The total energy of the N

electrons filled QD is a combination of non-interacting and electrostatic interactive terms :

$$E(N) = \sum_{n=1}^{N} \epsilon_n^{(0)} + \frac{e^2N^2}{2C_\Sigma} + eN\frac{C_gV_G + C_SV_S + C_DV_D}{C_\Sigma} \tag{2.13}$$

where $\epsilon_n^{(0)}$ is the single-particle energy level spectrum, C_Σ the total capacitance of the QD, defined by $C_\Sigma = C_G+C_S+C_D$ with C_G is the capacitance from the QD to its local gate and $C_{S/D}$ the capacitance from the QD to source/drain leads as schematized on Fig.2.10b. The energy required to add the N-th electron in the dot is the chemical potential $\mu_{dot}(N) = E(N)-E(N-1)$ and the energy cost for adding one electron, E_{add}, is therefore :

$$\begin{aligned} E_{add} &= \mu_{dot}(N) - \mu_{dot}(N-1) \\ &= \frac{e^2}{C} + \epsilon^{(0)}(N) - \epsilon^{(0)}(N-1) \\ &= E_C + \Delta E_{level} \end{aligned} \tag{2.14}$$

The addition energy is determined by two phenomena : the first one is due to Coulomb repulsion and electrostatic environment responsible of the charging energy $E_C = \frac{e^2}{C}$. The second one is due to the confinement in all directions and the quantization of the energy spectrum ΔE_{level}.

We now consider the possibility for a current to flow through the quantum dot. At $V_{DS} = 0$, μ_S=μ_D a tunneling transport occurs only if an empty single-energy level of the dot crosses $\mu_{S/D}$. As a consequence, a non-zero current can only be measured if the quantum dot chemical potential is aligned with source and drain chemical potentials. Consequently, when sweeping the chemical potential of the quantum dot levels using the gate voltage V_G, successive alignments with $\mu_{S/D}$ lead to successive current peaks (Coulomb peaks). By increasing V_{DS} such as $eV_{DS} < E_{add}$, an electron can tunnel from the drain to the quantum dot N electron state and then from the quantum dot to the source current if $\mu_{dot}(N)$ lies within the transport windows [μ_S,μ_D]. At V_{DS}=E_{add}, at least one state is within the transport window and a current can flow through the dot. The Coulomb blockade starts to be completely lifted when $eV_{DS} > E_{add}$. Charging energies and lever arms are the two quantities that electrostatically describe the circuit. When an extra electron enters the dot, $\mu(N)$ shifts by E_{add}. To determine the distance in gate voltage ΔV_g between two successive Coulomb peaks, the condition $\mu(N-1, V_g) = \mu(N, V_g+\Delta V_g)$ must be fulfilled, thus $\Delta V_g = \frac{C}{eC_g}E_{add}$. It is interesting to define $\alpha_g = \frac{C}{C_g}$ as the capacitive lever-arm of the gate. It may be understood as the coefficient factor linking gate voltage and associated energy, as $E_{add} = e\alpha_g\Delta V_g$.

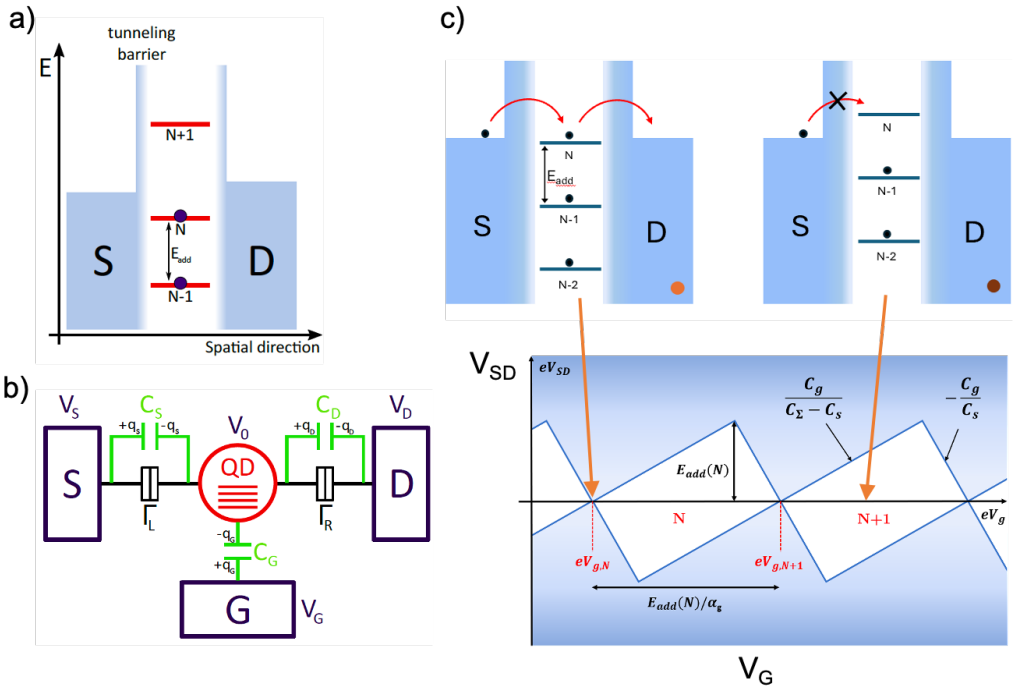

Figure 2.10: **(a)** Transport in single QD. Schematic energy diagram of a single electron transistor based on a single QD representing the quantum dot energy levels (red) between two Fermi sees or electron reservoirs, the source and drain electrodes (blue).**(b)** Schematic architecture of the single electron transistor (SET), here using a quantum dot as central island (red). Adapted from [23]. **(c)** Energy diagram of the QD based device in a non-conducting state and conducting state at zero bias (top) and schematic charge stability diagram of a quantum dot in the Coulomb blockade regime, depending on the gate voltage V_G and bias V_{DS}. The blue (white) areas denote the region where the electron transport is allowed (suppressed) through the dot (bottom).

Quantum transport in a double quantum dot

On the basis of this description of sequential tunneling current in a single QD, we now turn to the basics of transport in a double QD (DQD). When two QDs are close enough for electrons to jump from one dot to the other, the system behaves as an artificial molecule. A typical DQD-based device consists of two coupled single QDs, QD_L and QD_R, referred as the left and right QD, each QD is coupled to a reservoir (source and drain) by two tunnelling barriers (in our device two narrow constrictions) with a tunneling rate $\Gamma_{S/D}$, as schematized on Fig. 2.11a. The QDs are tunnel coupled via a mutual tunneling barrier with a tunnel rate t. Two plunger gates are used to tune the electrochemical potentials of the two dots, denoted V_{PL} and V_{PR}, which are capacitively coupled to the dots through capacitances C_{PL} and C_{PR}, for the left and right dots respectively. Additionally, we consider cross-capacitances of the left plunger gate with the right dot, and vice versa, denoted $C_{PR/L}$ and $C_{PL/R}$, respectively (see Fig. 2.11b). Electrons occupying one of the QDs will electrostatically interact with the electrons on the other QD. This is captured in a mutual capacitance between the QDs, C_m.

In the linear transport regime, a tunneling current can only flow if the electrochemical potentials of both QDs, μ_L and μ_R, are aligned with each other and with the one of the reservoirs.

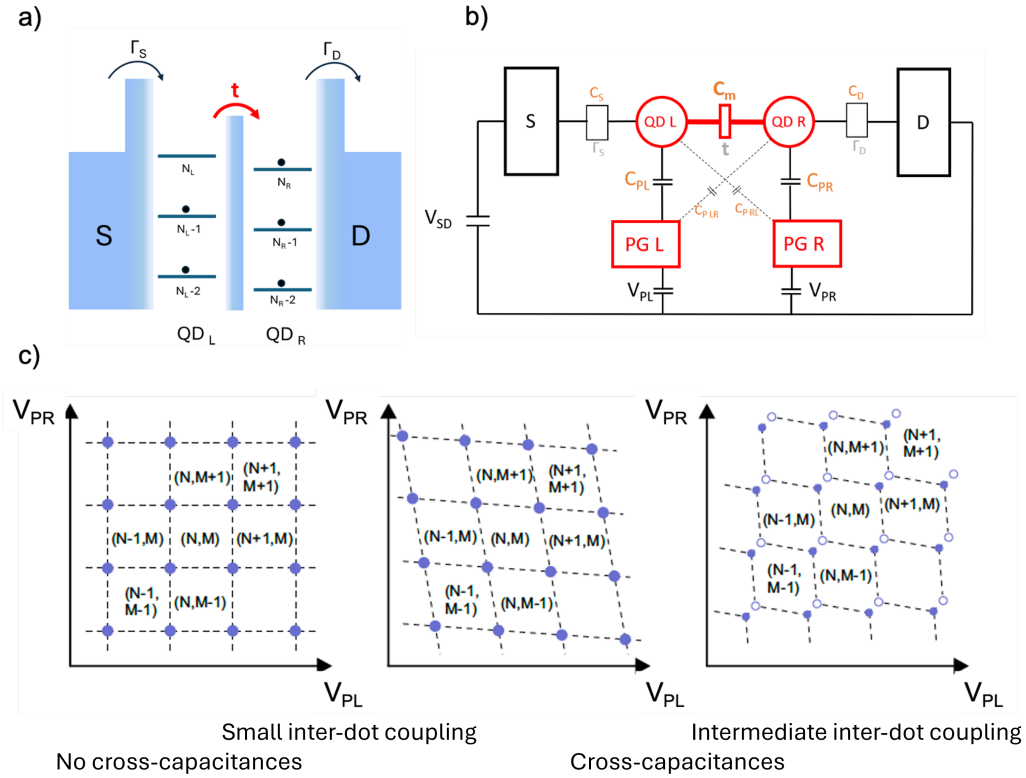

Figure 2.11: **(a)** Schematic representation of the electrochemical potentials in a DQD. The tunneling rates between the source and the dots Γ_S, between the dots and the drain Γ_D, and in-between the dots t are represented. **(b)** Equivalent electrical circuit. **(c)** Schematic stability diagram of the double-dot system for (left) small inter-dot coupling neglecting cross-capacitances, (middle) small inter-dot coupling including cross-capacitances, and (right) intermediate inter-dot coupling. The equilibrium charge on each dot in each domain is denoted by (N,M). Adapted from [24].

Based on this statement and by tuning the two plunger gate voltages, the charge stability diagram of a DQD is obtained [25]. We assume the electrochemical potential of each QD is now entirely controlled by their respective gate, by neglecting the cross capacitances of the gates and the mutual capacitance of the QDs. The vertical (horizontal) dashed lines in Fig. 2.11c (left) indicate whenever the electrochemical potential of QD_L (QD_R), $\mu_L(\mu_R)$ is aligned with the electrochemical potential of the reservoirs. Tunneling transport can only occur if, $\mu_S = \mu_L(N) = \mu_R(M) = \mu_D$, which is indicated by the blue circles marking the crossing points of the dashed lines. The regions enclosed by the dashed lines mark areas of constant electron occupation on both dots, (N;M). Including the cross capacitances of the gates causes $\mu_L(N)$ and $\mu_R(M)$ to be dependent on both gate voltages, resulting in a tilt of the dashed lines (see Fig. 2.11c (middle). The slope of the dashed lines is the relative lever arm of the QD. When considering that three consecutive tunneling processes are needed for an electron to pass the DQD from source to drain, it becomes apparent that two mechanisms are possible: For electron transport, the DQD is in a charge state (N;M). First, an electron tunnels into QD_L, changing the charge state to (N+1;M). The excess electron tunnels then into QD_R (N;M+1), before exiting QDR to the drain electrode, resulting in the initial charge state of (N;M). The second possible transport mechanism is hole transport, where the initial charge state is (N+1;M+1). First, an electron leaves QD_R, resulting in a charge state of (N+1;M), then one electron tunnels from QD_L to

QD_R yielding (N;M+1), before an electron tunnels into QD_L from the lead resulting in the initial state of (N+1;M+1). Electron and hole transport overlap in the charge stability diagram if the mutual capacitance is neglected. When we consider C_m, the electron and hole transport are separated by the mutual capacitive coupling (see Fig. 2.11c (right), forming so-called triple points, where three charge states intersect. For high tunneling rates, so-called cotunneling where tunneling events from source through only one of the QDs into the drain can be observed and the other QD is only virtually occupied, when the electrochemical potential of one of the QDs is aligned with that of the reservoirs. Cotunneling schematic representation is depicted in Fig. 2.17 and is observed along the dashed lines in the charge stability diagram in Fig. 2.11c.

The addition energy, $E_{add}(N_{L/R})$, can be defined for each QD, with $N_{L/R}$ the number of electrons in the left and right quantum dot, respectively : $N = N_L + N_R$ represents the total number of electrons. The charging energy E_{CL} corresponds to the addition energy of an electron to the left QD : $\mu_L(N_L+1, N_R) - \mu_L(N_L, N_R) = E_{CL}$. A similar expression is retrieved for E_{CR}. The DQD model and the quantum dots coupling give rise to the mutual charging energy E_{Cm}, corresponding to the change in the energy of one of the QDs when an electron is added to the other in a two coupled QDs system. It can be written as $E_{Cm} = \mu_L(N_L, N_R+1) - \mu_L(N_L, N_R) = \mu_R(N_L+1, N_R) - \mu_R(N_L, N_R)$. The charging energies are thus expressed by [25] :

$$E_{CL/R} = \frac{e^2}{C_{L/R}}(1 - \frac{C_m^2}{C_L C_R})^{-1} \tag{2.15}$$
$$E_{Cm} = \frac{e^2}{C_m}(\frac{C_L C_R}{C_m^2} - 1)^{-1}$$

with $C_{L/R}$ the total capacitance of the left/right QD.

2.3.2 Transport measurement set-up

In this section, we describe the low-temperature transport measurement setup used to study the transport properties of the graphene DQD device. We placed the device at the base of a refrigerator, an equipment that belongs to the group of Takis Kontos and Matthieu Delbecq.

Embedding of the chip in the sample holder

We first glued the device with a PPMA resist to a sample holder and micro-bonded it to a printed circuit board (PCB) placed on a dual in-line package (DIP) sample holder. The pins of this package are soldered to DC lines that are connected to the DC lines of the cryostat. This DIP is attached to the cryostat finger element, a copper plated metallic sample holder especially designed for this purpose, and wired to a switch box. Great care must be taken during the transfer process, as graphene QDs are very sensitive to electrical discharges that may occur during connections. To this end, one should always keep the DC lines grounded to prevent the circuit lines from being at a floating potential during the transfer into the cryostat. Also, one should check that there is no shunt between the cryostat DC lines that will be inside the ^{3}He pot and the sample holder.

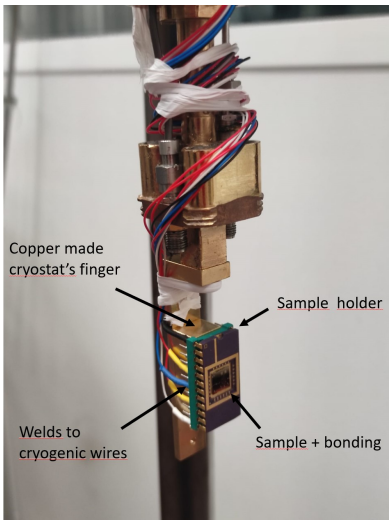

Figure 2.12: Photography of the graphene DQD based device set on the copper cryostat's finger element. The device is microbonded to the sample holder, whose pins are connected to DIB in green, which are welded to cryogenics wires.

^{3}He refrigerator

The experiments presented in this PhD work have been carried out in a dry ^{3}He refrigerator with a base temperature of 280 mK [26]. The DC wiring of this cryostat has been done by M.M. Desjardins. The base temperature is obtained by pumping on ^{3}He liquid contained in a closed circuit with an charcoal pump. This temperature is maintained over ∼30 hours before the ^{3}He fully evaporates. The maximum helium capacitance of the cryostat required an He-refill every 4 or 5 days, for an average of around 35 He liters per refill. As the base temperature is 280 mK, the smaller energy scale that can be resolved is typically 3.5 k_BT= 36 μeV that is significantly lower than energy scales in the THz spectral range (E= 4meV at 1 THz).

DC measurements

The whole measurement setup for transport spectroscopy of the graphene DQD is presented in Fig.2.13. DC voltages of all electrodes are controlled by DC voltage sources. The tunneling current I_{SD}, in the range of 1 nA, is measured using a transimpedance amplifier (10^7 gain) connected to the drain electrode and the voltage is read by a Keithley 2000. The integration time used to record the current is 60 ms. We use low pass filters connected to DC sources and a voltage divider placed on the source line to minimize the electrical noise in the measurements. The whole electric apparatus is computer controlled, which enables automated measurements. This transport spectroscopy setup was developed in the group of Takis Kontos and Matthieu Delbecq at LPENS.

2.3.3 Transport through a graphene DQD

In this section we present the measurements of dark transport through the graphene DQD-based device (see chapter 1, performed in collaboration with Takis Kontos and Matthieu Delbecq. To control the transport through the device, we use two gate voltages V_{G1} (V_{G3}) to tune the two tunnel barriers between the left (right) QD and the source (drain). Two other gate voltages, V_{PL}

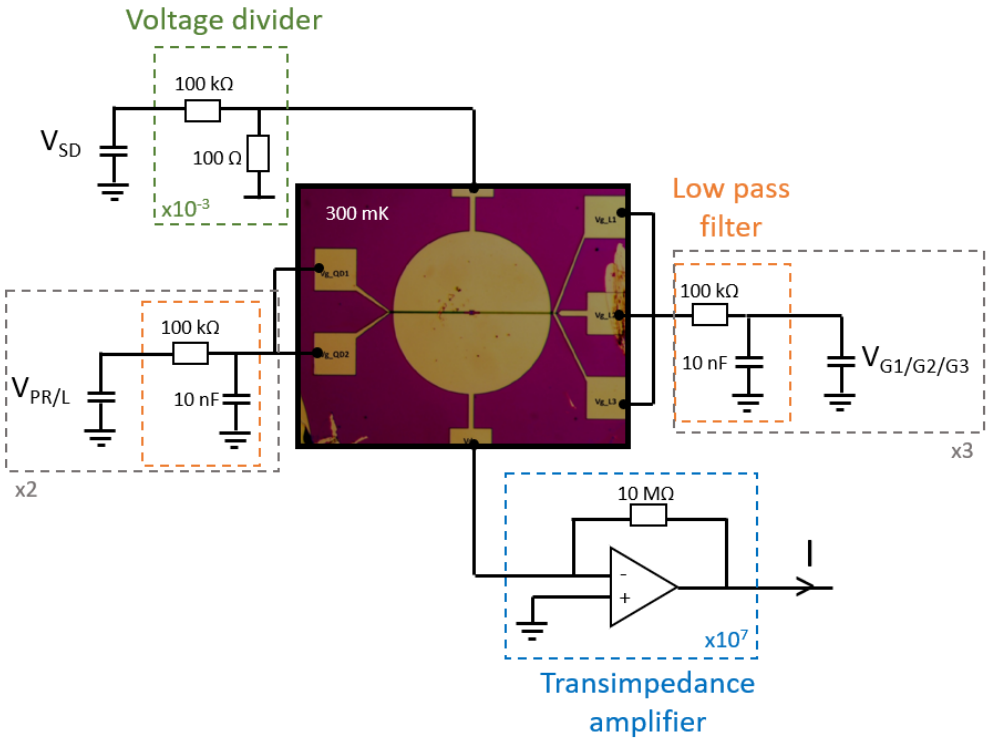

Figure 2.13: Transport measurement setup. The bias and gates voltage DC sources are connected to a voltage divider and to low pass filters respectively to reduce electrical noise. The current flowing through the quantum device is amplified by a factor of 10^7 by a I-V converter transimpedance amplifier.

and V_{PR}, allow to tune independently the chemical potentials in each QD. A gate voltage V_{G2} enables to control the tunneling rate between the two QDs. A last, source and drain electrodes enable to apply a bias, V_{DS} ,to the device.

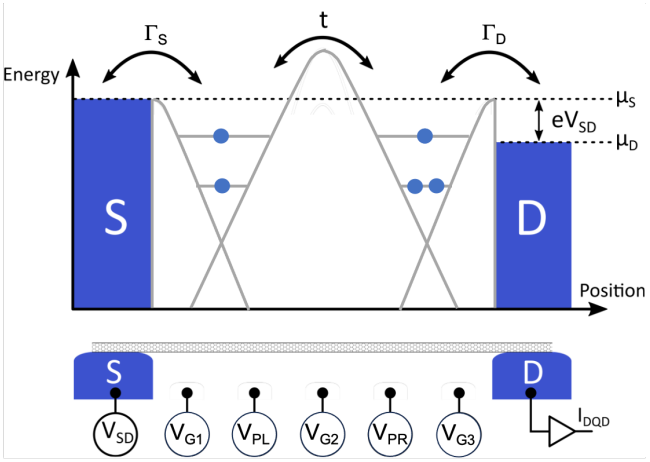

Figure 2.14: **(Top)** Landscape of the confinement potential in the graphene QDs felt by conduction electrons. The two fermionic reservoirs associated to the source and drain electrodes are shown in blue. **(Bottom)** View of the graphene DQD circuit.

Coulomb Blockage regime

To fully characterize the transport in a double quantum dot, one has to measure the current as a function of the five gate voltages and the bias voltage V_{SD}. This would produce a six-dimensional array, which is not very handy. A first approach is to record the source-drain current as a function of a plunger gate, V_{PL} or V_{PR}, while keeping V_{G1}, V_{G2}, V_{G3} and the other plunger gate constant to reach the Coulomb blockade regime. Fig.2.15 shows the low temperature measurements of source-drain current as a function of V_{PL} and of V_{PR} at a bias $V_{SD} = 0.2$ mV. For $V_{PL} = 10$ V, the overall shape of the current over $V_{PR} \in$ [-10, 10] V resembles that of bulk graphene but is distorted by fluctuations that are typical of mesoscopic devices and are due to quantum interference (see Fig. 2.15b). The neutrality point is expected at large V_{PR}. Thus, we record the current for large values of V_{PR}. We observe current suppression regions for $V_{PR} = 6$ V (see dashed blue rectangle in Fig. 2.15b) and even stronger for $V_{PR} = 7$ V around $V_{PL} \in$ [4,5] V (see dashed red rectangle Fig. 2.15c). Many reproducible current fluctuations are also visible. We attribute the region of suppressed current to a configuration where the plunger gates set the empty levels of the QDs in the so-called transport gap of the constrictions connecting the QDs to their respective reservoir. Indeed, graphene constrictions (nanoribbons) exhibit an effective energy gap. The energy gap is estimated from $E_g = a/w\, e^{-bw}$ where $a = 1$ eV.nm and $b = 0.023$ nm^{-1}. We found for the 40 nm width constrictions of our device $E_g \sim 10$ meV [27]. Note that previous studies on etched graphene nanoribbons have shown that the transport gap is significantly larger than energy gap of the constrictions due to the formation of charged islands in constrictions and bulk and edge disorders. In the region of suppressed current, we observe pronounced Coulomb resonances separated by regions of zero current, indicating the sequential tunneling regime. In this configuration, the constrictions act as tunneling barrier for electrons and the transport is allowed only if the chemical potential of the reservoir crosses empty levels of the QDs. From these first series of measurements, we define the regions of the plunger gate voltages of the two QDs, $V_{PL} \in$ [4, 5] V and $V_{PR} \in$ [6, 7] V, that set the device in the single-electron sequential tunneling regime. These are the regions we will probe to study the charge stability diagram.

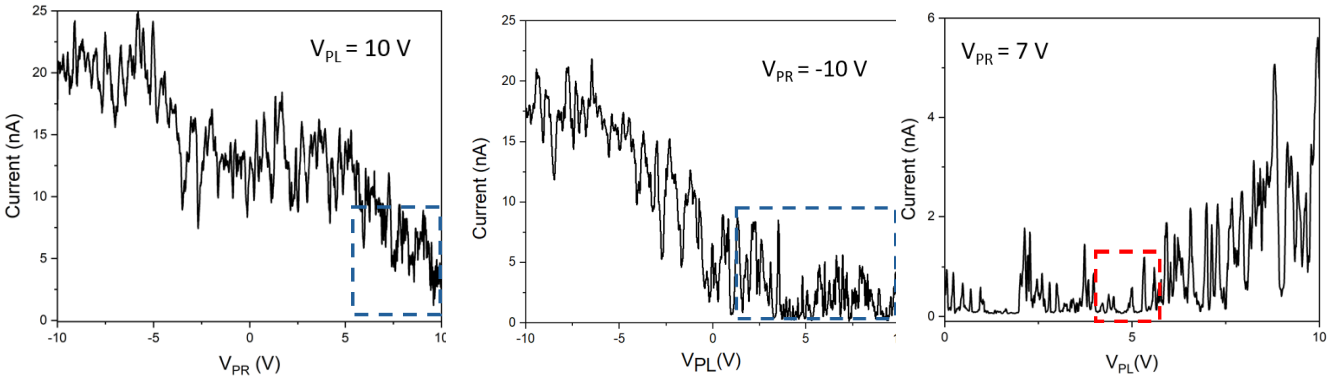

(a) (b) (c)

Figure 2.15: **(a)** Source-drain current as a function of V_{PR} for fixed V_{PL}=10 V. No plateau nor isolated peaks are visible, but a decrease of the current is noticeable for positive V_{PR}, indicating the Coulomb regime may lie in positive values. By sweeping V_{PL} for positive values and setting **(b)** V_{PR}=6 V and **(c)** V_{VPR}=7 V fixed, the presence of plateau and isolated Coulomb peaks is confirmed for $V_{PL} \in [3, 4]$ V for instance, indicating the region of sequential tunneling regime.

Stability diagram

Fig.2.16 shows color scale plot of the measured source-drain current, I_{SD}, as a function of the two plunger gates $V_{PL} \in [4, 6.5]$ V and $V_{PR} \in [6, 7.7]$ V according to results obtained in Fig. 2.15. A fixed bias voltage V_{SD}=0.2 meV is applied and V_{G1}, V_{G2}, V_{G3} are kept constant. Several domains can be identified. Around domain I (red circle on Fig. 2.16), there is a set of parallel lines that tend to bend and meet their neighbors in domain II (white circle). Domain III (orange circle) reveals hexagonal areas, or honeycomb patterns, the typical signature of the charge stability diagram of a DQD.

Note that at low bias, as discussed in section 2.3.1, tunneling transport only occurs when the chemical potentials of the QDs and of the reservoirs are aligned, giving rise only to circles in the charge stability diagram. However, we observe clear tilted horizontal and vertical yellow lines in Fig. 2.16 indicating non-zero current lines in gate voltage ranges where the chemical potential of one QD is not aligned with those of the reservoirs. This is attributed to the co-tunnelling mechanism that results from the tunneling of an electron involving a virtual process [28]. The electron passes from the reservoir to a higher virtual energy state of the QD before passing to the other QD and other reservoir. In other words, due to high tunneling rates, when the chemical potential of only one QDs is aligned with that of the reservoirs, we observe tunneling events from the source into the drain through only one QD with the other QD being only virtually occupied (see Fig. 2.17).

The other gate voltages also influence the different regimes. V_{G1} and V_{G3} act on the quantum dot-lead tunnel rates described by Γ_S and Γ_D. They directly impact co-tunneling process by tuning the potential barriers of the constrictions, and are adjusted to suppress at best co-tunneling lines. However, due to cross capacitances, it is challenging to suppress them without affecting the honeycomb and triple-points shape. V_{G2} controls the interdot tunnel rate, the tunnel rate between the two dots, t, which plays a dominant role in the regime of

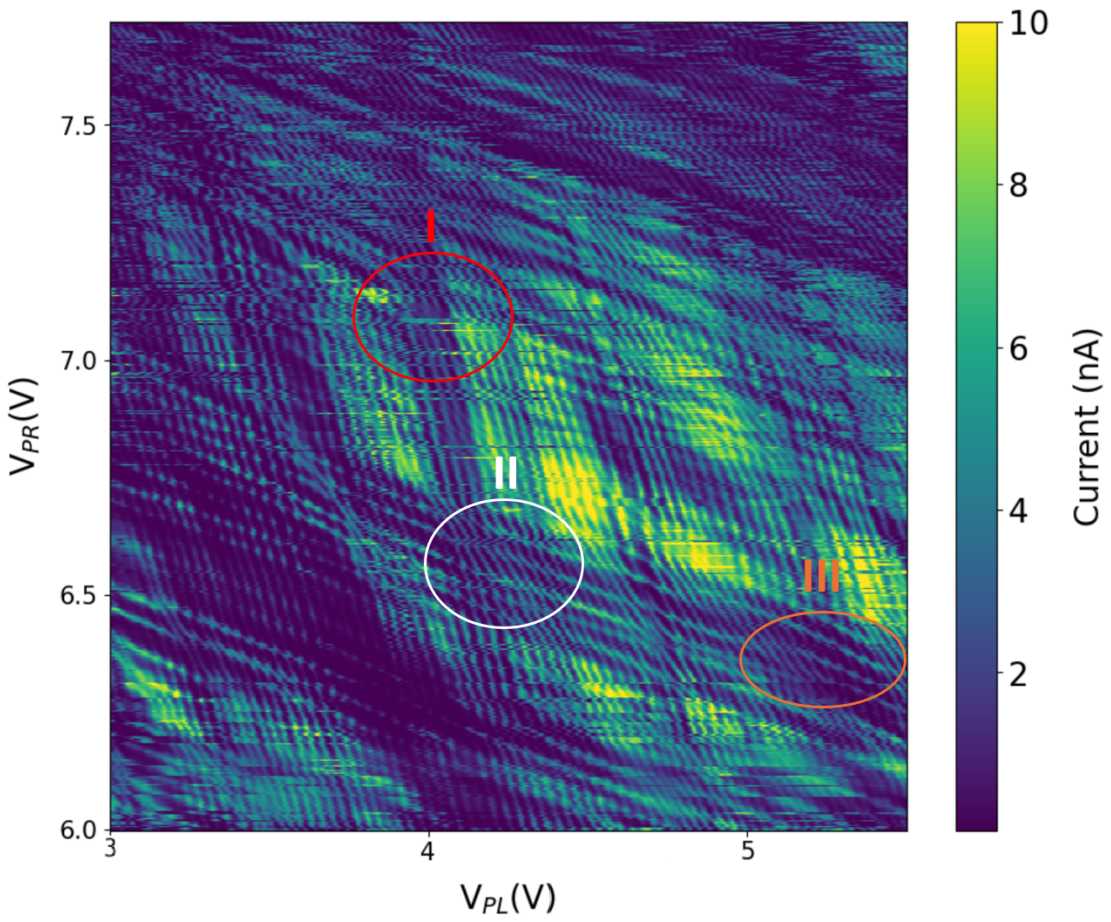

Figure 2.16: Charge stability diagram showing the conductance through the graphene DQD as a function of left and right plunger gates voltages V_{PL} and V_{PR}, at V_{SD}=0.2 meV. The wide range of plunger gate voltages reveals different characteristic domains, highlighted by I, II, and III (red, white, and orange circles, respetively).

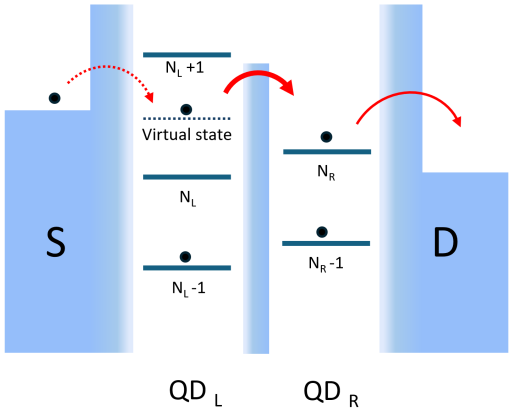

Figure 2.17: Schematic representation of a co-tunneling process involving a virtual state (dotted level in the left dot), enabling the tunneling of an electron from source to drain.

transport. When $t >> k_BT$, coherent tunneling between dot orbitals occur, thus forming molecular orbitals. These regime is called coherent regime of a double quantum dot [25].

Different inter-dot coupling regimes

We describe in the following the influence of the inter-dot coupling, controlled by V_{G2}, on the transport through the graphene DQD, based on our measurements.

- **Small inter-dot coupling**: When V_{G2} cancels the inter-dot coupling, the mutual capacitance is zero and the stability diagram has a rectangular pattern, as shown in Fig.2.18. The chemical potential of the QD is now entirely controlled by their respective gate without affecting the charge of the other dot. Electron and hole transport overlap in the charge stability diagram as the mutual capacitance cancelled. The oblique horizontal and vertical current lines result from cotunneling transport as discussed previously.

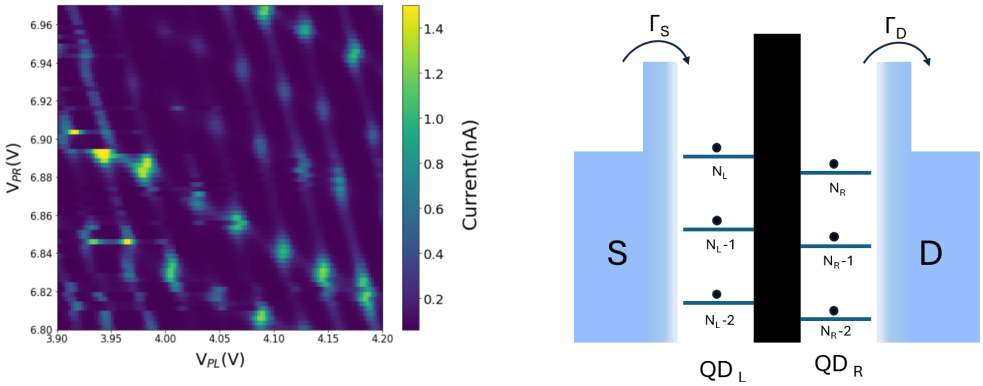

Figure 2.18: **(a)** Stability diagram representing the graphene DQD behaving like two independents QDs, with rectangular conductance lines. Measured for $V_{G2} = -0.27$V. **(b)** Associated schematic representation. The black rectangle symbolizes the opaque barrier between the dot, with no electron tunneling.

- **Intermediate inter-dot coupling**: When V_{G2} induces a coupling between the two QDs, curved current lines are observed with the emergence of triple-points. As the mutual capacitance is non-negligible anymore, the electron and hole transport are separated forming so-called triple points, where three charge states intersect (Fig. 2.19). The energy difference between both processes determines the separation between the triple-points and is given by E_{Cm}. Note that when a bias is applied, triple points turn into triangles.

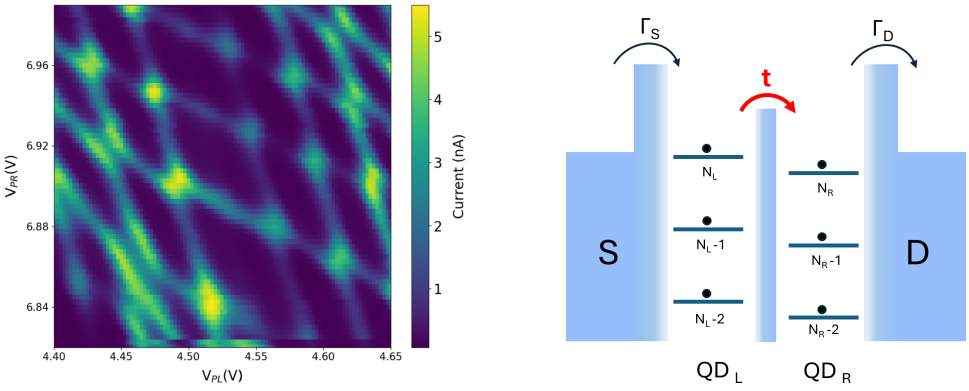

Figure 2.19: **(a)** Stability diagram showing the graphene DQD that starts behaving like a double dot structure, with triple points splitting : the cells now show curved vertices. Measured for $V_{G2} = -0.24$ V. **(b)** Associated schematic representation.

- **Large inter-dot coupling**: By tuning V_{G2} to further increase the inter-dot coupling, the oblique current lines become parallel to each other and the triple-points disappear in the stability diagram, as observed in Fig. 2.20. In this regime, the two QDs behave as a large single QD with charge $(N_L + N_R)$. Therefore, the addition of an electron to one QD modifies the chemical potential of the other QD and the chemical potential of the whole system is equally influenced by V_{PL} and V_{PR}. Note that the current lines are not diagonal as $C_{PR} \neq C_{PL}$.

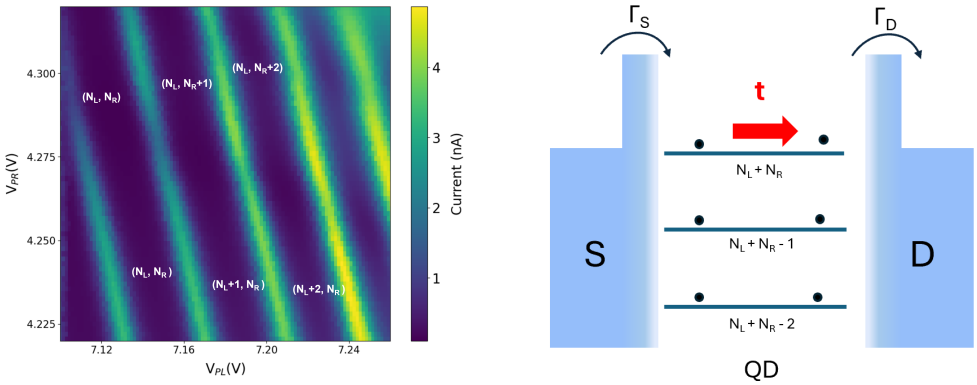

Figure 2.20: **(a)** Stability diagram showing the two overcoupled dots that behave like one large dot. The conductance lines appear parallel with no triple-points anymore. Measured for $V_{G2} = -0.2$ V. **(b)** Associated schematic representation. The absence of barrier and the large red arrow symbolize strongly coupled dots.

2.3.4 Honeycomb and triple-points quantitative analysis

The charge stability diagram is of great value in setting up and characterizing a DQD. In particular, in the context of this thesis, the open question was whether the DQD system can form a two-level system with energy separation in the THz spectral range. To this end, we tune V_{G1} and V_{G3} to strongly reduce the cotunneling and V_{G2} to give rise to the largest triple point separation. Fig.2.21 shows a high resolution charge charge stability diagram of the device, showing the current through the channel as a function of the plunger gate voltages V_{PL} and V_{PR}at a constant bias voltage of V_{SD}=0.5 meV. We clearly observe the honeycomb pattern characteristic of the graphene DQD with the cell pattern repeated several times, and a well-defined charge configuration (N_L, N_R) (see Fig. 2.23b). As the plunger gate voltages increase, the mutual energy E_{Cm} also increases. This is evidenced by the current lines shaping the honeycomb patterns, which tend to become more parallel, while the voltage V_{G2} is constant. We attribute this tendency to disorder near the gates of the plunger, which in addition to control the number of electrons in each QD, modifies the inter-dot coupling in the same way as V_{G2} [29].

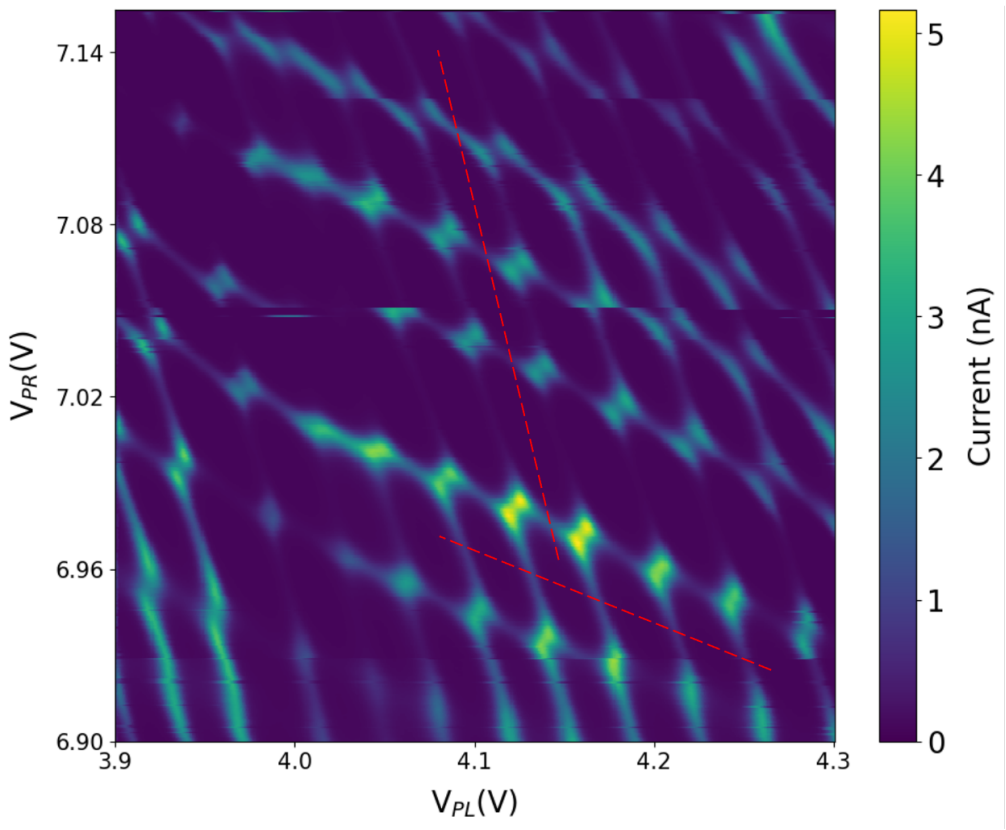

Figure 2.21: High resolution charge stability diagram of the graphene DQD device at a fixed V_{SD}=0.5 mV. Around V_{PL}= 4.1 V and V_{PR}= 7.05 V the device behaves as a DQD as the stability diagram shows curved current lines and repeated honeycomb pattern. Dashed red lines represent cut-lines of current used to observe Coulomb peaks in Fig. 2.22.

The line-cuts as the oblique red dashed lines in Fig.2.21 evidences the strong current suppression in the Coulomb blockaded regime (see Fig. 2.22). Indeed, the tunneling current through the DQD as a function of V_{PL} and V_{PR} at low V_{SD} reveals clear Coulomb peaks pattern.

(a) (b)

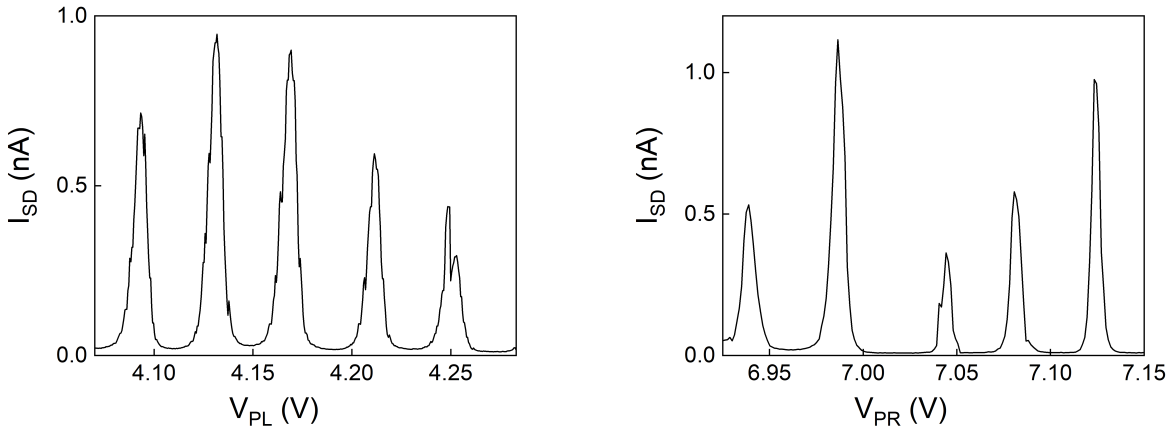

Figure 2.22: Current as a function of V_{PL} (**a**) and as a function of V_{PR} (**b**). The other plunger gate, V_{PL} for (**a**) and V_{PR} for (**b**), evolves to follow the red dashed lines in Fig. 2.21.

Using the electrostatic parameters defined in [25], relevant quantities can be extracted from honeycomb features and triple-points structures. For this quantitative analysis, we first focus

on a single honeycomb structure, depicted in Fig. 2.23a, measured at V_{G2}=-0.27 V and V_{SD}=0.5 mV. From the data, we extract $\Delta V_{PL} = 32.7$ mV, $\Delta V_{PR} = 30$ mV and determine the capacitances of the left and right QD to their plunger gate $C_{PL} = \frac{e}{\Delta V_{PL}} = 4.9$ aF. and $C_{PR} = 5.3$ aF (respectively). Thus, both QDs have relatively similar coupling to their respective plunger gate, indicating a relatively high device uniformity.

At finite bias, the triple points that are the vertices of the honeycomb expand into triangles of height δV_{PR} and width δV_{PL}, as shown in Fig. 2.23a. Indeed, for a bias voltage applied to the left lead ($\mu_S = eV_{DS}$) with the right lead grounded ($\mu_D = 0$), the bias voltage is coupled to the double dot through the capacitance of the left lead, C_S, and hence also affects the electrostatic energy of the system. The conductance regions at finite bias are triangularly shaped regions with boundaries determined by the conditions $eV_{DS} = \mu_S \geq \mu_L$, $\mu_L \geq \mu_R$, and $\mu_R > \mu_D = 0$. The dimensions of the triangles $\delta V_{PR/L}$ and $\delta V_{PR/R}$ (see Fig. 2.23) are related to V_{DS} as follows:

$$\alpha_L \delta V_{PL} = \frac{C_{PL}}{C_L}|e|\delta V_{PL} = |eV_{DS}| \tag{2.16}$$

$$\alpha_R \delta V_{PR} = \frac{C_{PR}}{C_R}|e|\delta V_{PR} = |eV_{DS}| \tag{2.17}$$

Analyzing one of the triangles from the same stability diagram, we extract the left and right lever-arms $\alpha_{L/R}$ expressed as : $\alpha_{L/R} = \frac{eV_{SD}}{\delta V_{PR/L}}$ that represent the conversion factors between gate voltage and energy. We find $\alpha_L = \frac{eV_{SD}}{\delta V_{PL}} \approx 0.064$ and $\alpha_R = \frac{eV_{SD}}{\delta V_{PR}} \approx 0.081$.

It is now possible to determine the total capacitances, $C_{L(R)}$, from the relation $\frac{C_{PL(R)}}{C_{L(R)}} = \alpha_{L(R)}$. We find $C_L = 76.5$ aF and $C_R = 65.4$ aF, giving a single QD charging energy $E_{CL} = \alpha_L \Delta V_{PL} = 2.1$ meV and $E_{CR} = \alpha_R \Delta V_{PR} = 2.4$ meV. These values are comparable to the charging energies reported in etched graphene single QDs of similar sizes [23]. In addition, the two QDs have close charging energies and lever arms, indicating relatively high device uniformity and similar geometric sizes for the two QDs. Note that the charge energies represent the dominant contribution to spectroscopic level spacing, since for QDs ∼120 nm in diameter, the spacing between quantum states is typically of the order of 2 meV [15]. We also estimate the mutual capacitance between the QDs in this configuration: $C_m = \frac{C_R \quad \Delta V^m_{PL}}{\Delta V_{PL}} = \frac{C_L \quad \Delta V^m_{PR}}{\Delta V_{PR}} \approx 4.7 \pm 0.17$ aF and the mutual coupling energy $E_m = \alpha_L \Delta V^m_{PL} = \alpha_R \Delta V^m_{PR} = 0.46$ meV.

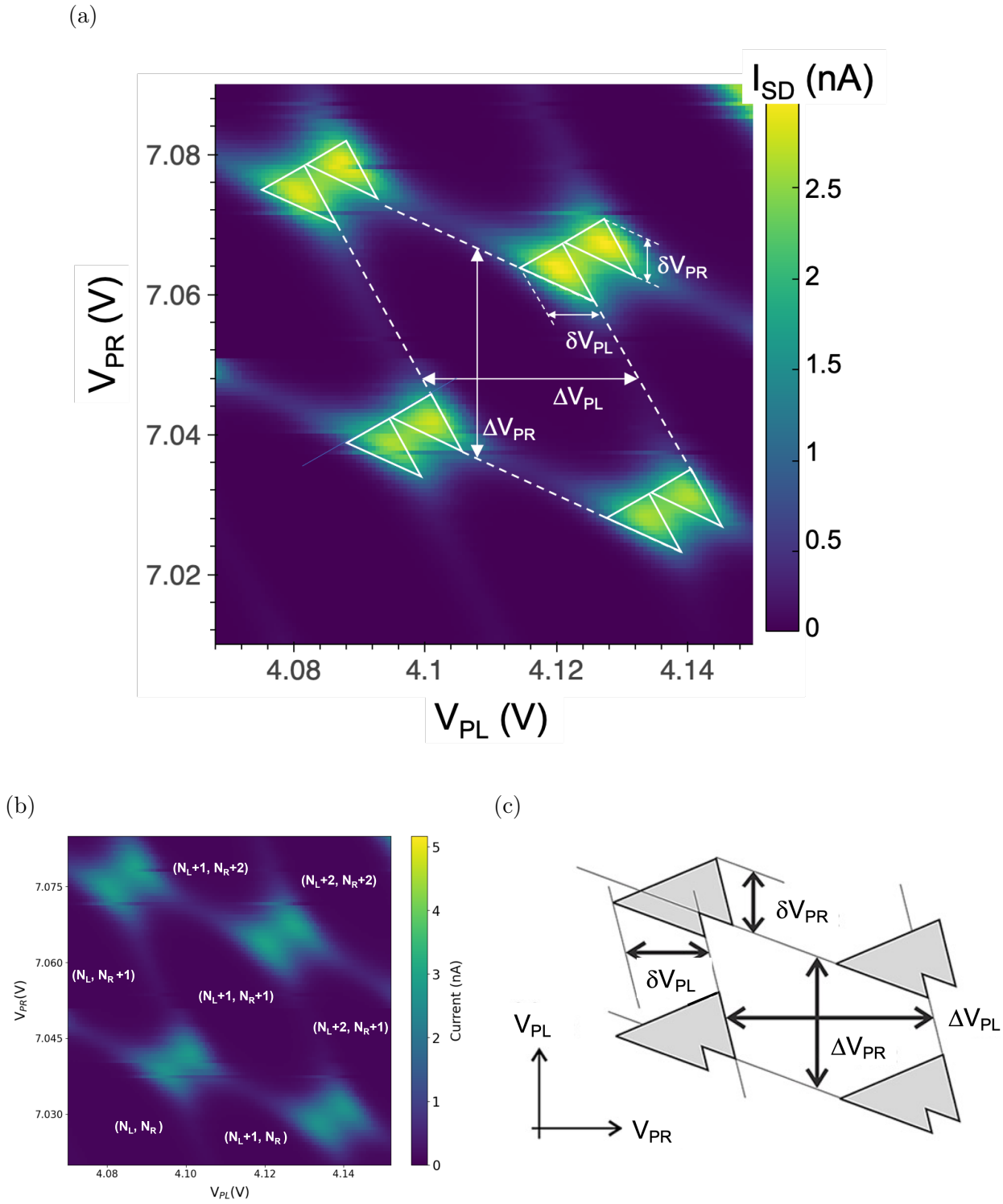

Figure 2.23: **a**. Measured charge stability diagram of a honeycomb pattern of the DQD system together with a schematic labelling the relevant quantities to extract the lever arms and the capacitive mutual coupling energy. **b**. Charge stability diagram of the honeycomb pattern with the regions of stable charge occupancy labeled with tuples (N_L, N_R) where N_L (N_R) indicates the occupancy of the left (right) QD. **c** At finite bias, triangular regions of allowed transport around each triple point are observed. Taken from [30].

We further then investigate the influence of the gate voltage V_{G2} on the mutual charging energy E_m between both QDs. As in our etched graphene DQD device the distance between the QDs is fixed by the length of the constriction, the mutual energy coupling E_m is only controlled by the gate voltage of the constriction between the two dots, V_{G2}. On Fig. 2.24, we follow a triple-point for different V_{G2} by measuring the charge stability diagram within the same range of (V_{PL}, V_{PR}). For each V_{G2}, the corresponding mutual coupling energy E_m is extracted from the triple-point features, assuming the lever-arms to be constant. Fig.2.24b shows the extracted E_m as a function of V_{G2}, revealing a non-monotomic behaviour. Indeed, the coupling energy starts to decrease down to 0.18 meV from V_{G2}=-0.27 to V_{G2}=-0.23 and then increases up to 0.5 meV for V_{G2}=-0.19. Such behavior is fully in agreement with previous experiments on etched graphene DQD [31, 29].

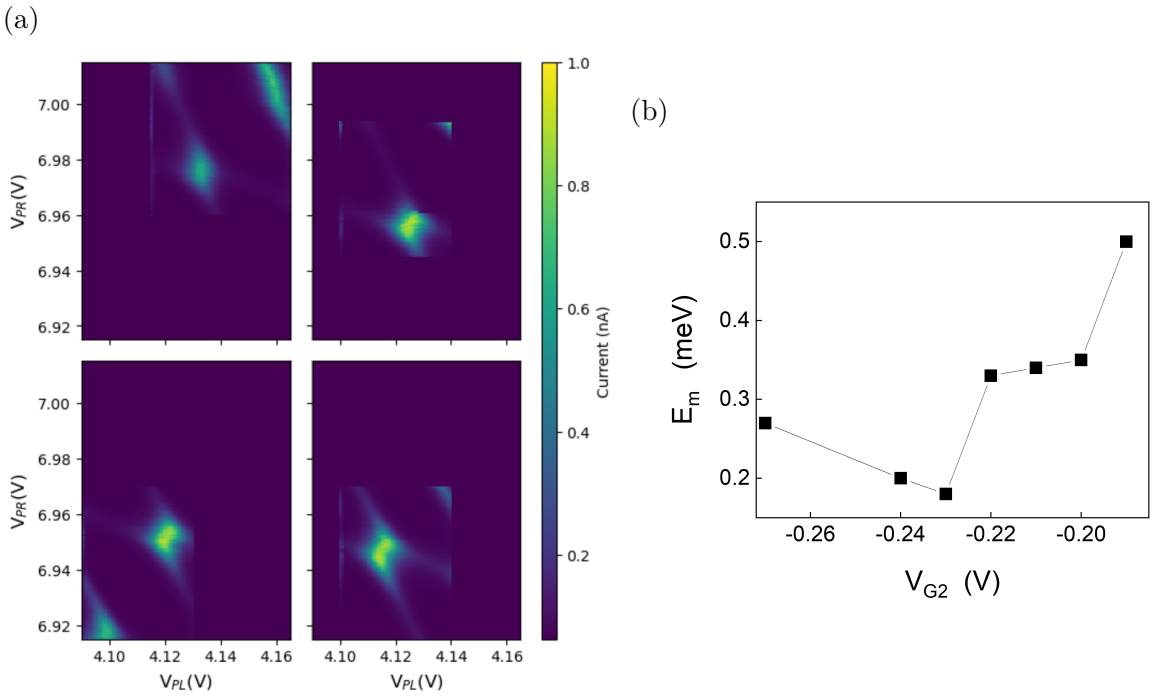

Figure 2.24: **(a)** Close view of the interdot coupling represented by the triangles splitting with increasing V_{G2} from -0.27 V to -0.19 V. We focused on the same triple-point, which changed in (V_{PL}, V_{PR}) position due to cross-capacitance effects. **(b)** Extracted mutual coupling energy from (a) as a function of V_{G2}.

The coupling between the two QDs has two origins : the Coulomb repulsion parameterized by the mutual charging energy E_m and the tunneling rate t between the two dots. We have analyzed the stability diagram solely in terms of the electrostatic coupling between both graphene QDs and determined E_m. However, the stability diagram reveals areas where an interdot transition occurs. In the picture of a single orbital in each dot, for $ht > k_BT$, the electron tunnels from one dot to the other at a rate t. This results in a two-level system, which is a much desired building block for applications in quantum technology, such as quantum information coding. In the following, we will get insight the properties of the two-level system within our graphene DQD device by analyzing the inter-dot tunneling rate t.

2.3.5 Exploring the two-level system

Basics on 'artificial' molecular description

When electrons can tunnel coherently from one dot to the other at appreciable rates, the eigenstates become delocalized, extending over the entire double dot system. We discuss here the elementary case of a quantum mechanical two-level system, appearing on a triple-point, for a non-zero interdot coupling, which is quite relevant for understanding the physics of a tunnel-coupled DQDs. We will focus on a given single electron transition $(N_L, N_R+1) \rightarrow (N_L+1, N_R)$ at the triple-point.

Our first interest lies on well-separated two QDs, that behave independently, described by a total Hamiltonian H_0, with eigenstates $|\varphi_L\rangle$ and $|\varphi_R\rangle$, and eigenenergies E_L and E_R:

$$\begin{aligned} H_0|\psi_L\rangle &= E_L|\psi_L\rangle \\ H_0|\psi_R\rangle &= E_R|\psi_R\rangle \end{aligned} \tag{2.18}$$

By introducing a finite tunnel coupling t between the levels in both dots described by the purely non-diagonal Hermitian matrix T:

$$T = \begin{pmatrix} 1 & t_{LR} \\ t_{RL} & 1 \end{pmatrix} \qquad \text{with } t_{LR} = t_{RL}^* \tag{2.19}$$

The Hamiltonian of the coupled DQD system becomes $H = H_0 + H_t$ with delocalized states referred as $|\varphi_{S/A}\rangle$ for the symmetric (S) and asymmetric eigenstates (A) and with eigenvalues $|E_{S/A}\rangle$:

$$\begin{aligned} H_0|\psi_S\rangle &= E_S|\psi_S\rangle \\ H_0|\psi_A\rangle &= E_A|\psi_A\rangle \end{aligned} \tag{2.20}$$

In the $(|\psi_L\rangle, |\psi_R\rangle)$ basis, the symmetric and asymmetric eigenstates write :

$$\begin{aligned} |\psi_S\rangle &= -\sin\frac{\theta}{2}e^{-i\phi/2}|\psi_L\rangle + \cos\frac{\theta}{2}e^{i\phi/2}|\psi_R\rangle \\ |\psi_A\rangle &= \cos\frac{\theta}{2}e^{-i\phi/2}|\psi_L\rangle + \sin\frac{\theta}{2}e^{i\phi/2}|\psi_R\rangle \end{aligned} \tag{2.21}$$

with $\tan\frac{\theta}{2} = 2|t|/(E_L - E_R)$. The corresponding eigenvalues can be expressed in terms of the eigenvalues of the uncoupled double dot and the tunnel matrix elements as follows:

$$E_{A/S} = \frac{1}{2}\Big[\frac{E_L + E_R}{2} \pm \sqrt{(E_L - E_R)^2 + (2t)^2}\Big] \tag{2.22}$$

with $\varepsilon_\Sigma = (E_L + E_R)/2$ the average energy of the two QDs and $\varepsilon_{det} = E_L - E_R$ the detuning energy between the two uncoupled QDs. From equation 2.22, we define the renormalized energy difference between the two delocalized states, ΔE^*, as :

$$\Delta E^* = E_A - E_S = \sqrt{(\varepsilon_{det})^2 + (2t)^2} \tag{2.23}$$

The eigenenergies $E_{A/S}$ of this two-level system as a function of ε_{det} are illustrated in Fig. 2.25b. For small ε_{det}, there is an anti-crossing of $|\psi_S\rangle$ and $|\psi_A\rangle$. The energy difference $\Delta E^* = 2t$ for $\epsilon_{det} = 0$. For large ε_{det}, the eigenenergies of the coupled DQD approach the eigenenergies of the uncoupled QDs, E_L and E_R. In a molecular description, $|\psi_S\rangle$ and $|\psi_A\rangle$ are called bonding and antibonding states. See Fig. 2.25a for a schematic description of the delocalization of the electron wave function over the two QDs giving rise to the new $|\psi_{S/A}\rangle$ eigenstates. Note that for vanishing interdot tunneling rate ($t = 0$), the energy difference becomes $\Delta E^* = \varepsilon_{det}$, the electron wavefunctions are well-localized in each QD and there is no more a two-level system.

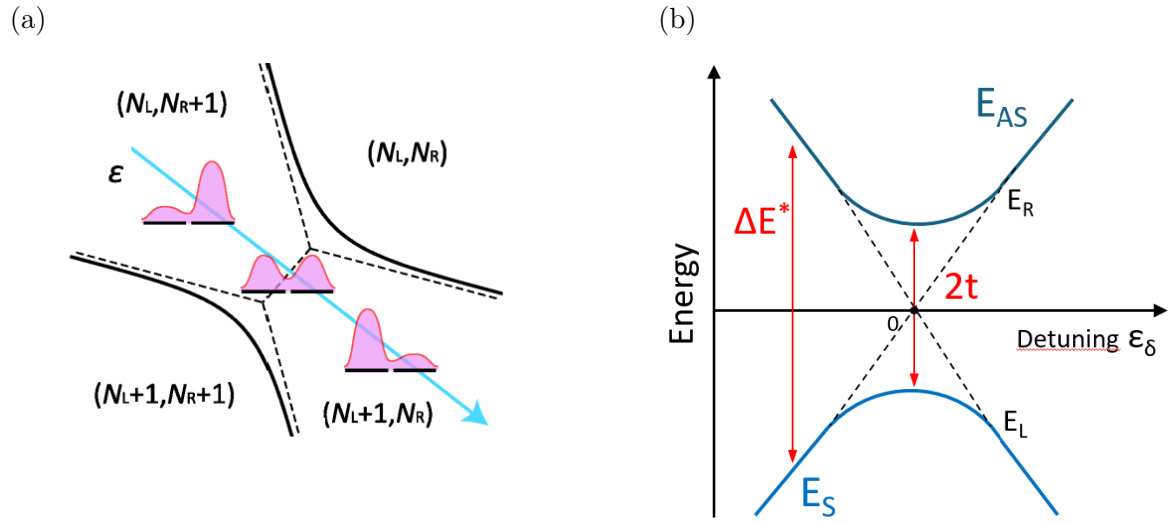

Figure 2.25: **(a)** Displays the electron's wavefunction overlapping between the two quantum dots, resulting in a two-level system. The overlap is reduced for larger detuning energy (ε). Taken from [32]. **(b)** Schematic diagram of a two-level system, where $E_{L/R}$ (dotted black lines) are uncoupled energy levels from left and right dot, and $E_{S/AS}$ (blue curved lines) are the energy levels belonging to the symetric and asymetric states. They are plotted in function of the detuning energy $\varepsilon_\delta = E_L - E_R$. While $E_{L/R}$ cross at zero detuning, $E_{S/AS}$ anticross by an energy splitting of $\Delta E^* = 2t$.

The two-level quantum system is thus characterized by ε_δ the energy difference between the uncoupled charge states $|\psi_L\rangle$ and $|\psi_R\rangle$ that describes the electron to be fully in the left or the right QD respectively, and $2t$ the anti-crossing energy that arises from the finite interdot coupling when the tunnel barrier is sufficiently lowered. The resonance frequency of the two-level system is deduced from the difference energy between the bonding and antibonding eigenstates as: $f_{res} = \Delta E^*/h = \sqrt{(\varepsilon_{det})^2 + (2t)^2}/h$. To realize a two-level system in the THz spectral range, which is the main objective of this thesis, the inter-dot coupling rate t should be of the order of several hundred μV. Two-level systems have been previously demonstrated in DQD based on many material systems such as semiconductor heterostructures, carbon nanotubes, graphene and bilayer graphene with t values typically ranging from $4\mu V$ to $\leq 100\mu V$, i.e. with resonance frequencies from 1 GHz to 25 GHz (see Table 2.3.5). Realizing a two-level system with resonance frequency in the THz spectral range (> 0.1 THz) remains elusive so far and represents the technological challenge of this thesis work.

Material System	ht	f_{res}	**Ref.**
Etched graphene	14 μV	3.4 GHz	[33]
Graphene nanoribbons	106 μV	24.5 GHz	[34]
Gate-defined bilayer graphene	10 μV	2.4 GHz	[29]
	8.5 μV	2.1 GHz	[35]
	4-17 μV	1-4 GHz	[36]
Self-assembled InAs QDs	4.2 μV	1 GHz	[37]
Gate-defined InAs nanowire	16.4 μV	4 GHz	[38]
Gate-defined in silicon	$< 4\mu$V	1 GHz	[39]
Gate-defined Si/SiGe heterostructure	16 μeV	3.9 GHz	[40]
Gate-defined GaAs/AlGaAs heterostructure	5-30 μeV	1.2-7.2 GHz	[41]
Gate-defined carbon nanotubes	62 μV	15 GHz	[42]

The tunneling rate t between the dots

In this section, we analyze our data to evaluate the coupling strength $2t$ within this "artificial molecule", which is characterized by the separation of the bonding and antibonding states. It should be noted that we cannot rely on previous theoretical works that provide a theoretical estimate of the tunneling energy t as a function of the interdot distance and the potential barrier height, as these are limited to GaAs DQDs [43] and gapped graphene DQDs, [44] and are thus not available in etched graphene DQDs. To determine the interdot coupling energy from the charge stability diagram measurement, we record a high-resolved charge stability diagram of a triangle pair (triple point pair) as shown on Fig. 2.26a. The two plunger gate voltages, V_{PL} and V_{PR}, are tuned in two different ways, symbolized by two perpendicular axis, the ε_δ and ε_Σ axis indicated in Fig. 2.26b. The axis ε_δ follows the energy detuning between the two levels of the quantum dots, $\varepsilon_\delta = E_R - E_L = e\alpha_R V_{PR} - e\alpha_L V_{PL}$ in the (V_{PL}, V_{PR}) plane. The axis ε_Σ represents $\varepsilon_\Sigma = (E_R + E_L)/2$, the average energy of quantum dot levels, which follows the baseline of the triangles, where the ground states of the two dots are aligned and shifted within the bias window. Note that we have verified that the two level arms, α_R and α_L, in this range of values of V_{PL} and V_{PR}, are very close to those extracted previously in Fig. 2.23.

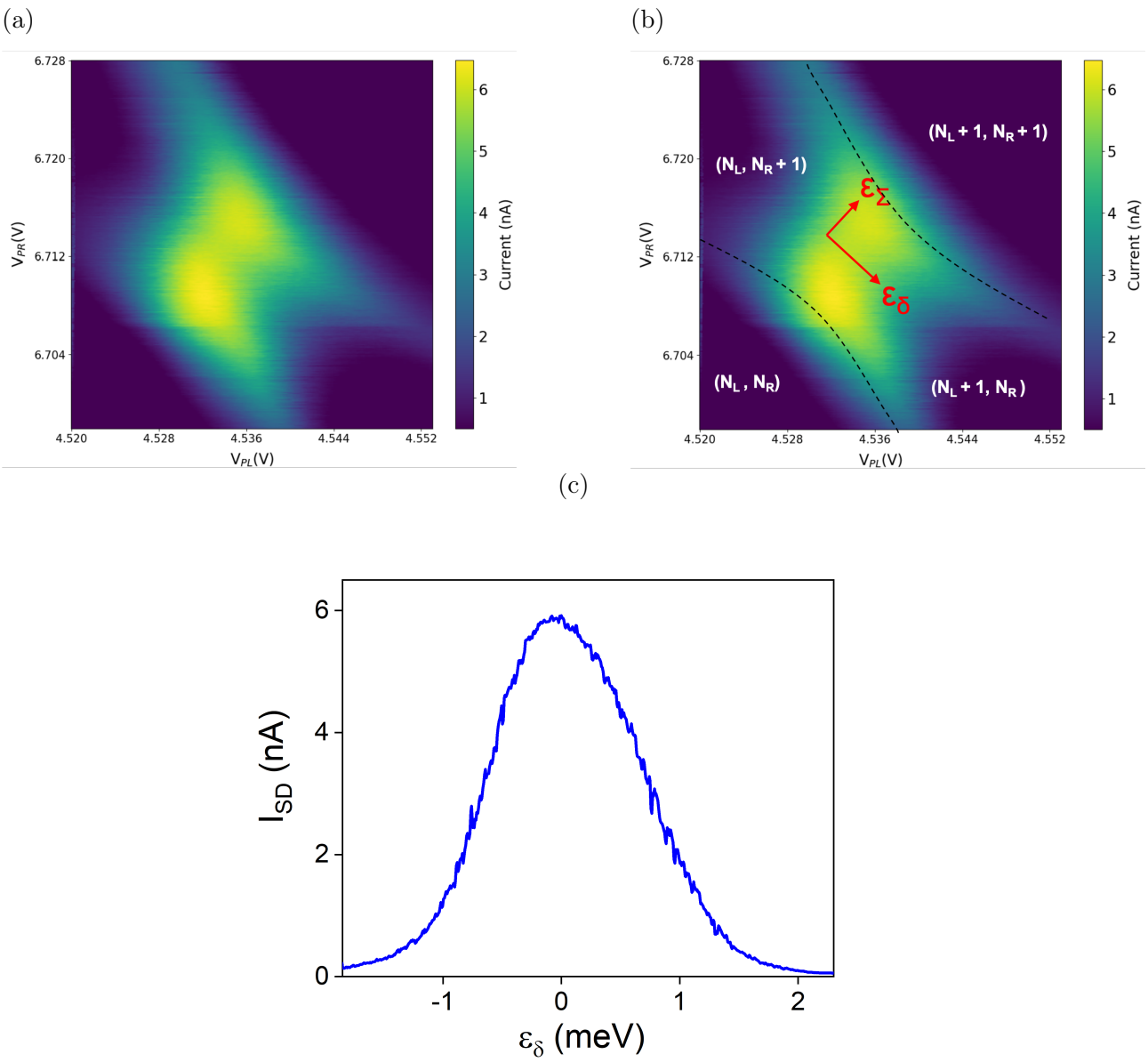

Figure 2.26: **a** Charge stability diagram at V_{SD} =0.7 meV and a central gate voltage V_{G2} = 0.27 V, providing a close view of a measured triple-point. **b** Same measurement but with a charge stability diagram with the indication of the detuning axis $\varepsilon_\delta = E_R - E_L$ and the perpendicular axis $\varepsilon_\Sigma = (E_R + E_L)/2$ in red arrows. Dashed black lines are used as guide lines for curved tunneling lines to delimit the four different charge domains. **c** Line-cut of I_{DS} along the detuning axis ε_δ for V_{SD}=0.7 meV. We set the zero-detuning point at the peak maximum for elastic ground state tunneling [45].

Fig.2.26c shows a source-drain current I_{SD} trace along the detuning axis ε_δ at a finite bias voltage V_{SD}=0.7 meV. The resonance corresponds to the $(N_L, N_L + 1) \rightarrow (N_L + 1, N_R)$ charge transition. We set the zero-detuning value at the peak maximum for elastic ground state tunneling [45]. As we assume an electron temperature of T_e ∼300 mK, i.e. 25.6 μeV, the condition $eV_{SD} >> k_B T$ is fulfilled and thus the linewidth of the resonance at zero detuning is temperature independent. To interpret the evolution of I_{SD}, let us describe the two-level system with a density matrix description. The equations for the density matrix are given by [46] :

$$\begin{aligned}
\frac{\partial \rho_L}{\partial t} &= +\Gamma_S \rho_0 + i\frac{t}{\hbar}(\rho_{RL} - \rho_{LR}) \\
\frac{\partial \rho_R}{\partial t} &= -\Gamma_D \rho_R - i\frac{t}{\hbar}(\rho_{RL} - \rho_{LR}) \\
\frac{\partial \rho_{LR}}{\partial t} &= -\frac{1}{2}\Gamma_D \rho_{LR} + i\varepsilon_\delta \rho_{LR} + i\frac{t}{\hbar}(\rho_R - \rho_L) \\
\frac{\partial \rho_{RL}}{\partial t} &= -\frac{1}{2}\Gamma_D \rho_{RL} - i\varepsilon_\delta \rho_{RL} - i\frac{t}{\hbar}(\rho_R - \rho_L)
\end{aligned} \tag{2.24}$$

with ρ_L, ρ_R and $\rho_0 = 1 - \rho_L - \rho_R$ the probability for an electron to be on the left dot, on the right dot, or in neither dot, respectively, and $\rho_{LR} = \rho^*_{RL}$ are the nondiagonal density matrix elements. ε_δ is the time-averaged energy mismatch. The current $I_{SD} = e\Gamma_D \rho_R$ is determined by the stationary solution of Eq. 2.24:

$$I_{SD} = I(\varepsilon_\delta) = e\frac{\Gamma_D t^2}{(\frac{\varepsilon_\delta}{h})^2 + \frac{\Gamma_D^2}{4} + t^2(2 + \frac{\Gamma_D}{\Gamma_S})} \tag{2.25}$$

This is known as the Stoof-Nazarov equation [47, 48], defining current for resonance occurring between the ground states of both dots for Coulomb-interactive electrons. The current as a function of ε_δ has a Lorentzian-shaped peak with width of the order of $max(t, \Gamma_D/2, t\sqrt{\Gamma_D/\Gamma_S})$.

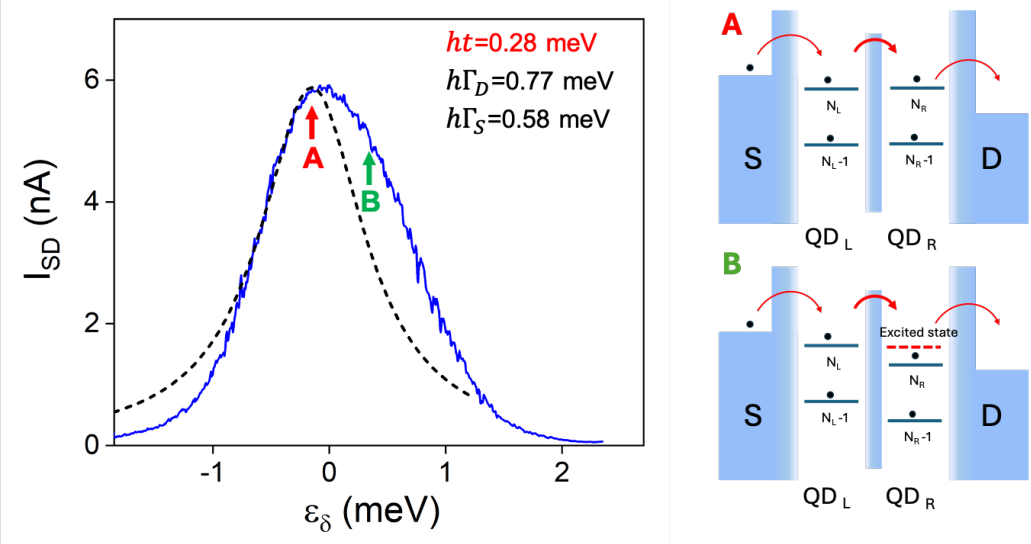

Figure 2.27: I_{SD} as a function of the detuning energy (line-cut from Fig.2.26), at V_{SD}=0.7 mV (blue line). The peak at zero detuning has been fitted (dashed line) by the Stoof-Nazarov equation (2.25). Schematic diagrams showing the possible alignments of the electrochemical potentials in the case of two levels per dot. (A) The first electrochemical potentials to align correspond to the ground states of both dots, N_L and N_R. (B) When moving down the levels in the right dot, the next states to align are the ground state of the left dot, N_L, and the first excited state of the right dot.

We observe on Fig. 2.27 that the left-hand side of the current peak (blue curve) is relatively well fitted by the Lorentzian line (dashed black line). The right-hand side of the current peak shows a deviation from the Lorentzian fit due to the contribution of excited states, co-tunneling

processes and inelastic transport [29, 25] that are not taken into account for the fit. Indeed, the resonance line of the ground state should overlap with the lines of the excited states because the tunnel rates towards the leads are comparable to the level spacing, $\Delta E_{\text{level}} \sim h\Gamma_{S/D}$ [49]. So the current also appears when the levels from excited states in one dot are in resonance with the ground state in the other (see Fig. 2.27). Also, at large negative detuning energy ($\varepsilon_\delta < -0.8$ meV), we observe that the recorded current is lower than the predicted current leading to a reduced tail. This discrepancy is currently under investigation and is attributed to interactions effects. The fit yields an interdot tunnel coupling of ht=0.28 meV and a dot-lead tunnel coupling of $h\Gamma_D$=0.77 meV and of $h\Gamma_S$=0.58 meV. From this analysis, we extract the two-level system resonance frequency: $f_{res} = 2t/h$ =0.137 THz. We thus demonstrate a two-level system in the THz spectral range opening promising perspectives towards the development of quantum THz devices.

We further estimate the resonance frequency of the two-level system f_{res} by measuring a map of I_{SD} as a function of V_{SD} and ε_Σ, as shown in Fig. 2.28a. The current is probed along the baseline of the two triangles corresponding to zero detuning energy, i.e. ε_δ=0. The Coulomb diamonds due to regions of suppressed current, which are characteristic of the sequential tunneling, are clearly visible in Fig. 2.28a. However, the Coulomb Diamond map differs from usual Coulomb Diamond maps measured in a single QD based device [15]. To interpret this map, we assume that the symmetric and anti-symmetric states of the two-level system can only be occupied by a single electron (i.e. spinless electrons). As represented schematically in Fig.2.28b, the triple points of the weakly coupled double dot (orange points) develop into orange crescents for a strongly coupled double dot. The length of these crescents increases with the interdot tunnel coupling t. Moving along the direction ε_Σ from lower left to upper right, first the symmetric state aligns with the electrochemical potentials of the leads. Current through the double dot is possible via the electron transfer process of the lower left inset of Fig.2.28b. Moving along ε_Σ towards upper right, the anti-symmetric state aligns with the leads. However, current is blocked, since an extra electron is already added to the double dot and the charging energy E_m is not available yet. Further along the line, the electrochemical potential for adding the second electron to the symmetric state aligns with the leads. As we assumed single occupation of the delocalized states, current is blocked here as well. When arriving at the upper right orange crescent, the electrochemical potential for adding the second electron to the double dot in the (empty) anti-symmetric state becomes available. This enables the hole transfer process of the upper right inset of Fig.2.28b. From this analysis, we deduce that the energy separation between the two orange crescents at ε_δ=0 is given by: $E_m + 2t$. We plot in Fig. 2.28c a line-cut of I_{SD} along the detuning axis ε_Σ for V_{SD}=0.7 meV, extracted from the color map Fig. 2.28a. We clearly observe two main peaks separated by ΔE_{peak}= 1.17 meV. As these two peaks result from the two configurations where the current is allowed (see the two insets of Fig.2.28b). Therefore, the peak separation $\Delta E_{peak} = E_m + 2t$. We extract $2t$=0.67 meV assuming E_m=0.46 meV as discussed in section 2.3.4. Therefore, this analysis of the Coulomb diamond map of the two-level system provides an estimation of $f_{res} = 2t/h$=0.167 THz, that is fully consistent with our estimation from Equation 2.25.

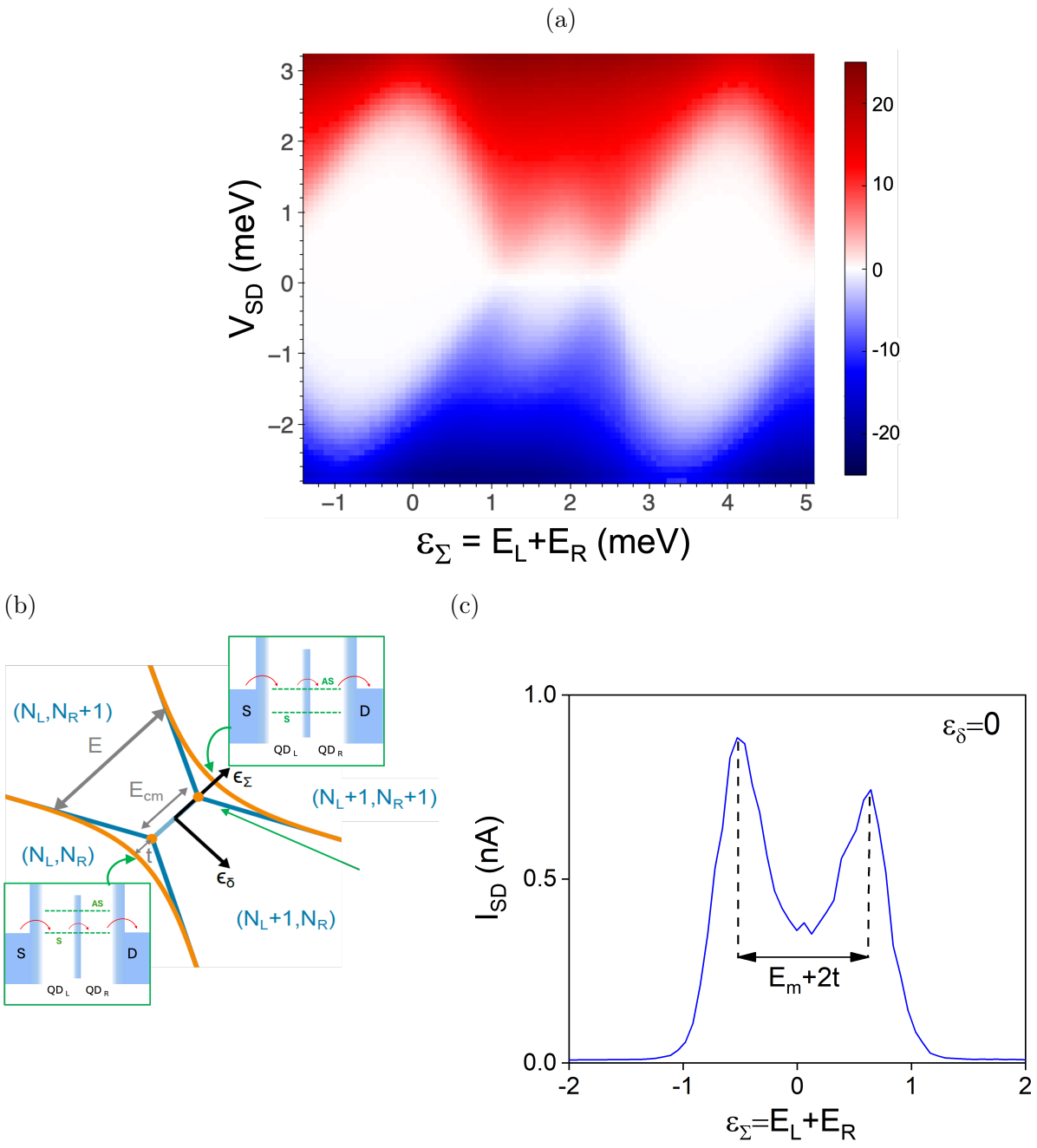

Figure 2.28: (a) Current I_{SD} as a function of the source-drain voltage V_{SD} and of the mean energy ε_Σ, exhibiting Coulomb diamonds. (b) Schematic of the region around an interdot transition. The orange circles are the triple points of the weakly coupled double dot showing a maximum current. The triple points of the weakly coupled double dot develop into the orange crescents in the strong coupling regime. The various configurations of the electrochemical potentials are also illustrated in the two insets. **c** Line-cut of I_{DS} as a function of the mean energy ε_Σ at V_{SD}=0.7 meV and ε_δ=0.

As presented in the previous chapter, the double GQD is inserted into the gap of a THz LC circuit resonator. The size of the gap is 2.7x2.7 μm^2 and the resonance frequency of the LC resonator is ~350 GHz. We had initially planned to probe the interaction of the double GQD with the THz vacuum field using dark transport spectroscopy measurements. Unfortunately, the resonance frequency of the two level system is limited to 0.17 THz which is well below the resonance frequency of the LC resonator. This frequency mismatch explains why we were not

able to observe a signature in the tunnel current of the ultra-strong coupling of the double GQD with the vacuum field.

As a conclusion, our study of the quantum transport through an etched double GQD, encapsulated by hBN layers, has revealed thaty by tuning the interdot coupling regime, a two-level system can be formed. We have demonstrated that the resonance frequency between the anti-symmetric and symmetric states of the two-level system lies in the range of 0.13-0.17 THz, i.e. in the THz spectral range. This result is a first step into the realization of new THz quantum technologies.

Bibliography

[1] M. A. Reed et al. "Observation of discrete electronic states in a zero-dimensional semiconductor nanostructure". *Phys. Rev. Lett.*, 60, pp. 535–537, 1988.

[2] C. W. J. Beenakker. "Theory of Coulomb-blockade oscillations in the conductance of a quantum dot". *Phys. Rev. B*, 44, pp. 1646–1656, 1991.

[3] Michel Devoret, Daniel Esteve, and C. Urbina. "Single-Electron Transfer in Metallic Nanostructures". *Nature*, 360, pp. 547–553, 1992.

[4] Sylvain Massabeau. "Optical and electronic properties of graphene quantum dots in the Terahertz spectral range". Theses. Sorbonne Université, Nov. 2020, 2020.

[5] Mônica A. Cotta. "Quantum Dots and Their Applications: What Lies Ahead?" *ACS Applied Nano Materials*, 3, 6, pp. 4920–4924, 2020.

[6] Maureen A. Walling, Jennifer A. Novak, and Jason R. E. Shepard. "Quantum Dots for Live Cell and In Vivo Imaging". *International Journal of Molecular Sciences*, 10, 2, pp. 441–491, 2009.

[7] Sheetal Devi et al. "Quantum Dots: An Emerging Approach for Cancer Therapy". *Frontiers in Materials*, 8, 2022.

[8] *Quantum dots – The future of Display Technology*. `https://xtpl.com/quantum-dots-the-future-of-display-technology/`. 11/04/24.

[9] Yedluri Anil Kumar et al. "Recent advancement in quantum dot-based materials for energy storage applications: a review". *Dalton Trans.*, 52, pp. 8580–8600, 2023.

[10] Nicolas Goubet et al. "Terahertz HgTe Nanocrystals: Beyond Confinement". *Journal of the American Chemical Society*, 140, 15, pp. 5033–5036, 2018.

[11] Thibault Apretna et al. *Nanophotonics*, 10, 10, pp. 2753–2763, 2021.

[12] T. Apretna et al. "Coherent THz wave emission from HgTe quantum dots". *Applied Physics Letters*, 121, 25, p. 251101, 2022.

[13] Abdel El Fatimy et al. "Epitaxial graphene quantum dots for high-performance terahertz bolometers". *Nature Nanotechnology*, 11, 4, pp. 335–338, 2016.

[14] Abdel El Fatimy et al. *Nanophotonics*, 7, 4, pp. 735–740, 2018.

[15] Elisa Riccardi et al. "Ultrasensitive Photoresponse of Graphene Quantum Dots in the Coulomb Blockade Regime to THz Radiation". *Nano Letters*, 20, 7, pp. 5408–5414, 2020.

[16] A. H. Castro Neto et al. "The electronic properties of graphene". *Rev. Mod. Phys.*, 81, pp. 109–162, 2009.

[17] A. Matulis and F. M. Peeters. "Quasibound states of quantum dots in single and bilayer graphene". *Phys. Rev. B*, 77, p. 115423, 2008.

[18] Pawel Bugajny et al. "Optical properties of geometrically optimized graphene quantum dots". *Physica E: Low-dimensional Systems and Nanostructures*, 85, pp. 294–301, 2017.

[19] H. Choi et al. "Broadband electromagnetic response and ultrafast dynamics of few-layer epitaxial graphene". *Applied Physics Letters*, 94, 17, p. 172102, 2009.

[20] Simon Messelot et al. “Large terahertz electric dipole of a single graphene quantum dot”. *Phys. Rev. Res.*, 4, p. L012018, 2022.

[21] T. H. Oosterkamp et al. “Photon Sidebands of the Ground State and First Excited State of a Quantum Dot”. *Phys. Rev. Lett.*, 78, pp. 1536–1539, 1997.

[22] L. P. Kouwenhoven et al. “Observation of Photon-Assisted Tunneling through a Quantum Dot”. *Phys. Rev. Lett.*, 73, pp. 3443–3446, 1994.

[23] Simon Messelot. “Terahertz Tamm cavities for light-matter coupling with graphene based materials”. PhD thesis. 2021, 2021.

[24] Luca Banszerus. “Gate-defined quantum dots in bilayer graphene”. Dissertation, RWTH Aachen University. PhD thesis. 2022, 2022.

[25] W. G. van der Wiel et al. “Electron transport through double quantum dots”. *Rev. Mod. Phys.*, 75, pp. 1–22, 2002.

[26] Benoît Neukelmance. “Spin-photon interface and quantum gates for spins in carbon nanotube.” Thèse de doctorat dirigée par Kontons, Takis EDPIF Université Paris sciences et lettres 2024. PhD thesis. 2024, 2024.

[27] C. Stampfer et al. “Tunable Graphene Single Electron Transistor”. *Nano Letters*, 8, 8, pp. 2378–2383, 2008.

[28] D. V. Averin and Yu. V. Nazarov. “Virtual electron diffusion during quantum tunneling of the electric charge”. *Phys. Rev. Lett.*, 65, pp. 2446–2449, 1990.

[29] Xing Lan Liu, Dorothee Hug, and Lieven M. K. Vandersypen. “Gate-defined graphene double quantum dot and excited state spectroscopy”. *Nano Letters*, 10, 5, pp. 1623–1627, 2010.

[30] Luca Banszerus et al. “Electrostatic Detection of Shubnikov–de Haas Oscillations in Bilayer Graphene by Coulomb Resonances in Gate-Defined Quantum Dots”. *physica status solidi (b)*, 257, 12, p. 2000333, 2020.

[31] F. Molitor et al. “Transport through graphene double dots”. *Applied Physics Letters*, 94, 22, p. 222107, 2009.

[32] Linjun Wang et al. “Controllable tunnel coupling and molecular states in a graphene double quantum dot”. *Applied Physics Letters*, 100, 2012.

[33] F. Molitor et al. “Observation of excited states in a graphene double quantum dot”. *Europhysics Letters*, 89, 6, p. 67005, 2010.

[34] Jian Zhang et al. “Double quantum dots in atomically-precise graphene nanoribbons”. *Materials for Quantum Technology*, 3, 3, p. 036201, 2023.

[35] Luca Banszerus et al. “Single-Electron Double Quantum Dots in Bilayer Graphene”. *Nano Letters*, 20, 3, pp. 2005–2011, 2020.

[36] L. Banszerus et al. “Tunable interdot coupling in few-electron bilayer graphene double quantum dots”. *Applied Physics Letters*, 118, 10, p. 103101, 2021.

[37] Olfa Dani et al. “Temperature-dependent broadening of coherent current peaks in InAs double quantum dots”. *Communications Physics*, 5, 1, p. 292, 2022.

[38] Y.-Y. Liu et al. "Photon Emission from a Cavity-Coupled Double Quantum Dot". *Phys. Rev. Lett.*, 113, p. 036801, 2014.

[39] "Non-symmetric Pauli spin blockade in a silicon double quantum dot". *npj Quantum Information*, 10, 1, p. 28, 2024.

[40] Artem O. Denisov et al. "Microwave-Frequency Scanning Gate Microscopy of a Si/SiGe Double Quantum Dot". *Nano Letters*, 22, 12. PMID: 35678453, pp. 4807–4813, 2022.

[41] Wilfred G. van der Wiel et al. "A Double Quantum Dot as an Artificial Two-Level System". *Japanese Journal of Applied Physics*, 40, 3S, p. 2100, 2001.

[42] T. Cubaynes et al. "Highly coherent spin states in carbon nanotubes coupled to cavity photons". *npj Quantum Information*, 5, 1, p. 47, 2019.

[43] Martin Raith, Peter Stano, and Jaroslav Fabian. "Theory of single electron spin relaxation in Si/SiGe lateral coupled quantum dots". *Phys. Rev. B*, 83, p. 195318, 2011.

[44] Martin Raith et al. "Electric control of tunneling energy in graphene double dots". *Phys. Rev. B*, 89, p. 085414, 2014.

[45] Seigo Tarucha et al. "Elastic and inelastic single electron tunneling in coupled two dot system". *Microelectronic Engineering*, 47, 1. New Phenomena in Mesoscopic Structures, pp. 101–105, 1999.

[46] Yuli V. Nazarov and Yaroslav M. Blanter. *Quantum Transport: Introduction to Nanoscience*. Cambridge University Press, 2009, 2009.

[47] T. H. Stoof and Yu. V. Nazarov. "Time-dependent resonant tunneling via two discrete states". *Physical Review B*, 53, 3, pp. 1050–1053, 1996.

[48] Yuli V. Nazarov. "Quantum interference, tunnel junctions and resonant tunneling interferometer". *Physica B: Condensed Matter*, 189, 1, pp. 57–69, 1993.

[49] Sami Sapmaz et al. "Excited State Spectroscopy in Carbon Nanotube Double Quantum Dots". *Nano Letters*, 6, 7. PMID: 16834409, pp. 1350–1355, 2006.

Chapter 3

Hybrid resonators based on Tamm cavities

The previous chapter of this thesis has shown that a double GQD acts as a two-level systems in the THz spectral range. This result represents an important milestone towards the development of THz quantum devices, which are currently under-developed. Another highly desired building block for the development of THz quantum devices are THz resonators. Indeed, by coupling a two-level system with a resonator it is possible to realise many functionalities for quantum technologies such as single-photon detectors by exploring a weak coupling regime, the generation of squeezed THz light by exploring a strong coupling regime and the detection of squeezed THz light by exploring an ultra-strong coupling regime.

A major difficulty in the realization of a THz resonator whose optical mode must couple efficiently to a discrete material such as a double GQD is the considerable gap between the typical wavelength in the THz spectral range, $\lambda \sim 300$ μm at 1 THz, and the material system size of a few hundred nanometers. A main challenge is therefore to design a THz resonator that can store and concentrate the electromagnetic energy of the resonant mode in the small area of the discrete material system. THz resonators that efficiently store electromagnetic mode energy as well as those that confine electromagnetic mode energy on sub-wavelength volume are widespread today. However, THz resonators that meet both criteria simultaneously, -storing electromagnetic energy and confining it to sub-wavelength dimensions- remain elusive so far.

In this chapter, we explore hybrid resonators based on Tamm cavities coupled to LC resonators. We will first present the basic of resonators and the state-of-the-art of resonators at THz frequencies. After, we will describe the properties and characterization of THz Tamm cavity. We will then report on our investigation of hybrid resonators based on Tamm-cavity coupled to LC circuit metamaterial and show that they combine efficient electromagnetic mode energy storage with electromagnetic mode energy confinement on sub-wavelength volume. Finally, we will present our research on the THz confined-mode Tamm cavity.

3.1 Basics of resonators

The control of light–matter coupling by embedding quantum matter into a photonic resonator is an essential ingredient for the development of single photon devices and cavity quantum electrodynamic studies and applications. The two main parameters of resonators that play a key role in light–matter coupling are the quality factor Q, which is proportional to the photon lifetime of the cavity, and the mode volume V, which quantifies the confinement of the electric field. In many cases, resonators associating strong electric field confinement, i.e. low V, and a high Q are highly desired. For instance, in the weak-coupling regime, the intensity of light–matter interaction is enhanced by the Purcell effect [1]. The latter describes the enhancement of spontaneous emission or absorption rates of emitters when placed into a resonant cavity. It is quantified by the Purcell factor F_P, which links the quality factor Q and the mode volume V of the resonant cavity:

$$F_P = \frac{3}{4\pi^2}\left(\frac{\lambda}{n}\right)^3 \frac{Q}{V} \tag{3.1}$$

with n the refractive index of the medium containing the emitter and λ the wavelength in free space. Therefore, the intensity of light–matter interaction in the weak coupling regime is enhanced by the ratio Q/V. Also, the coupling constant g that quantifies the light–matter coupling scales with $\sqrt{N_e/V}$, with N_e the number of elementary emitters in the matter part collectively involved in the interaction [2, 3, 4]. Thus, to reach the ultrastrong and deep-strong coupling regimes at the few electron level [5, 6, 7, 8, 9], ultra-small V are needed. Moreover, the in-depth study of the ultrastrong coupling regime requires a high degree of coherence of the light–matter coupling [10, 11, 12, 13, 14], quantified by the cooperativity $C = 4g^2Q/(\omega\gamma)$, with γ being the matter non-radiative decay rate and ω being the resonator mode angular frequency, which implies a high Q. In this context, a current challenge in the development of the light–matter coupling platform is to build resonators that conciliate a small V with a high Q, which represents an important challenge in the THz spectral range.

Quality factor Q The quality factor Q describes the enhancement of energy density inside the resonator when an external electromagnetic wave with a frequency matching the resonance frequency, ω is present. It also describes the linewidth of the resonance $\Delta\omega$, which represents the photon decay rate of the cavity Γ:

$$Q = 2\pi \frac{\text{Energy stored in the system}}{\text{Energy lost per cycle}} \qquad \text{and} \qquad Q = \frac{\omega}{\Delta\omega} = \frac{\omega}{\Gamma} \tag{3.2}$$

The linewidth depends on the total dissipation processes the cavity undergoes, represented by the total rate Γ : $\Gamma = \Gamma_{rad} + \Gamma_{loss}$ with Γ_{rad} the radiative coupling rate, Γ_{loss} the losses coupling rate. We can define the quality factor associated to these dissipation processes as followed:

$$Q_{rad} = \frac{\omega_r}{\Gamma_{rad}} \qquad Q_{loss} = \frac{\omega_r}{\Gamma_{loss}} \tag{3.3}$$

The total Q-factor then reads:

$$\frac{1}{Q} = \frac{1}{Q_{rad}} + \frac{1}{Q_{loss}} \tag{3.4}$$

Mode volume V The mode volume V is defined as [15] :

$$V = \int d^3\vec{r} \frac{\mid \epsilon(r)\vec{E}^2 \mid}{\mid \epsilon(r)\vec{E}^2 \mid_{max}} \tag{3.5}$$

where $\vec{E}$ is the electric field profile of the mode and ϵ the relative dielectric constant. The mode volume V is a measurement of the energy spatial confinement in the mode, as $1/V$ is the maximum energy density divided by the total energy. Note that this expression is used to quantify light-matter coupling as it is an indirect measurement of the electromagnetic energy density at the matter system position associated to a given photonic mode. It relies on an important assumption that the the dimensions of the matter systems are much smaller than the typical variation length of the resonator mode and where the entire matter system is subjected to an homogeneous electric field. This is totally justified in the case of a double GQD based device inserted in a THz resonator.

Considering the critical quantities Q and V, we can distinguish between two main types of resonator: propagation-based resonators and localized resonators. Propagation-based resonators allow light to travel through the device, while localized resonators confine it within a specific delimited region. We will detail the two types of resonator in the context of light-matter interaction.

3.1.1 Main classes of resonators

Electromagnetic resonators can be distinguished by the physical mechanism involved in the exchange of energy between the electric and magnetic fields at resonance, which depends on the relative weight of the two source terms in the fourth Maxwell equation: $\nabla \times \mathbf{H} = \mathbf{J} + \frac{\partial \mathbf{D}}{\partial t}$. The displacement current $\frac{\partial \mathbf{D}}{\partial t}$ leads to resonances effects arising from propagation effects and standing waves while the conduction current $\mathbf{J}$ from the interaction between at least two localized and possibly separate systems able to exchange energy. This gives rise to two classes of resonators: Propagation-based cavities (i.e. Fabry-Perot cavities) and localized component-based resonators (such as LC resonators). Todorov *et al.* present a comprehensive description of the difference between these two classes of THz resonators in [8], from which is reproduced Fig. 3.1.

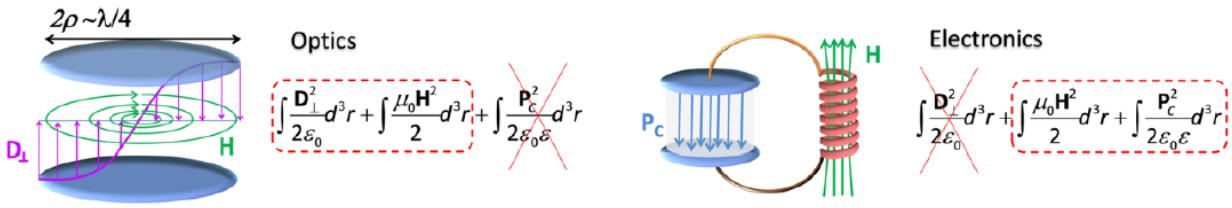

Figure 3.1: Schematic representation and associated Hamiltonian of two types of resonators. On the left, the propagation based resonators, or optics resonators, for which its Hamiltonian is dominated by the propagation wave effect (first term). On the right, the localized component-based resonators, or electronic resonators, for which the propagation term is negligible and the capacitive term dominates (third term). D refers to the transverse displacement field, H to the total magnetic field, and P_c to the polarization field inside the capacitor. Reproduced from [8].

- **Propagation-based cavities :** Propagation-based cavities rely on standing waves and the periodic energy exchange between the magnetic and electric fields is mediated by the displacement current. In the Hamiltonian description of the model reported in Fig. 3.1, the first propagative term is dominant and the capacitive term can be neglected. The resonator exists because it can fit a propagating wave in at least one direction. In this direction, the size of the resonator is therefore ultimately limited by $\lambda/2n$ (diffraction limit), where λ is the wavelength of the mode and n the refractive index of the material filling the resonator. As a result, the mode volume in these Fabry-Perot cavities is extremely large at THz frequencies (λ=300 μm at 1 THz), making them suitable for light-matter coupling involving very large numbers of electrons in spatially extended matter systems.

- **Localized component-based resonators :** Localized component-based resonators rely on the interaction between at least two localized elements able to exchange energy mediated by conduction currents. In the Hamiltonian description, the third capacitive term is dominant and propagation effects are neglected. As an example, for a resonator made of parallel plate capacitor with an inductive loop, the energy exchanged is mediated by currents flowing between the capacitor and the inductive loop. For localized component-based resonators, the space-time entanglement from propagating waves is lifted as the capacitive electric field contribution is quasi-static, and there is no necessity for a dimension of the resonator to be of the order of the wavelength λ, overcoming the diffraction limit for the mode volume. Thus, localized component-based resonators allow for strong electromagnetic confinement within deep sub-wavelength volumes. However, the quality factor of such localized component-based resonators are limited due to large radiative and ohmic losses.

3.2 State-of-the-art THz resonators

A large number of studies have been carried out on THz light-matter interaction involving these two classes of resonators. In the following, we present a brief review of previous research.

3.2.1 THz Fabry-Perot cavities

A Fabry-Perot cavity is composed of two mirrors facing each other and the resonance mechanism is phase matching after a round-trip inside the cavity, resulting in a constructive interference effect at specific frequencies. The mirrors are usually either metallic mirrors or Distributed Bragg Reflectors (DBRs). DBRs are realized by stacking dielectric layers of different refractive indexes n and of thickness $\frac{\lambda}{4n}$. It operates on the principle of constructive interference, which occurs at specific frequencies. There is no fundamental limit to the quality factor Q, the value of which depends on the materials used for the mirrors and the number of layers. DBRs based on dielectric materials with very low losses at THz frequencies, such as high-resistivity silicon/vacuum stacking, are preferred to achieve high Q factors. The ultrastrong light-matter coupling regime with high cooperativity has been recently studied using cyclotron resonances in a high-mobility two-dimensional electron gas (2DEG) coupled to various types of THz photonic resonators [16]. For example, using a THz Fabry-Perot cavity made of distributed Bragg

reflectors ($Q > 180$) (see Fig. 3.2a), Qi Zhang *et al.* have reported $g/\omega_0 \sim 0.1$ with $C > 300$ and shown that these unique conditions increase cyclotron resonance lifetime via the suppression of superradiant decay [17]. More recently, in a similar THz Fabry-Perot cavity, X. Li *et al.* have reported $g/\omega_0 \sim 0.36$ with a record-high cooperativity $C = 3513$, allowing the observation of a vacuum Bloch–Siegert shift in ultra-narrow Landau polaritons [18] (see Fig. 3.2a). Also, Mavrona *et al.* have demonstrated a cooperativity of $C = 57$ and $g/\omega_0 \sim 0.175$ using a Fabry-Perot cavity based on weakly transmitting hole patterned metal layer [19] (see Fig. 3.2b). However, these studies on THz light-matter coupling based on high-Q Fabry-Perot cavities, have involved a very large number of electrons N_e due to the large mode volume V, limited by diffraction to the order of $(\frac{\lambda}{2n})^3$.

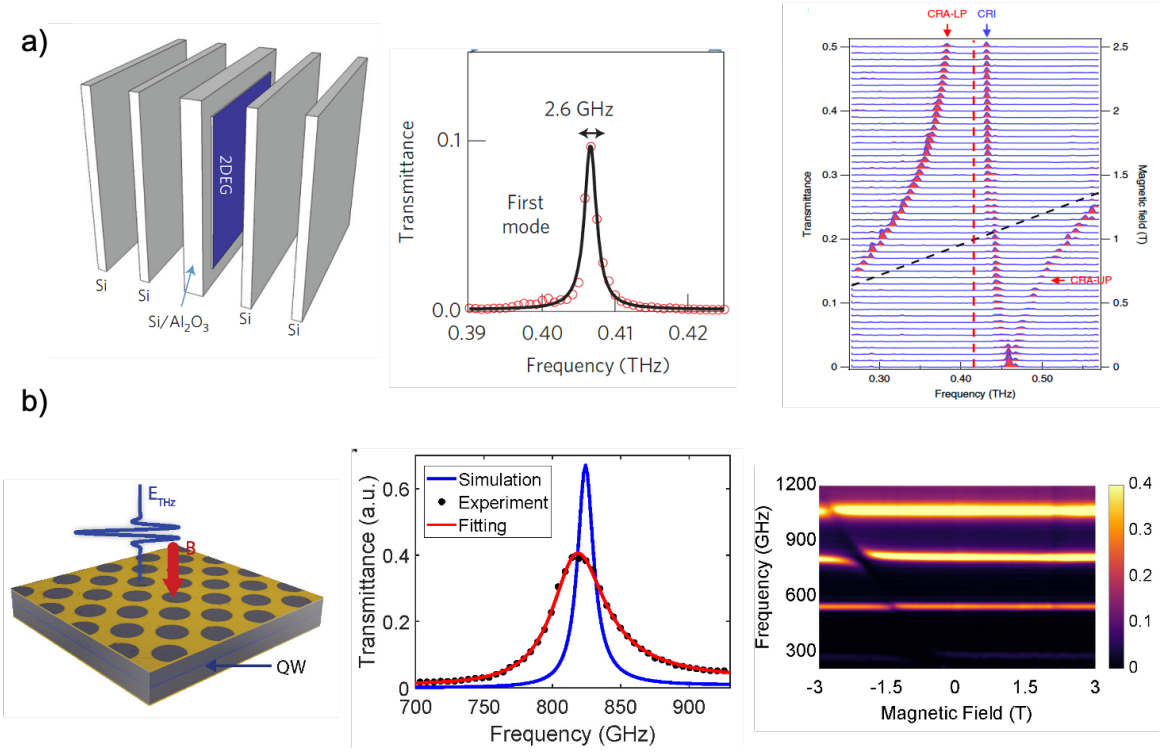

Figure 3.2: **(a)** Left: schematic of the THz Fabry-Perot cavity developed in [17] based on two silicon layers are placed on each side of the centre defect layer. The blue part is the transferred 2DEG thin film. Middle : experimental power transmittance spectrum for the cavity. Q value is 2.6 GHz (150), from [17]. Right: linearly polarized THz transmittance spectra where cyclotron resonances couple with the first-order cavity mode, from [18]. **(b)** Left: schematic representation of the Fabry-Perot cavity with quantum wells at the center of the cavity developed in [19]. Middle : experimental and simulated transmittance of the Fabry-Perot cavity. Right: transmission through samples for the first mode of the cavity revealing ultra-strong coupling regime, from [19].

3.2.2 THz LC circuit resonators

Among localized component-based resonators, LC circuit resonators are the most popular in the THz spectral range. They are often composed of split-ring resonators (SRRs) or their derivatives, arranged in a 2D metamaterials, forming arrays of sub-wavelength periodic structures that respond collectively to optical stimuli. By coupling LC resonators in metamaterials to

quantum well intersubband transitions and 2DEG Landau levels, ultra-strong coupling regimes have been successfully demonstrated [3, 20] (see Fig. 3.3a right). The typical SRR structure is composed by circular or rectangular rings, forming inductive loops, split by narrow capacitive gaps in which charge accumulation happens as illustrated in inset of Fig. 3.3a left. The transmission spectrum of the SRR structure presents two distinct resonances. The first mode is thus a LC circuit resonance as, at 0.50 THz, the 36 μm wide resonator is almost 5 times smaller than the wavelength in silicon λ/n= 170 μm (GaAs, n = 3.53). The second resonance at 2 THz is a propagation based resonance, often called dipolar mode, as the resonator size is of the order of the wavelength, λ/n= 42 μm.

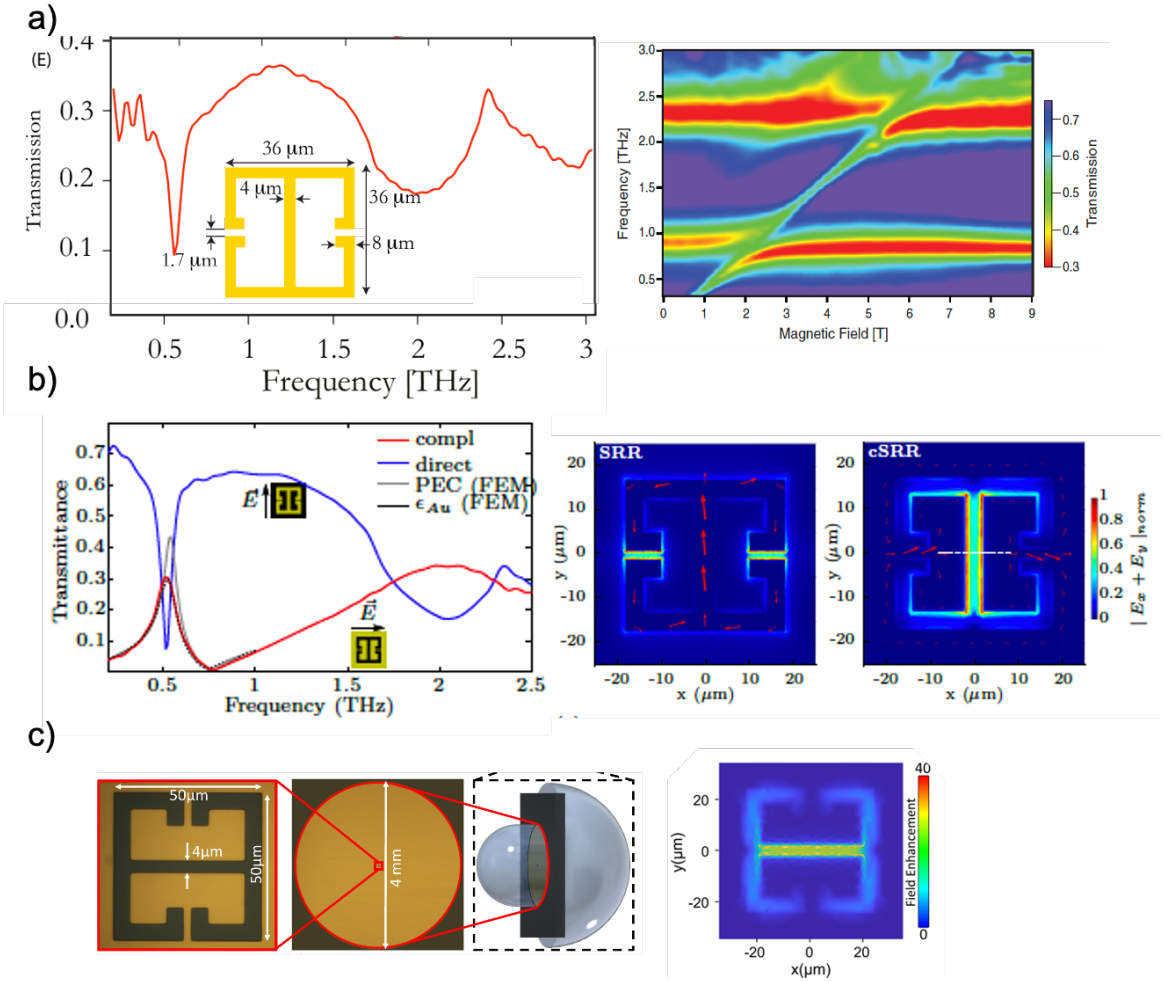

Figure 3.3: **(a)** Left: transmission spectrum of the SRR structure included in inset. Right: transmission of cyclotron transition of a 2DEG coupled to the metamaterial as a function of magnetic field, showing ultrastrong coupling regime. Adapted from [3]. **(b)** Left: complementary split-ring resonators show a complementary transmission spectrum (red curve) compared to their direct counterpart (blue curve). Right: simulations of the direct (left) and complementary (right) split-ring resonator showing the in-plane electric field distribution below the semiconductor surface (color scale) and the current distribution in the gold structure (red arrows), from [21]. **(c)** Left: optical images of the single resonator, of the whole sample and schematic of the configuration with Si lens. Right: simulated field enhancement at the resonator plane and at the resonant frequency, from [22].

Maissen *et al.* have used an alternative resonator design [21]: the complementary split ring

resonator (CSSR), where the metamaterial pattern is identical to the related SRR but metal and free substrate are inverted. The metamaterial is then a whole metallic plane including SRR shaped holes. The CSRRs and the usual direct SRRs share many reciprocal properties but CSSRs exhibit a transmission maximum at resonance unlike direct SRRs that exhibit a transmission minimum (see Fig. 3.3b left). Then, current confinement in CSSR is equivalent to electric field confinement in SRR, as the small capacitive gap of SRRs is replaced by a narrow metal strip in CSRR, as shown in Fig.3.3b right. As a consequence, the CSSR is designed to confine magnetic field around this narrow strip. Using a single complementary LC-circuit THz resonator as shown in Fig. 3.3c and two silicon lens, Rajabali *et al.* have recently achieved $g/\omega_0 \sim 0.33$ with $C = 94$ implying an estimated optically active electron number of only 30 000, and even of 2 000 with $C = 14$ [22]. Such a small number of electrons is obtained thanks to the confinement in truly all space dimensions of the electromagnetic mode which leads to a deeply sub-wavelength mode volume V, the cooperativity remaining nevertheless moderate due to the low Q factor typical of LC circuit resonators ($Q = 11$). This class of resonators exposed very low mode volume down to $V \sim 10^{-6}\lambda^3$ in the THz range thanks to the small capacitive gap. However, their quality factors are limited to typically $\leq$10 due to high ohmic loss in the metal and large radiative loss.

In a few words, these two classes of THz resonators exhibit distinct advantages and limitations based on their design. Fabry-Perot type resonators have high Q-factors (greater than 200) but their mode volume V is limited by diffraction to $(\frac{\lambda}{2})^3$. On the other hand, electronic circuits made of isolated miniature metallic structures, such as SRRs, have low Q-factors ($\leq$10) but their mode volume is not limited by diffraction and can be as small as $\sim 10^{-6}\lambda^3$. This state of the art clearly highlights the particular and difficult challenge of building THz electromagnetic resonators capable of conciliating low mode volume and high quality factor.

3.2.3 THz hybrid resonators

Potential candidates that have recently emerged to simultaneously achieve a high Q and a strong electric field confinement are hybrid THz resonators based on Fabry-Perot cavities coupled to LC circuit resonators. In these hybrid resonators, the strength of the coupling is given by the resonator-to-resonator coupling constant G defined by analogy to the light-matter coupling constant g. The ultrastrong coupling between a metamaterial based on THz LC circuit resonators and a THz Fabry-Perot cavity was first reported by Meng *et al.* [23], as illustrated in Fig. 3.4a. The authors have demonstrated nonlocal collective interaction of spatially separated metamaterial layers mediated by the cavity photons [23] and also the potential of these hybrid THz resonators for phase-sensitive THz detection of chemical and biological materials [24]. More recently, they have demonstrated ultra-strong coupling between the effective magnetic dipole moments of metallic complementary metasurfaces and the magnetic field of a cavity mode [25]. Also, Jeanin *et al.* have reported an hybrid THz cavity based on the coupling between LC circuit resonators and a dipolar antenna to engineer the radiative coupling properties and reach unity absorption [26] (see Fig. 3.4b).

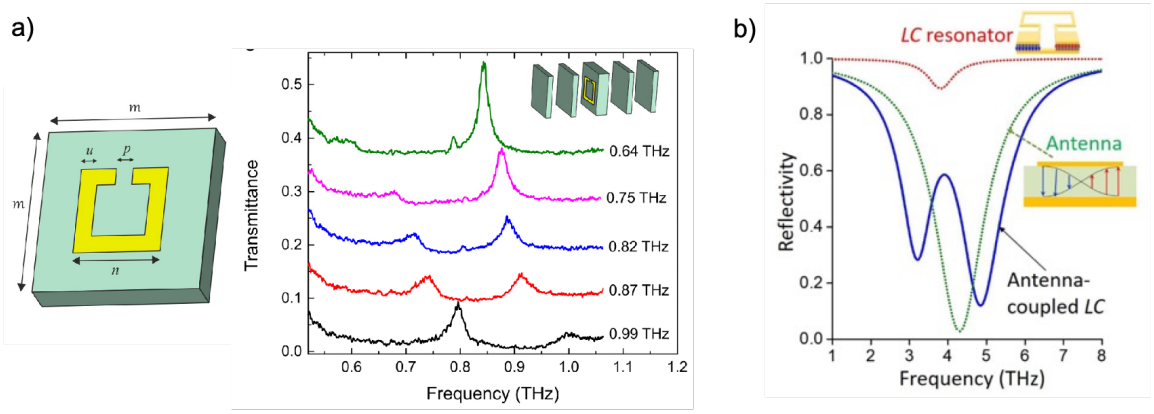

Figure 3.4: **(a)** Scheme of the SRR unit cell (left) and measured transmittance spectra with the SRRs positioned in the Fabry-Perot cavity, with the cavity mode fixed at 0.86 THz (right), from [23]. **(b)** Calculated reflectivity spectra of an array of LC resonators (red curve), of the same array coupled with antenna (blue curve) and of the antenna alone (green curve), from [26].

In this thesis, we aim at evaluating the potential of hybrid resonators to simultaneously achieve high Q and strong electric field confinement, with a perspective to coupling them to a double GQD. In this context, we have focused on a new class of hybrid THz resonators, Tamm cavities coupled to LC resonators, which have been patented by my thesis group.

3.3 THz Tamm cavity

In this section, we present the properties of basic Tamm cavities with resonance frequencies in the THz spectral range. The experimental results presented in this section are mainly taken from S. Messelot's thesis [27].

3.3.1 General description

A Tamm cavity is a Fabry-Perot cavity formed by a 1D photonic crystal or a DBR covered by a metallic layer acting as a second mirror, as illustrated Fig. 3.5a. This configuration creates a zero-length cavity and the photonic mode arises between them. Tamm cavities have been widely studied in the past decade in the visible and infrared range but has been subject to a very few numbers of studies in the THz spectral range [28, 29]. The frequency of the Tamm modes is determined by phase matching of a round-trip inside the cavity, similarly to common Fabry-Perot cavities. However, since there is no space between the two mirrors in Tamm cavity, this phase matching condition involves only the complex reflection coefficients of the DBR, r_{DBR}, and of the metallic mirror, r_{metal}. Hence, the phase matching criterion reads:

$$arg(r_{DBR}) + arg(r_{metal}) = 2\pi n \tag{3.6}$$

The "Tamm" cavity name refers then to an analogy with the electronic Tamm states which are surface states in semiconductor structures arising for electron energies within the material bandgap due to a disrupt of periodicity near the material surface [30]. Equation 3.6, that is referred to as phase matching condition, enables the prediction of the frequency of the resonant

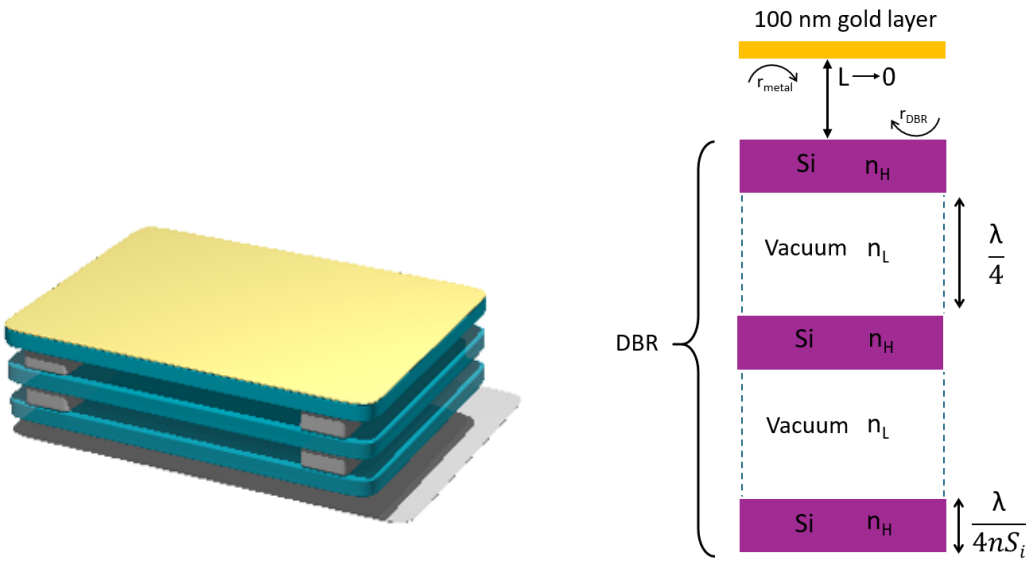

(a) (b)

Figure 3.5: **(a)** 3D representation of the 3 layers THz Tamm cavity including a gold top layer as mirror, silicon wafers (blue) and metal strips as spacers (gray). **(b)** Schematic association of a DBR and a metallic mirror resulting in a Tamm cavity. The DBR structure is an alternate of high (n_H) and low (n_L) refractive index layers.

Tamm mode.

In the following, we describe two main elements of the Tamm cavity: the DBR and the metallic mirror.

THz Distributed Bragg Reflector

To form the DBR in the THz Tamm cavity, we use a stack of thin silicon wafers and vacuum layers as an alternation of high (n_H) and low (n_L) refractive index quarter-wave layers, see Figure 3.6a. The high refractive index contrast between the silicon, n_{Si}=3.42 in the THz range, and the vacuum layers, n=1, makes it possible to realize DBR of high reflectivity and wide stop-band with a low number of layers. The stop-band frequency width Δf_{DBR} of the DBR is expressed as :

$$\frac{\Delta f}{f_{DBR}} = \frac{4}{\pi} arcsin\left(\frac{n_H - n_L}{n_H + n_L}\right) \tag{3.7}$$

with f_{DBR} the center of the DBR stop-band. This frequency is determined by the thickness of the high- and low-index layers and by number of periods, expressed due to the destructive interfence condition as :

$$f_{DBR} = (2p+1)\frac{c}{4e_i n_i} \tag{3.8}$$

with p an integer and $e_i n_i$ the thickness and refractive index product in layer i. The reflection spectrum of a DBR is periodic, the first stop-band is given by $p = 0$. To center the first stop-band at a frequency of 1 THz, the required condition for material thickness is $e_i n_i = \frac{\lambda}{4} = 75\mu$m. This implies that the silicon layers, whose refractive index is $n_{Si} = 3.42$, have a thickness of 22 μm and the vacuum layers have a thickness of 75 μm.

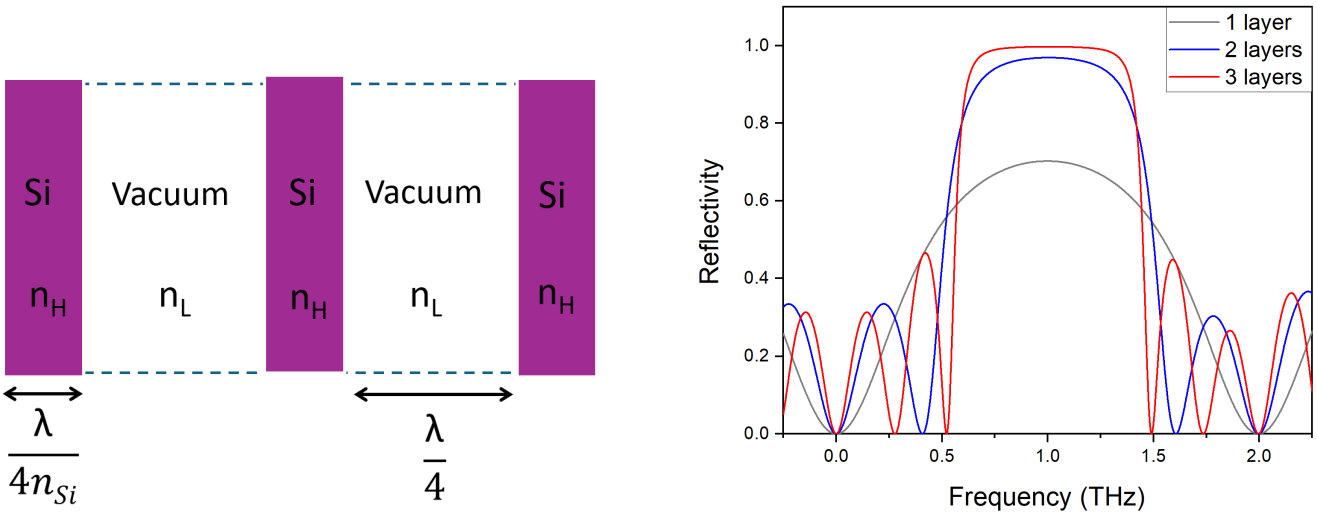

(a) (b)

Figure 3.6: **(a)** Schematic representation of the DBR structure used for the Tamm cavity. A 3 layered silicon DBR is represented, consisting in the stacking silicon-vacuum layers of $\frac{\lambda}{4n_{Si/vac}}$ thick. **(b)** Calculated reflectivity spectra of a 1, 2 and 3 silicon layers DBR structure, with $e_{Si/vac}n_{Si/vac} = 75\mu$m thick silicon and vacuum layers, respectively.

The optical properties of the DBR multilayer structure can be predicted using Transfer Matrix Method (TMM) simulations, by calculating the reflection, transmission, and absorption spectra as well as the profile of electric field of the mode. Here we calculate the properties of a DBR with a center frequency of the stop-band $\sim$ 1 THz by setting $e_i n_i = 75$ μm. The calculated reflection spectra of DBRs composed of 1, 2, and 3 silicon layers are depicted on Fig. 3.6b. We observe the high reflectivity achieved for only 3 layered DBR due to high refractive index contrast and the negligible THz conductivity of high-resistivity silicon ($\rho > 8000$ Ω.cm).

Since a thickness of 22 μm is very thin compared to standard silicon wafer thickness available in the market, $\frac{3\lambda}{4n_{Si}} = 66$ μm thick wafers were used instead. As shown in Fig. 3.7, this substitution does not affect the stop band's reflectivity at 1 THz. Indeed, the maximum reflectivity is unchanged in the center of the stop band. However, the DBR stop-band of the $\frac{3\lambda}{4n_{Si}}$ DBR is split in three smaller sub-stop-bands because of the frequency period divided by 3 associated with the tripled silicon thickness [31]. The central stop-band is about twice narrower for the $\frac{3\lambda}{4n_{Si}}$ DBR. In the following, we focus on the $\frac{3\lambda}{4n_{Si}}$ DBR structure as we will use it for experiments.

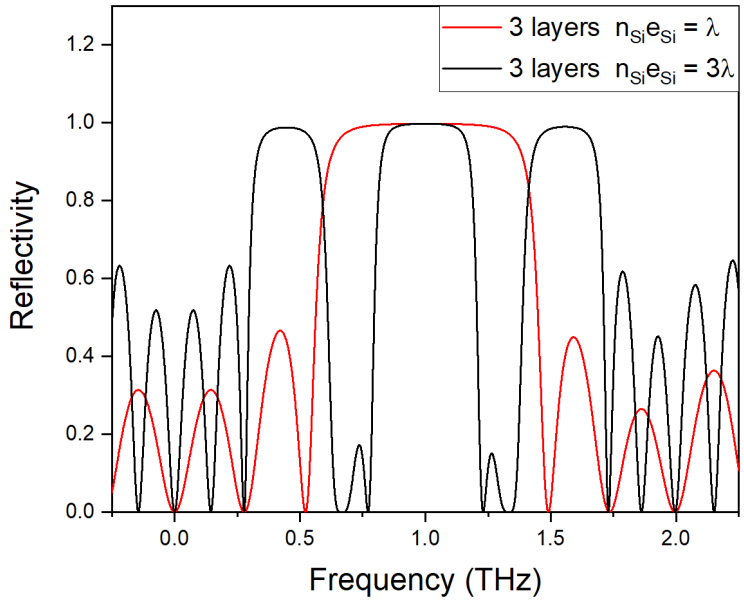

Figure 3.7: Comparison between reflection spectra of 3 silicon layers DBRs centered at 1 THz using $e_{Si} = \lambda_{1THz}/4n_{Si} = 21.94\ \mu m$ (black) and $e_{Si} = 3\lambda_{1THz}/4n_{Si} = 65.83\ \mu m$ (blue). $e_{vac} = 75\ \mu m$ for both.

THz mirror based on gold layer

The second mirror used to form a Fabry-Perot cavity is a metallic mirror made out of a gold layer deposited on the final silicon layer of the DBR. The gold is chosen for its high conductivity and low ohmic loss. As the penetration depth in the gold metal is $\delta \approx 80$ nm at 1 THz, we use a gold layer thickness of 100 nm, i.e. larger than δ. Figure 3.8 represents the power reflection coefficient $|r_{metal}|^2$ as well as the phase of the reflection coefficient $arg(r_{metal})$ of a gold layer (from Ref [27]). At 1 THz, the extrapolated power reflection coefficient is $|r_{metal}|^2 = 98.79$ %. A direct consequence of this perfect-like mirror behavior of a gold layer is that transmission is extremely low, beyond detectable limits at 1 THz.

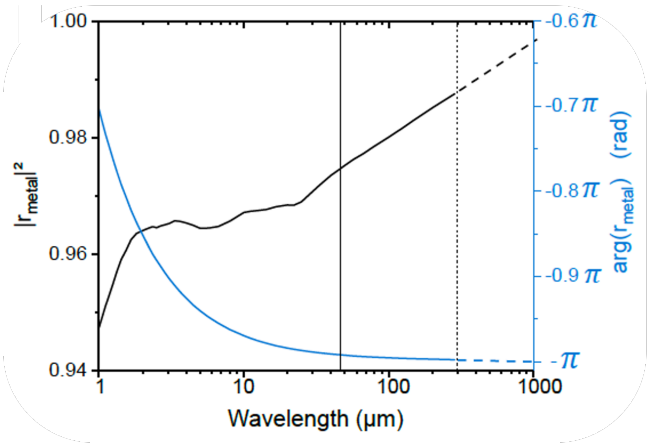

Figure 3.8: Power reflection coefficient $|r_{metal}|^2$of a gold mirror for an incident wave from silicon (black) and associated reflection phase $arg(r_{metal})$ (blue). Dashed lines are linear extrapolations and dotted vertical line stands for $\lambda = 300\ \mu$m or 1 THz. Adapted from [27]

.

3.3.2 Reflection properties

Figure 3.9 shows the calculated reflection spectrum of a Tamm cavity made up of a DBR with 3 silicon layers 66 μm thick separated by vacuum gaps 75 μm thick, and a gold mirror. For comparison, the calculated reflection spectrum of the 3 layers DBR is also reported. We clearly see that the association of the two mirrors results in the apparition of a sharp, high contrast resonance at the center of the DBR, at the frequency f_{DBR}=1 THz. The sharp resonance results in a high Q factor of 544, demonstrating the design of a high-Q THz cavity.

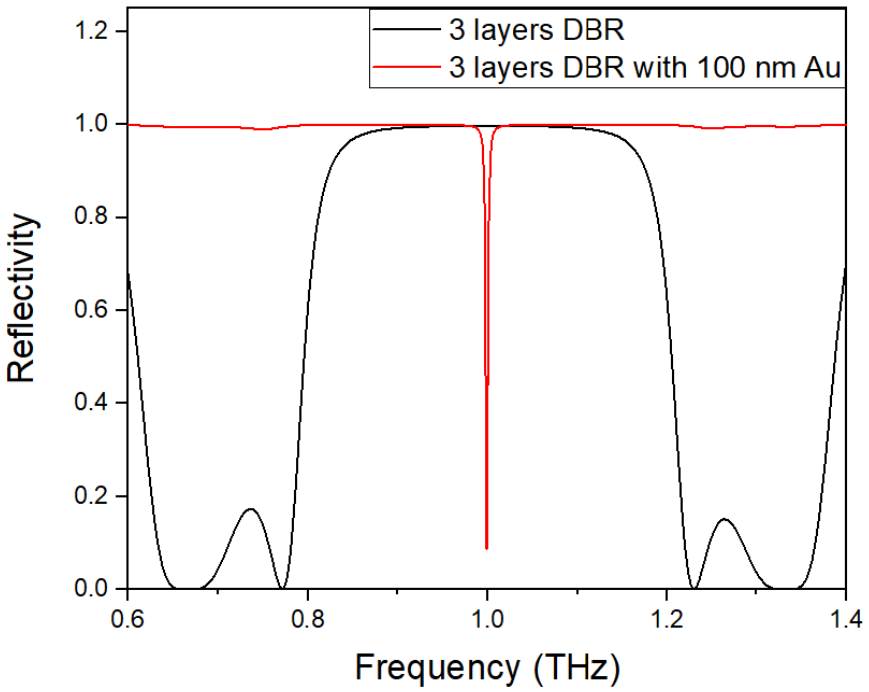

Figure 3.9: Simulated reflection spectra of a Tamm cavity composed of a 3 layers DBR (66 μm-thick silicon, 75 μm vacuum gaps) and a 100 nm-thick gold layer (red curve) and of the bare 3 layers DBR (black curve).

3.3.3 Electric field distribution

Using TMM, we compute the electric field profile inside the cavity for the fundamental mode at 1 THz for a 3 layers structure, as shown in Fig. 3.10. The electric field is represented normalized by the input wave amplitude, and then the relative electric field corresponds to the electric field enhancement factor due to the cavity. We observe that the amplitude maximum is located at the silicon-vacuum interface closest to the gold mirror, and its amplitude is enhanced by a factor as high as ∼8. We also observe a second maximum within the final silicon layer, which exists in the $\frac{3\lambda}{4n_{Si}}$ thickness of the silicon layer only and not for a $\frac{\lambda}{4n_{Si}}$ thickness silicon layer. Note that this electric field profile is of interest for light-matter coupling applications, and more particularly for coupling with a double GQD as fabricated and characterized in the previous chapters. Indeed, localized device based on 2D materials can be easily be deposited by usual transfer techniques on the free silicon-air interface, where the electric field is maximum. Also, the silicon layer can act as a back gate electrode for 2D material based devices deposited at this silicon-vacuum interface to control their chemical potential without introducing any

electromagnetic perturbation.

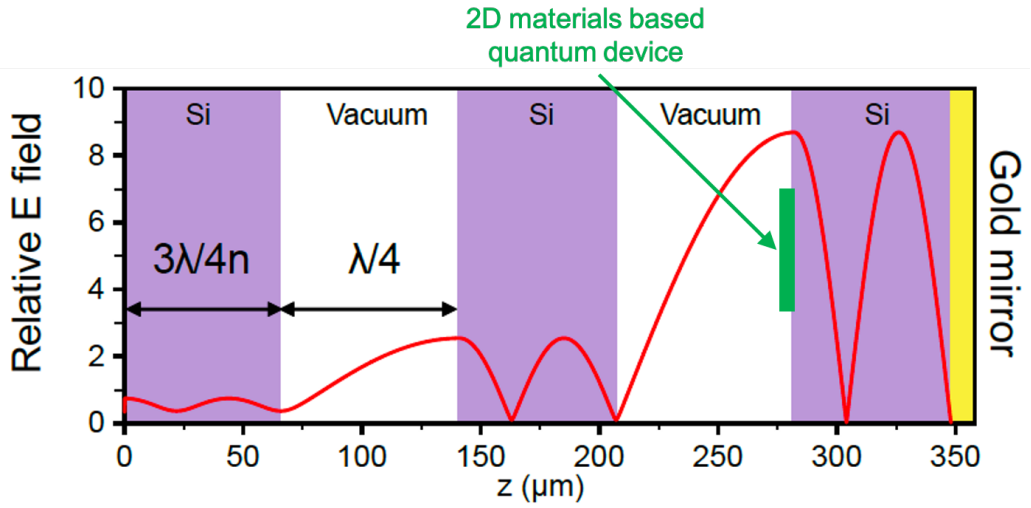

Figure 3.10: Electric field profile (amplitude modulus) of the resonant Tamm mode at 1 THz computed using TMM, superimposed to the cavity structure. The input incident wave is of normalized amplitude 1. Adapted from Ref [27].

3.3.4 Fabrication and characterization of Tamm cavity

The fabrication process of THz Tamm cavity is relatively straightforward, requiring 66 μm thick silicon wafers separated by a 75 μm thick metallic spacers to create the vacuum gaps (layers). The silicon layers are double side polished, of high resistivity, and supplied by the company Pi-Kem Ltd and the 75 μm metallic spacers were produced by the company Wipelec. We deposit a 100 nm gold layer on the top silicon layers of the DBR stack using thermal evaporation under vacuum at the LPENS cleanroom. We have developed a manual assembly procedure of the whole structure in which we use tweezers to stack the silicon wafers with intercalated metallic strips to create the vacuum gaps in a custom-made sample holder (see Fig. 3.11). The frequency resonance of the Tamm cavity is tuned by stacking silicon wafers of another thickness, separated accordingly.

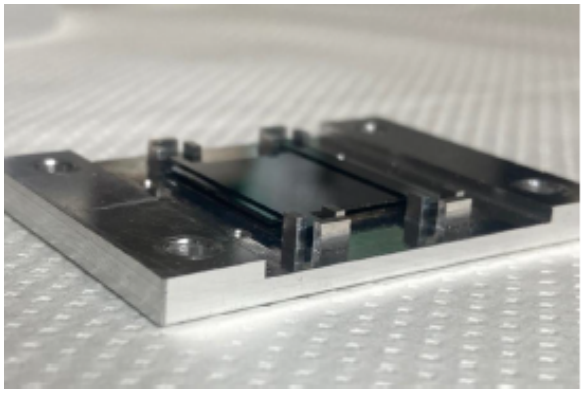

Figure 3.11: Photography of a Tamm cavity in its sample holder

To characterize the reflection of THz Tamm cavities, we use a Fourier Transform Infrared (FTIR) spectrometer based on a Globar thermal light source and a liquid helium-cooled bolometer detector. The spectral resolution of our FTIR spectrometer is 6 GHz. To overcome the limited resolution of our FTIR spectrometer, a series of experiments were performed by S. Messelot in collaboration with Pascale Roy and Jean-Blaise Brubach using SOLEIL synchrotron source and their Bruker IFS125 HR interferometer providing a spectral resolution as low as 0.6 GHz. Figure 3.12 shows the reflection spectrum of a 3 layers Tamm cavity, revealing a sharp resonance at 1.015 THz (extracted from [31]). The full-width at half-maximum (FWHM) of this Tamm cavity mode is ∼4.4 GHz corresponding to a quality factor as high as 230. The contrast reaches 50 %. It should be noted that the experimental Q is 2 times lower than that predicted by the simulations. This inhomogeneous broadening of the Tamm resonance is attributed to local variations in the layer thickness (∼100 nm) over the large THz beam area (∼1 mm).

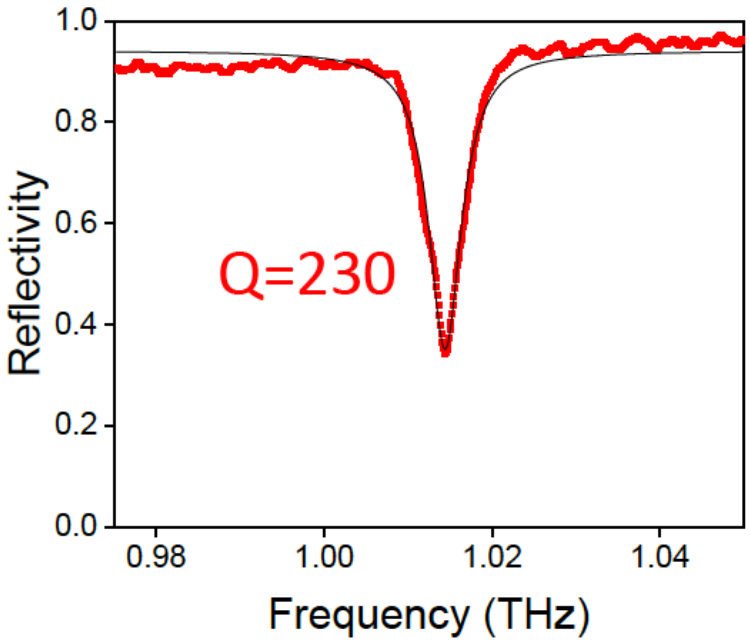

Figure 3.12: High resolution (0.6 GHz) reflection spectrum of a 3 layers Tamm cavity, measured using high resolution FTIR and synchrotron radiation. The FWHM of the Tamm resonance is 4.4 GHz corresponding to a Q of 230. Adapted from Ref [31].

THz Tamm cavities are therefore very promising propagation-based resonators for THz technology as they offer a large Q, up to 230. However, the volume of the Tamm mode is limited by diffraction to $\left(\frac{\lambda}{2n}\right)^3$. To overcome this limitation, we are taking advantage of the presence of a metallic mirror, which opens up new design possibilities by patterning the surface. In particular, our strategy is to pattern the metal to realise hybrid THz resonators. In the next section, we investigate the potential of hybrid resonators based on a Tamm cavity coupled to a LC metamaterial for achieving high Q factor and sub-wavelength electric field confinement in view of coupling efficiently a double GQD to a THz resonator.

3.4 Tamm cavity-LC metamaterial coupled resonators

In this section, we explore hybrid resonators based on the coupling of a Tamm cavity to LC resonators patterned on the gold mirror of the Tamm cavity. The works presented in this section, in which I was actively involved for the experimental part, were led by S. Messelot during his PhD in our team [27]. A large part of this section is reproduced in our publication in Photonics Research, "High Q and sub-wavelength THz electric field confinement in ultrastrongly coupled THz resonators" [32].

3.4.1 Different patterns of coupled resonators

As mentionned, an interesting feature of Tamm cavities is that they include a metallic mirror on which the metamaterial can be directly patterned on top. In this work, we integrate an inverted metamaterial into the gold mirror, i.e. we pattern arrays of holes in the mirror as resonators instead of direct SRRs. By doing so, we design hybrid resonators as represented in Fig. 3.13a. The metamaterial structure is fabricated by a simple optical lithography and the gold layer deposition via thermal evaporation process. After lift-off, it results in a 100 nm thick gold surface with an array of patterned LC holes. This pattern should not be mistaken for a complementary split ring resonator (CSRR) that is efficient for concentrating the magnetic field. Our resonators, shown in Fig. 3.13b, concentrate the electric field at its center, similarly to conventional split ring resonator, which is crucial for coupling it to matter systems involving the electric dipole interaction, such as a double GQD. For this reason, we call this pattern grid split ring resonators (GSRRs). Figure 3.13c reports the calculated transmission spectrum of an array of such LC structures of dimensions w=4.4 μm, l=4.4 μm, and L=16.5 μm. We observe a broad resonance at 1 THz with a linewidth Γ_{LC}=0.222 THz, which gives Q=4.5 (orange curve). The Tamm cavity, on its own, consists of a DBR composed of 2 layers of 66 μm-thick silicon ($\frac{3\lambda}{4n_{Si}}$), separated by 75 μm-thick vacuum layers, and a 100 nm-thick gold mirror deposited on the top silicon wafer of the DBR. The calculated reflection spectrum of this Tamm cavity exhibits a Tamm mode at 0.98 THz and a resonance linewidth of Γ_{Tamm}=0.098 THz, which gives Q=100 (black curve). The transmission spectrum of the complete hybrid structure in which the two resonators are coupled together (see Fig. 3.13a) , shows two well separated peaks at 0.84 and 1.13 THz, with quality factors of 15 and 20 (blue curve). As we will show in the following, the peak separation into two well defined peaks is an observation of the coupled modes and the frequency separation between the two peaks is a measure of the coupling energy G between the Tamm and LC metamaterial resonators.

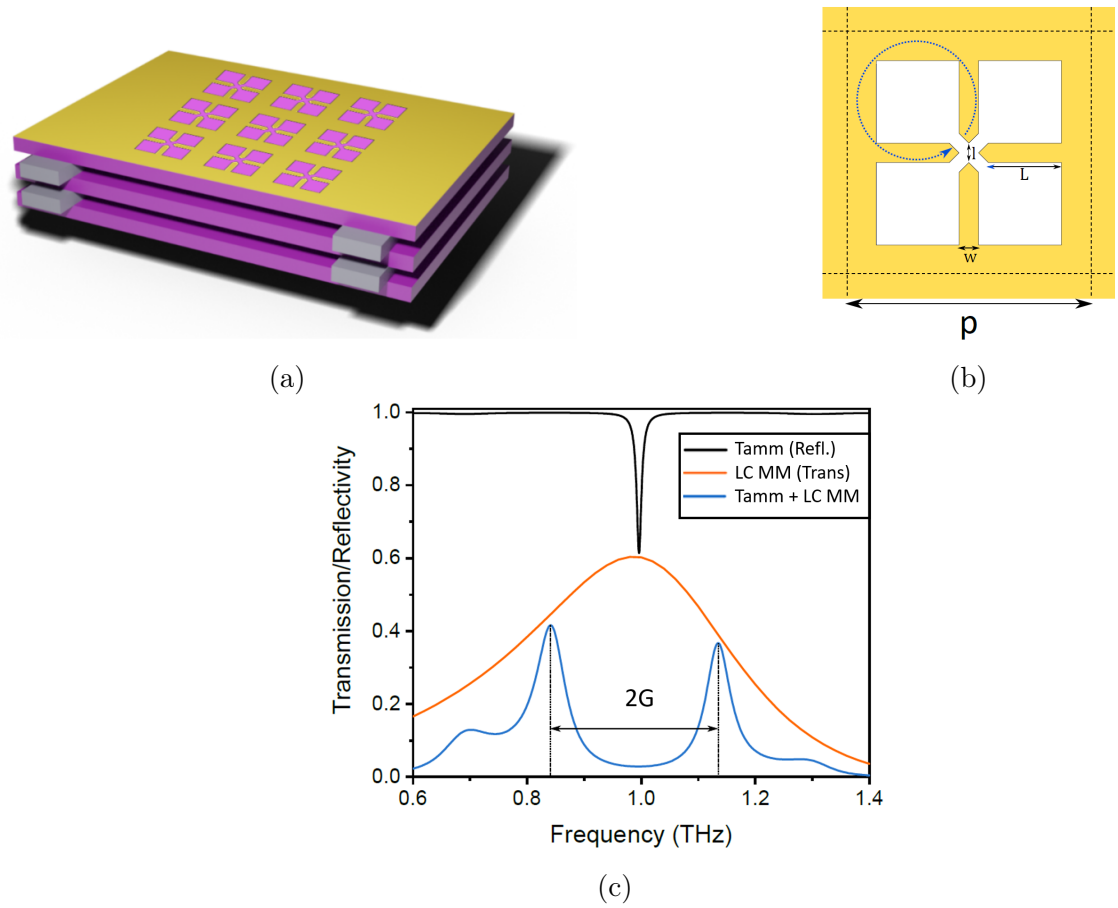

(a) (b)

(c)

Figure 3.13: Representation of the Tamm cavity/LC metamaterial coupled resonators structure **(a)** and unit cell pattern of the LC metamaterial **(b)**. **(c)** Calculated transmission and reflection spectra of the separated LC metamaterial and Tamm cavity, and of the coupled Tamm/LC metamaterial cavity (blue curve) which shows two well separated peaks separated by a distance 2G in frequency.

We experimentally investigate three different LC metamaterial patterns, designed to resonate at 1 THz. We study the GSRR for maximal electric field confinement (Fig. 3.14a), the cross pattern which is a rather usual reference for 2D metamaterial studies in the THz range (Fig. 3.14b), and the Complementary Split Ring Resonator (CSRR) that was reproduced from literature [20] (Fig. 3.14c). We use our FTIR spectrometer and a helium-cooled bolometer to record the reflection spectra of the three types of hybrid cavities.

- The transmission spectrum of the GSRR/Tamm hybrid resonator shows a frequency splitting of ≈290 GHz that demonstrates the coupling of the two resonators. The upper frequency peak is perturbed and seems to be split in two. This is due to its frequency that lies in the edge of the DBR stop-band.

- The transmission spectrum of the Cross/Tamm hybrid resonator also shows a coupling regime with two split peaks separated by ≈200 GHz. This value is overestimated since the resonance frequency of the fabricated Cross pattern is 0.93 THz, while the Tamm is 1 THz.

- The transmission spectrum of the CSRR/Tamm hybrid resonator does not show any peak

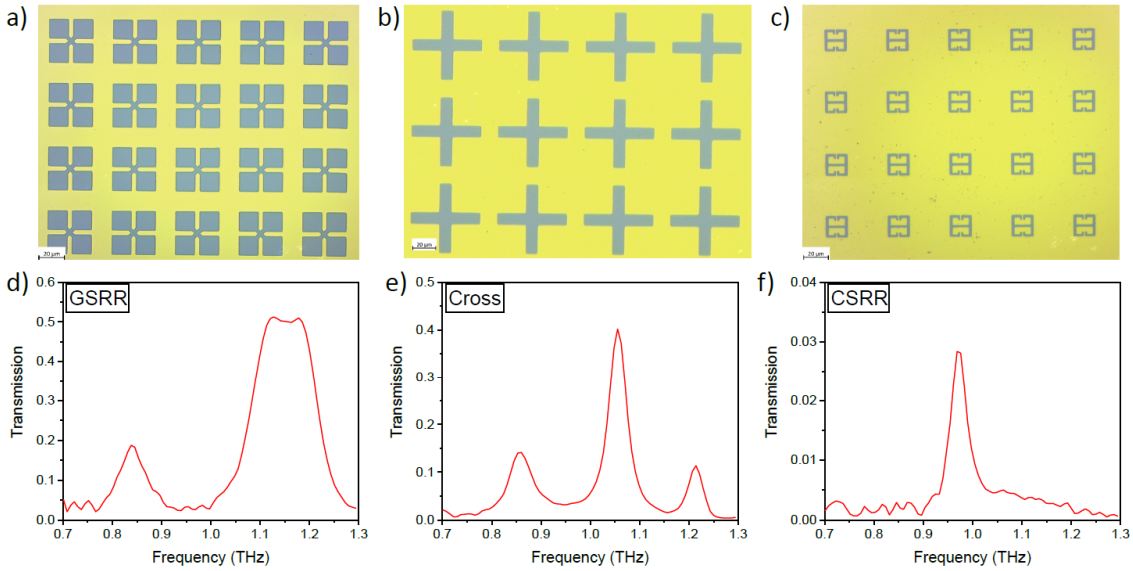

Figure 3.14: Optical microscope images of the patterned LC metamaterial on top of the Tamm cavity, with their associative transmission spectrum when set on top of the Tamm cavity. The left and right columns are the SRR and CSSR patterns as already presented, and the middle one is the cross pattern.

splitting, but we mainly observe a single sharp peak at 0.97 THz, corresponding to the Tamm resonance. As for the Cross pattern, we could not obtain sufficiently good matching between the resonance frequency of the uncoupled resonators. The CSSR fabrication process using optical lithography is challenging as the CSRR smaller dimensions are lower than 1 μm.

3.4.2 Quantum description of two coupled harmonic oscillators

To quantitatively describe the experimentally observed trends, S. Messelot has used a quantum formalism similar to the Rabi Hamiltonian, the Hopfield model, which involves bosonic operators only. In a general picture involving two resonators, creation and annihilation operators $a^\dagger, a, b^\dagger, b$ are associated with the photonic modes **A** and **B**. Here, **A** is the Tamm cavity mode, and **B** is the LC metamaterial mode. The Hamiltonian of the coupled resonators can then be expressed as :

$$H = \hbar\omega_A(a^\dagger a + \frac{1}{2}) + \hbar\omega_B(b^\dagger b + \frac{1}{2}) + \hbar G(a^\dagger b + ab^\dagger - ab - a^\dagger b^\dagger) \tag{3.9}$$

where G is the energy exchange rate between the two harmonic oscillators. The uncoupled eigenstates are written $\mid N_A, N'_B\rangle$ with N_A and N'_B the number of photons in modes **A** and **B**, respectively. Under the rotating wave approximation and considering for simplicity the subspace with one photon in the system, the eigenstates are then two coupled photonic modes $\mid \pm\rangle$ that are linear combinations of the uncoupled eigenstates $\mid 1_A, 0_B\rangle$ and $\mid 0_A, 1_B\rangle$:

$$| +\rangle = cos\,\theta \mid 1_A, 0_B\rangle + sin\,\theta \mid 0_A, 1_B\rangle \tag{3.10}$$

$$| -\rangle = sin\,\theta \mid 1_A, 0_B\rangle - cos\,\theta \mid 0_A, 1_B\rangle \tag{3.11}$$

where $\tan(2\theta) = -\frac{2G}{\delta}$. θ varies from 0 to $\frac{\pi}{2}$ with the resonator detuning $\delta = \omega_A - \omega_B$, describing the continuous transition from $\mid 1_A, 0_B\rangle$ to $\mid 0_A, 1_B\rangle$. For zero detuning, θ is set to $\frac{\pi}{4}$.
The lower $\mid +\rangle$ and upper $\mid -\rangle$ resonance frequencies read :

$$\omega_\pm = \frac{\omega_A + \omega_B}{2} \pm \frac{1}{2}\sqrt{(\omega_A - \omega_B)^2 + 4G^2} \tag{3.12}$$

These equations represent an anti-crossing pattern, with the minimal frequency difference occurring at zero detuning and equal to $2G$. It is important to point out that G defines the coupling constant between the two resonators, similarly to the light-matter coupling constant g involved in the Rabi Hamiltonian describing for instance a two-level system coupled to a resonator. At zero detuning, the linewidth of the coupled modes is the average values of the two uncoupled resonator linewidth :

$$\Gamma_\pm = \frac{\Gamma_A + \Gamma_B}{2} \tag{3.13}$$

Let us now discuss on the frequency splitting between the two peaks observed at zero detuning in the experimental transmission spectra of the hybrid resonators, reported in Fig. 3.14. The energy splitting is $\approx$ 290 GHz and $\approx$ 200 GHz for the SRR/Tamm hybrid resonator and the Cross/Tamm hybrid resonator, respectively. The theoretical description shows that, at zero detuning, the frequency splitting corresponds to $2G$. Therefore, we extract a reduced coupling constant $G/\omega \sim 0.1$ for both hybrid resonators, demonstrating the ultra-strong coupling regime between the Tamm cavity and the LC metamaterial in these hybrid resonators.

3.4.3 Strong coupling regime

In the following we only focus on the SRR/Tamm hybrid resonator as it presents the largest G coupling. In order to study in more depth the ultra-strong coupling regime between the SRR patterned metamaterial (LC metamaterial) and the Tamm cavity, we fabricate 9 different Tamm cavity-LC metamaterial coupled resonators. The Tamm cavity is composed of 2 silicon layers and its uncoupled resonance frequency remains constant at 1 THz. On the other hand, the resonance frequency of the LC structures is tuned by applying an homothetic transformation to the w, l, and L dimensions of the LC resonator, at a fixed period p = 65 μm (see Fig. 3.13b). Their resonance frequency, noted f_{LC}, ranges from 0.79 to 1.28 THz. Figure 3.15a reports the measured transmission spectra of the Tamm cavity-LC metamaterial coupled resonators for the 9 different f_{LC}. The resonance frequency of the uncoupled LC resonator f_{LC} is represented by colour dots. All the transmission spectra show two-well separated resonance peaks arising from the coupling between the two resonators. They correspond to the frequency of the upper and lower coupled modes f_+ and f_-, as described by Equation 3.12. Close to

the frequency matching between the two uncoupled modes, the two peaks are approximately symmetric and separated by an energy splitting of $2G = 0.2$ THz. The corresponding reduced coupling constant is $G/\omega \sim 0.1$. The resonance frequencies of the upper f_+ and lower f_- coupled modes are reported in Fig. 3.15b, as a function of f_{LC}. The evolution of the resonance frequencies clearly shows two distinct branches that form the anti-crossing pattern, similar to the behavior observed in strong light–matter coupling regime, demonstrating the ultra-strong coupling regime between the LC metamaterial and the Tamm cavity.

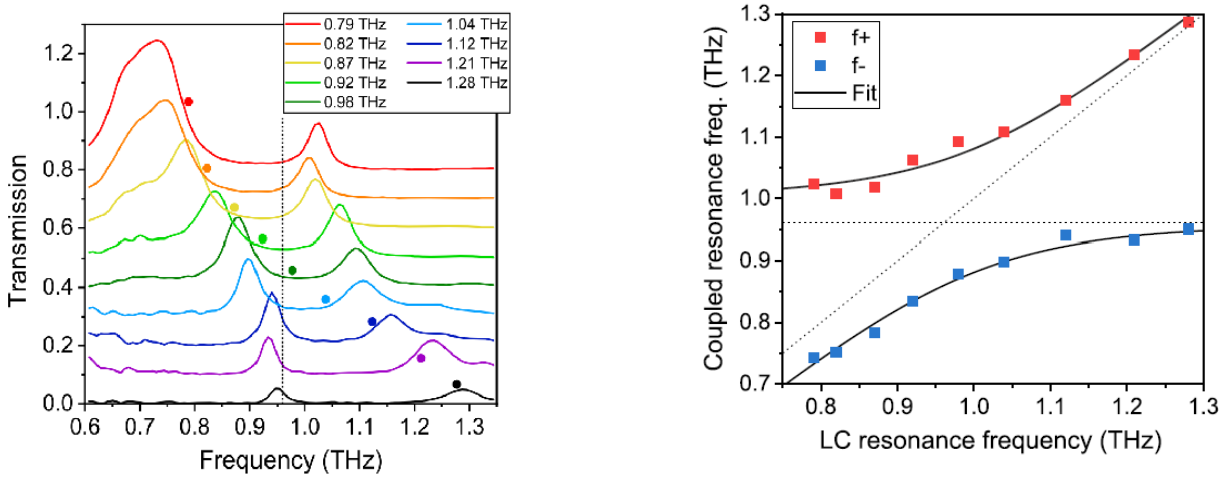

(a) (b)

Figure 3.15: **(a)** Transmission spectra of the Tamm cavity-LC metamaterial coupled resonatrors with decreasing LC resonance frequencies f_{LC}. The Tamm cavity resonance is fixed at 0.96 THz (vertical line) while f_{LC} is shited by homothetic transformation of their dimensions. **(b)** Resonance frequencies of the upper (red squares) and lower (blue squares) coupled modes, taken from (a), as a function of the LC resonance frequency. The horizontal and diagonal dotted lines represent the Tamm cavity and LC metamaterial resonances frequency, respectively.

In the next two sections, we examine an open question, namely what is the impact of the ultra-strong coupling regime between the two resonators on the Q-factor and the mode volume.

3.4.4 Quality factors

From the transmission spectra reported in Fig. 3.15a, we extract the linewidth of the two resonance peaks $\Gamma_\pm$ as a function of f_{LC}. The evolution of $\Gamma_\pm$ with f_{LC}, depicted in Fig. 3.16a, exhibit a crossing at zero detuning due to the exchange of properties between the fully Tamm and fully LC resonator configurations of the coupled modes. At the crossing, we measure $\Gamma_+ = 0.061$ THz and $\Gamma_- = 0.064$ THz. The associated quality factors of the two modes at zero detuning are Q_+=18 and Q_-=14, which are significantly larger than the Q factor of an uncoupled LC metamaterial equals to ~ 4. Such Q values are however surprising as the standard coupled modes theory predicts linewidth values of $\Gamma_\pm = \frac{\Gamma_{Tamm}+\Gamma_{LC}}{2} \sim 0.11$ THz, resulting in $Q_\pm \approx 9$ (see Equation 3.13).

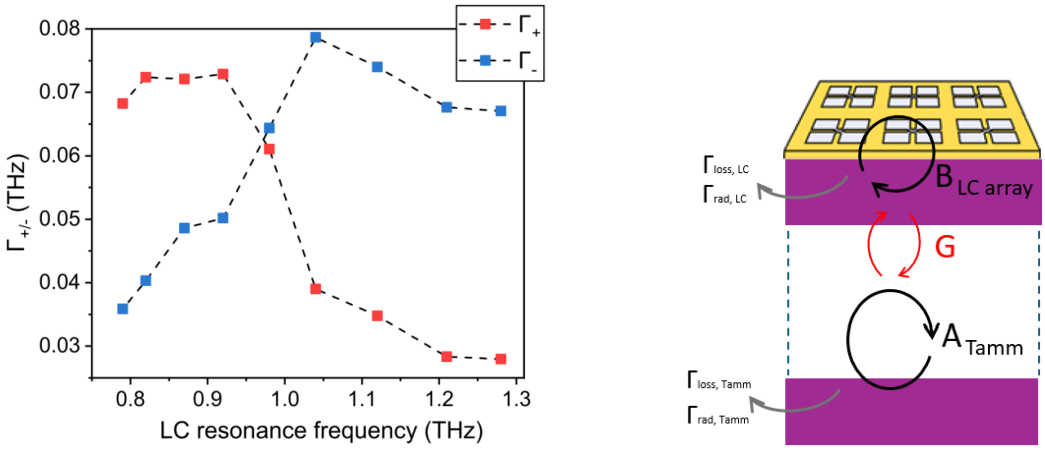

(a) (b)

Figure 3.16: **(a)** Resonance peak linewidth of the two coupled modes, determined by Lorentzian fits from Fig. 3.15a data. Dashed lines are guide for the eyes. **(b)** Schematic picture of the Tamm cavity and LC metamaterial directly on top, including radiative channels

However, when considering energy exchange between the resonators, the radiative loss of the LC metamaterial in the left direction and of the Tamm cavity in the right direction vanish as the energy emitted by the LC metamaterial in the left direction is absorbed by the Tamm cavity and reciprocally (see Fig. 3.16. Therefore, the linewidth of the modes are reduced to $\Gamma_{Tamm} = \Gamma_{rad1,Tamm} + \Gamma_{loss,Tamm}$ and $\Gamma_{LC} = \Gamma_{rad2,LC} + \Gamma_{loss,LC}$. $\Gamma_{rad1,Tamm}$ and $\Gamma_{rad2,LC}$ are the only remaining radiative losses as $\Gamma_{rad1,LC}$ and $\Gamma_{rad2,LC}$ cancel. The Equation 3.13 now becomes :

$$\Gamma_{\pm} = \frac{\Gamma_{rad1,Tamm} + \Gamma_{rad2,LC} + \Gamma_{loss,Tamm} + \Gamma_{loss,LC}}{2} \tag{3.14}$$

The coupling mechanism, which cancels $\Gamma_{rad1,LC}$ and $\Gamma_{rad2,LC}$, is responsible for the narrow resonance linewidths of the coupled modes, $\Gamma_{\pm}$, observed experimentally compared to those predicted by the standard theory of coupled modes. This explains the high Q_- and Q_+ values extracted from experimental transmission spectra. The large value of G observed experimentally is a direct consequence of the efficient radiative coupling properties of the LC metamaterial. Since there is no way to distinguish $\Gamma_{loss,Tamm}$ from $\Gamma_{loss,Lc}$ contributions as they both result from ohmic loss, we can write $\Gamma_{loss,metal} = \Gamma_{loss,Tamm} + \Gamma_{loss,LC}$. As the DBR is highly reflective, we assume $\Gamma_{rad1,Tamm} << \Gamma_{rad2,LC}$ and Equation 3.14 is approximated by :

$$\Gamma_{\pm} \approx \frac{\Gamma_{rad2,LC} + \Gamma_{loss,metal}}{2} \tag{3.15}$$

Equation 3.15 highlights the fact that $\Gamma_{\pm}$ can be ultimately reduced to $\frac{\Gamma_{loss,metal}}{2}$ by minimizing the radiative losses $\Gamma_{rad2,LC}$. To this aim, we add a supplementary mirror at a distance of 75 μm over the LC metamaterial to suppress radiative losses. We measure the experimental reflection spectra of two Tamm cavity-LC coupled resonators based on DBRs made of 2 and 3 layers, including the additional gold mirror blocking transmission. As observed in Fig. 3.17b, the spectra show two resonant peaks at resonance frequencies 0.84 and 1.06 THz, with Q_-=25 and Q_+=33 for the 2 layers hybrid cavity and Q_-=35 and Q_+=37 for the 3 layers hybrid cavity. The Q-factor is larger for the 3 layers hybrid cavity than for a 2 layers hybrid cavity

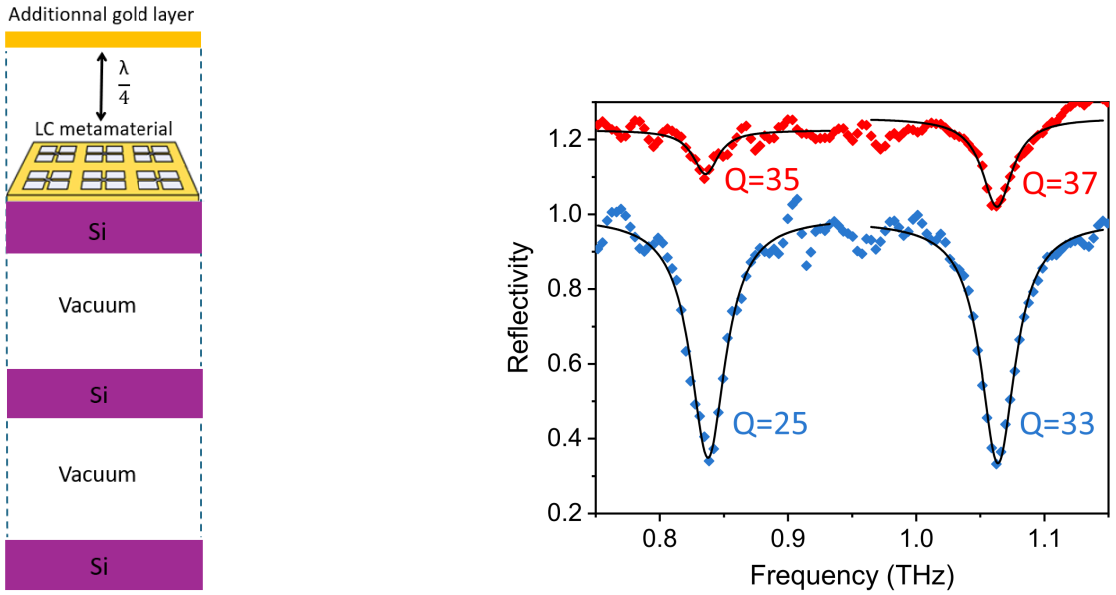

(a) (b)

Figure 3.17: **(a)** Schematic representation of the hybrid Tamm-LC cavity including an additional mirror for Q-factor optimization. **(b)** Experimental reflection spectra of 2 layers and 3 layers hybrid Tamm-LC cavities including an additional mirror.

due to the higher reflectivity of the DBR that reduces $\Gamma_{rad1,Tamm}$. This analysis shows that our original approach provides an enhancement of the Q-factor by a factor 8 over the uncoupled LC metamaterial, owing to the suppression of the dominant decay rate that is the radiation loss rate of the LC metamaterial. The Q-factor is thus only limited by the ohmic losses in the metallic layer.

3.4.5 Mode volume

We now describe how the mode volume of the resonators evolves in the ultrastrong coupling regime. The unit pattern of the LC metamaterial is designed to concentrate the electric field in the central capacitive gap between the metallic tips. Using the eigenfrequency solver of COMSOL Multiphysics, the electric field distribution of the lower and upper frequency resonant modes of the coupled resonator is calculated. Figure 3.18a displays the simulated in-plane electric field amplitude enhancement profile of the upper coupled mode in the LC unit cell plane, at the resonance frequency f_{LC}=1 THz compared to an input plane wave of unity amplitude. The electric field is increased up to a factor 20 close to the edges of the metallic tips and to 13 between the metallic tips.

Figure 3.18b reports the calculated mode volume of the upper and lower coupled modes $V_{\pm}$ at their respective resonance frequency $\omega_{\pm}$, normalized by V_{LC}, as a function of the detuning (increasing values of f_{LC}) and for a fixed Tamm resonance frequency f_{Tamm}=1 THz. V_+ and V_- show opposite evolution with the detuning, and cross at zero detuning. The evolution reflects the continuous transition of the upper coupled mode from a mode mainly given by the Tamm mode to an LC metamaterial mode for increasing resonator detuning, and inversely for the lower coupled mode, in the same way as the anticrossing measurement (Fig. 3.15b). V_+ and

V_- converges toward V_{LC} at large positive and negative detuning, respectively. The crossover indicates the exchange of mode volume properties between the two resonators. At zero detuning, the mode volume is increased by only a factor of 2 compared to V_{LC} : $V_\pm = 2V_{LC}$ because of the coupling. It highlights the fact that the mode volumes of the coupled resonator systems are dominated by the metamaterial mode volume at small detuning. The mode volumes at zero detuning are reduced down to $3.2 \times 10^{-4}\lambda^3$ for V_- and $2 \times 10^{-4}\lambda^3$ for V_+, revealing a high degree of subwavelength confinement of the coupled modes. In his PhD, S. Messelot has provided insight on the origin of the factor 2 in the increase of $V_\pm$ compared to V_{LC}, by using quantum theory of coupled resonators based on the Hopfield model as reported in the previous section [27]. The factor 2 can be interpreted as the dilution of the photon electromagnetic energy in the two resonators. Achieving mode volumes of coupled modes only 2 times the mode volume of the uncoupled LC metamaterials is then a general result that can be transposed to other coupled systems based on metamaterials and Fabry–Perot cavity.

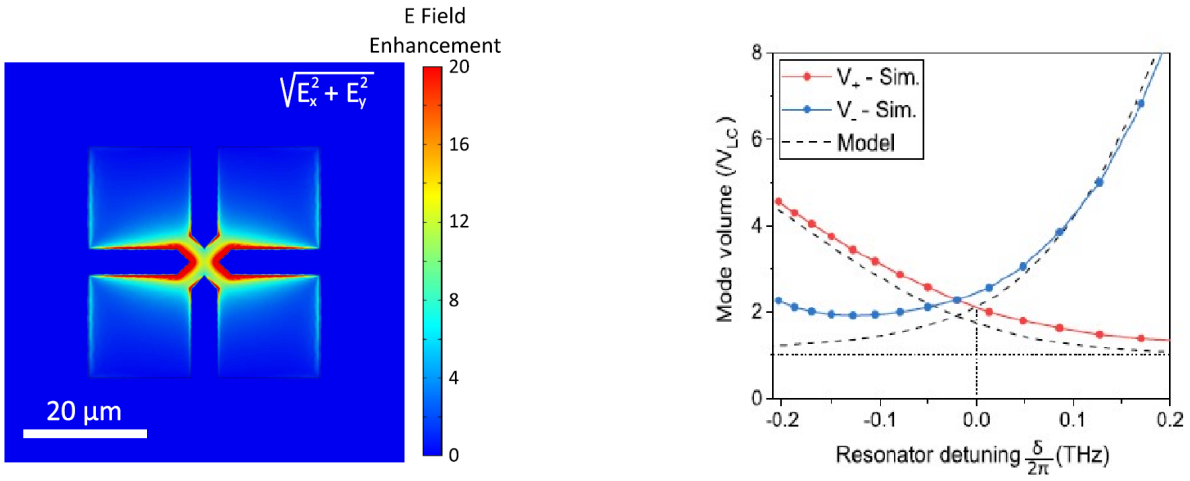

(a) (b)

Figure 3.18: **(a)** Simulated spatial profile of the electric field distribution over a single unit cell of LC resonator. In-between the metallic tips at the center of the cell, the electric field is 13 times stronger than the input wave of amplitude 1 due to the coupling with Tamm cavity, while the maximum enhancement is around 20, closer to the tips. **(b)** Mode volume of the upper (red) and lower (blue) frequency coupled modes, normalized by the mode volume of the uncoupled LC resonator V_{LC}, as a function of the resonators detuning δ. The Tamm resonance is fixed at 1 THz. The horizontal dashed line is the uncoupled mode volume of LC resonators V_{LC}.

This experimental and theoretical study demonstrates that original hybrid THz cavities based on the ultra-strong coupling between a THz Tamm cavity and an LC circuit metamaterial conciliates high quality factors, Q $\approx$ 37, with sub-λ electric field confinement, down to $2\times10^4\lambda^3$. Our work shows that the principal qualities of resonators, which are a high Q for Tamm cavity and a low V for LC circuit metamaterials, act beneficially in the ultra-strong coupling regime. The main strength of LC metamaterials, which is their ability to highly concentrate electric field, is preserved despite their coupling to a large mode volume propagation-based cavity. A strong concentration of the electric field is reached in the gap of the LC unit cell, i.e. between the metallic tips. These hybrid cavities are thus very promising for the development of advanced

THz devices exploiting light-matter interactions, which are highly desired for THz quantum technologies.

3.4.6 Towards coupling to a discrete matter system

The hybrid resonators presented in previous sections are based on planar Tamm cavities, which means that although the electric field is highly confined within the gaps of the LC resonators, it nevertheless extends over a very large number of unit cells in the 2D plane of the metamaterial. The LC unit cells of the metamaterial are thus collectively involved in the interaction with the electromagnetic field. These hybrid resonators are therefore ideally suited to the study of light-matter coupling in extended material systems such as 2D electron gas based materials. However, these hybrid resonators are not adapted for coupling with discrete material systems such as quantum dots, which require the electromagnetic mode of the cavity to be confined to three-dimensional space. A major challenge is to get beyond the metamaterial and couple the Tamm cavity to a single LC resonator.

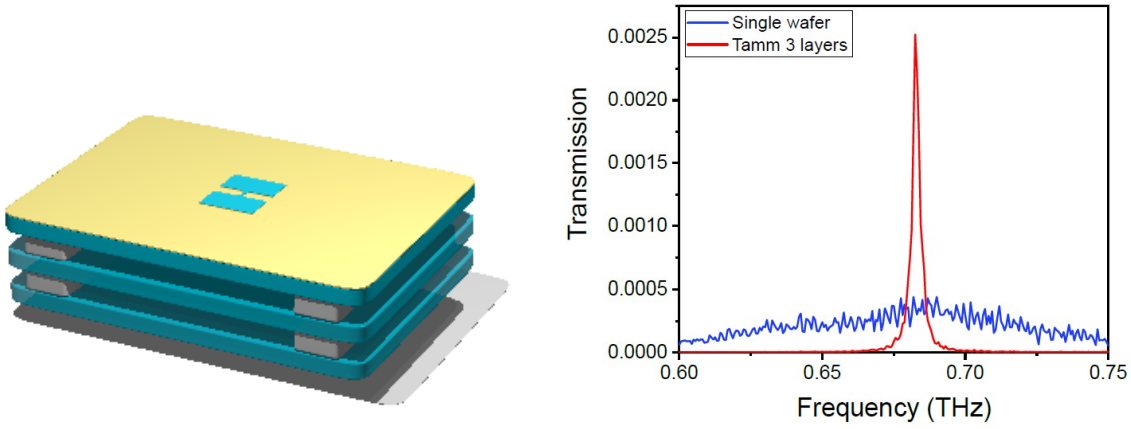

(a) (b)

Figure 3.19: **(a)** Schematic representation of a single LC cell on top of a Tamm cavity. The small-period array of LC metamaterial has been replaced with a diluted one, i.e a single LC cell. **(b)** Transmission spectrum of the array of diluted LC resonators, showing the effect of the coupling to the Tamm cavity when the final layer is on top of the DBR (red) or not (blue).

A preliminary step in this direction is to study an hybrid resonator based on the coupling of a Tamm cavity with a very dilute metamaterial, i.e. whose LC resonator unit cells are separated by a large distance. To this aim, we fabricate an hybrid cavity composed by a Tamm cavity resonating at 700 GHz and a LC metamaterial on top of the Tamm cavity with a period of unit cell p=1 mm, i.e. larger than the THz wavelength, to mimic an isolated LC resonator as illustrated in Fig. 3.19a. Because of the very low density of resonators on the surface, the transmission of such hybrid resonators is very low and we were unable to measure it using our FTIR spectrometer. We collaborate with Jean-François Lampin from IEMN laboratory, Villeneuve d'Ascq, who performed transmission measurements using a Vector Network Analyser (VNA) on Tamm cavity/LC coupled resonators centered at 700 GHz. The advantages of the VNA instrument are its high dynamic range, up to 80 dB, and its very high frequency resolution.

The Tamm cavity and the LC resonance frequencies are adjusted to 700 GHz by applying a scale factor 1/0.7 to the DBR layers thicknesses (e_{Si} = 94 μm and e_{vac} = 107 μm) and the LC dimensions because the VNA setup operates in the 500-750 GHz frequency range. Figure 3.19b shows the power transmission spectra of the hybrid resonator composed by a Tamm cavity resonating at 700 GHz and a diluted LC metamaterial. We observe a sharp resonance peak at 0.683 THz with Q∼240. The absence of peak splitting indicates that the strong coupling regime is not reached, unlike in the case of a dense array of LC unit cells. This is due to the fact that the Tamm-LC metamaterials coupling energy G scales as $\sim \sqrt{N_{LC}}$ with N_{LC} the number of LC resonators involved in the interaction. Here, the LC resonators are too diluted to provide a collective contribution, $N_{LC} \to 0$ leading to a weak coupling regime. However, the addition of the high-Q Tamm cavity is responsible for the large enhancement of the energy absorption in the photonic mode of the isolated LC pattern, as revealed by the difference between the transmission spectra of the LC resonators weakly coupled to the Tamm cavity (red) and of the same LC resonators on a single thin silicon layer (blue).

The absence of strong coupling between the two resonators is due to the small number of LC resonators which overlap with the photonic mode of the Tamm cavity. Thus, our approach reaches its limits and is not optimal for coupling these hybrid cavities to a discrete material system asuch as a double GQD. In this thesis work, we aim to overcome this issue by reducing the in-plane spatial extension of the Tamm mode and thus improve its interaction with a single LC resonator. This involves confining the photonic Tamm mode in the plane of the layers. To laterally confine the Tamm mode and consequently the coupled modes, our strategy is to limit the spatial extension of the metallic mirror of the Tamm cavity to a dimension typical of the wavelength by replacing the metal layer with a metal disk of finite size, as shown in Fig. 3.20. The cavity Tamm is then referred to as a confined-mode Tamm cavity.

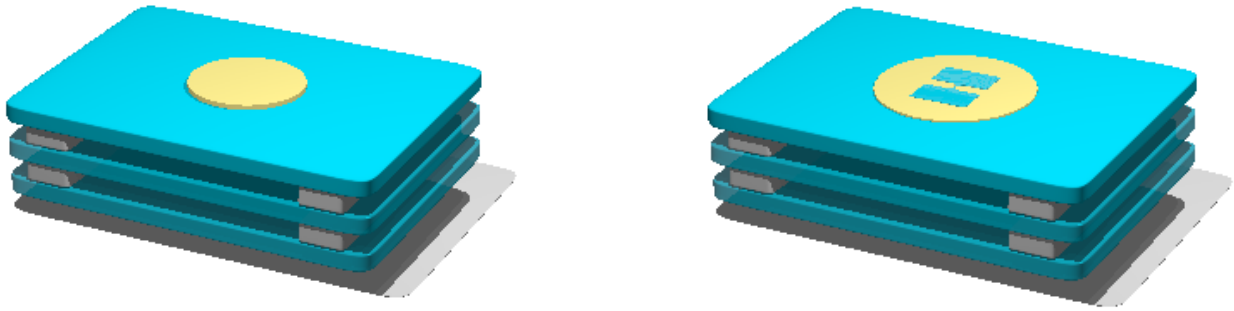

(a) (b)

Figure 3.20: **(a)** THz confined-mode Tamm cavity composed of a 3-layer silicon DBR and a gold disk with a diameter of the order of the wavelength. **(b)** New hybrid resonator design based on a THz confined-mode Tamm cavity coupled to a single LC resonator optimized for future studies of THz light-matter coupling with a double GQD.

In the latter part of this chapter, we present our work on THz confined-mode Tamm cavity. Studies of hybrid cavities based on a THz confined-mode Tamm cavity coupled to a single LC resonator are beyond the scope of this thesis, due to limited time available for the thesis, and will be carried out as part of the thesis of Alexis Wietzke, which will follow on from this work.

3.5 THz confined-mode Tamm cavity

To study THz confined-mode Tamm cavities, we implement a new set-up optimised for their characterization. Indeed, the THz beam probing these cavities must be highly focused because the diameter of the metallic disk is of the order of λ, which is not easily achievable with our FTIR spectrometer. In addition, the limited 6 GHz resolution of our FTIR spectrometer prevents accurate measurements of high Q factors. In this section, we present a new measurement set-up based on an electronic THz source that we have implemented to characterize THz confined-mode Tamm cavities. We also report a first series of measurements on basic Tamm cavities to optimize our fabrication and stacking procedure and on a confined-mode Tamm cavity.

3.5.1 Description of the set-up

The set-up includes a commercial amplifier/multiplier chain from Virginia Diodes, Inc. as an electronic THz source. The THz source consists of a multiplication chain (x54) driven by a 0-20 GHz synthesiser. The coherent emitted THz radiation can be tuned from 500 GHz to 750 GHz with an average power of 15 μW. The THz radiation can also be modulated in amplitude by a low-frequency ac voltage applied to the synthetizer. The THz beam delivered by the source and its horn antenna is collimated using a Zeonex lens L_e of 1 inch diameter and f-number=2, which transmits 91% of incoming light at 700 GHz. The collimated beam is focused onto the cavity sample using a Zeonex lens L_s, as depicted in Figure 3.21. We use a L_s lens of small focal length for strong focusing of the THz beam, of either 25 mm (f-number=1) or 17.5 mm (f-number=0.7). The THz beam reflected by the sample is collimated and deviated using a home-made THz beamsplitter. It is made of a stretch 75 μm thick Mylar film for a transmission and refletion at 45 ° of the incoming beam at 700 GHz of 50 %. The collimated beam is then focused onto the TeraPyro Lytid pyroelectric sensor using a 1-inch Zeonex lens L_s of focal lens 50 mm (f-number=2). As the bandwidth of the pyroelectric detector is limited to 50 Hz, we modulate the THz beam at a repetition rate of 47 Hz and the output signal of the pyroelectric detector is read-out by a lock-in amplifier with an integration time of 300 ms. We analyze the signal-to-noise (S/N) ratio of the set-up and measure a S/N ratio as low as 0.0013. Optimal alignments are made possible thanks to motorized displacements in the x, y, z directions of the sample holder.

Study of spatial inhomogeneities

In this section, we exploit our high-resolution THz characterisation tool to study irregularities in the basic Tamm cavity that may result from 1/ the stacking stage, which is sensitive to the force applied to the screws that hold the structure together, and 2/ variations in the thickness of the vacuum layers due to the curved spacers. To this aim, we record the reflection spectra of a basic 2 layers Tamm cavity at different positions in the XY plane for a fixed Z position (see Fig. 3.21). Figure 3.22 reports the reflection spectra for two distinct positions on the Tamm cavity, distant from 6.5 mm. We observe that the Tamm resonances are shifted by 6.8

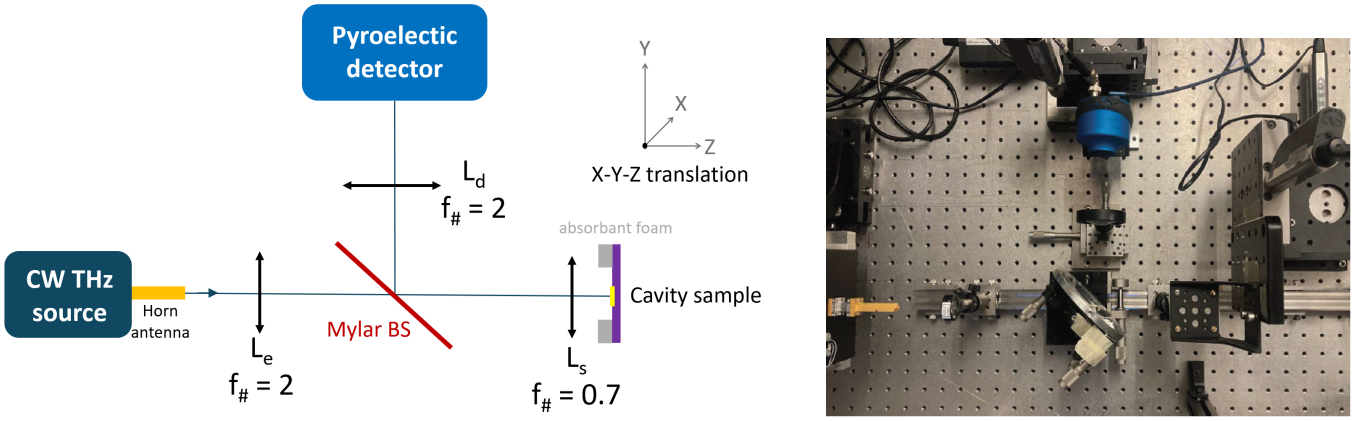

Figure 3.21: Scheme and photography of the set-up based on an THz electronic source optimized for the characterization of THz coupled-mode Tamm cavities and THz hybrid resonators based on a coupled-mode Tamm cavity and a single LC resonator.

GHz from 685.6 GHz for position 1 to 692.4 GHz for position 2. Moreover, the Q-factor of the resonance is 48 for position 1 and 66 for position 2, which represents a non-negligible variation of $\sim$ 30%. Moreover, these values of Q are lower than the value of Q=100 predicted by the TMM calculation. Then, we record reflection spectra by mapping a large surface of the Tamm cavity and, by analyzing the data, we estimate an average shift in the resonance frequency of 3.5 GHz/mm over the plane of the Tamm cavity (XY plane). This value is to be compared to the size of the THz beam on the surface of the Tamm cavity sample. We measure the diameter of the THz beam focused on the surface of the sample by replacing the sample with the pyroelectric detector and recording a XY map. We determine a typical diameter (FWHM) at 700 GHz of 1.6 mm. We therefore deduce that the resonance frequency is typically shifted by $\sim$ 5.5 GHz within the surface of the focused THz beam, which fully explains the lower value of the Q-factor measured compared to that predicted.

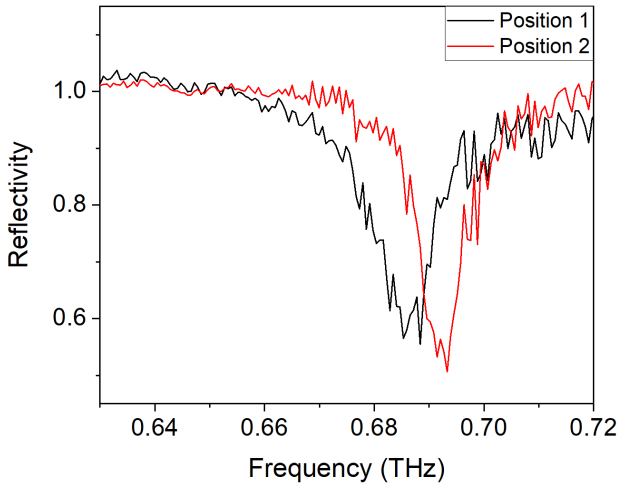

Figure 3.22: Reflectivity spectra of a 2-layers basic Tamm cavity at two different positions, apart from 6.5 mm, resulting in different resonance frequency, linewidth and peak depth due to spatial inhomogeneities.

To reduce these spatial inhomogeneities in the basic Tamm cavity, we use a torque screw-

driver to uniformly tighten the 4 screws on the sample mounting piece. We mount a 3 layers Tamm cavity using this torque screwdriver with a force of 2 cN.m and compare its reflection properties with a similar Tamm cavity mounted with a basic screwdriver. In average, we measure that the resonance frequency shift is reduced from 23 GHz down to 1.6 GHz using the torque screwdriver, and the Q-factor is significantly enhanced from 70 to ∼190. Note that the Q-factor predicted by TMM calculation for a 3 layers Tamm cavity is 588. We also measure that the gradient of the resonance frequency shift is reduced from 3.5 GHz/mm with no control to 1.6 GHz/mm using the torque screwdriver, and can even reach 0.3 GHz/mm at specific location. These values show the significant improvement in the procedure for assembling the complete Tamm cavity structure using the torque screwdriver.

Study of k-broadening effects

In the previous section, we have succeed to significantly reduce the spatial inhomogeneities of basic Tamm cavity. In this section, we study the influence on the resonance frequency and Q-factor of the multiple k-components of the THz beam incident on the basic Tamm cavity due to its strong focusing.

It is important to point out that Tamm modes have an in-plane parabolic dispersion. Figure 3.23 shows the calculated modal dispersion relation of a 2 layers and a 3 layers Tamm cavity for TE and TM polarization. The dispersion is parabolic, similarly to a Fabry-Perot mode, and distinct for TE and TM polarizations due to the polarization dependence of the reflections at the air-dielectric interfaces. Being excited by free-space THz waves, the Tamm mode is radiative and lies within the light cone.

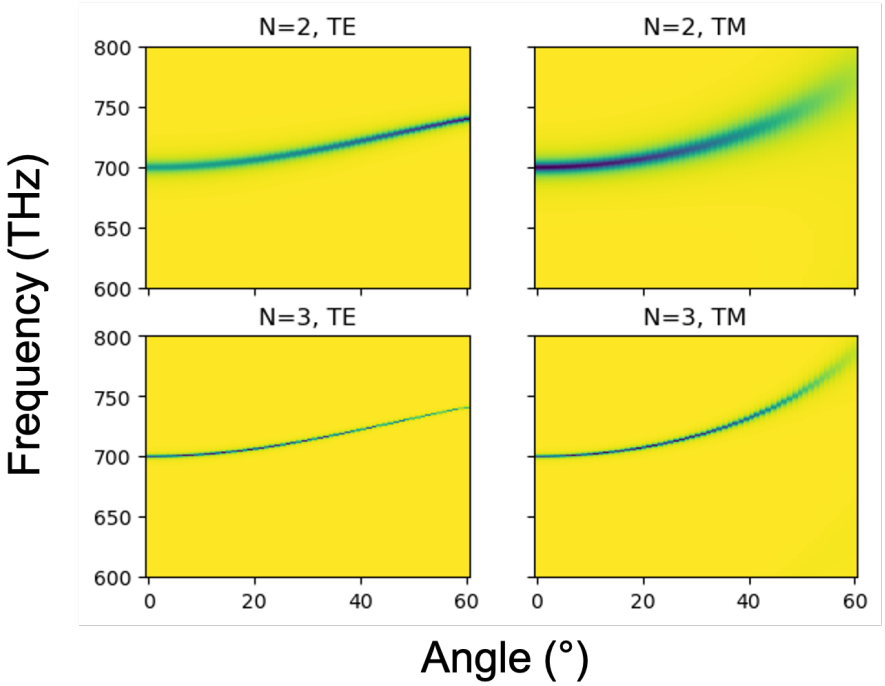

Figure 3.23: Dispersion relation versus incidence angle of the 2 layers (N=2) and 3 layers (N=3) Tamm cavity for TM and TE polarization predicted from TMM calculation.

This parabolic dispersion needs to be taken into account when the THz probe beam is strongly focused. Indeed, in the case of a collimated incident THz beam, the in-plane components of the wavevector, $k_{//}$, are negligible and the incidence angle θ is close to 0. This is more or less the configuration in which reflectivity measurements are carried out with our FTIR interferometer. On the other hand, the THz beam is highly focused in this set-up and is therefore composed of a wide range of in-plane components of the wavevector, $k_{//}$. The incidence angle of the THz beam θ_{max} is determined by to the f-number (or the numerical aperture N.A.) of the lens L_S. The dependence of the resonance frequency to the in-plane incoming wavevector, $k_{//}$, leads to an averaging effect for strongly focused incoming THz beam, the direct consequence of which is a reduction in the quality factor Q of the Tamm resonance. In other words, the incoming beam carries a continuum of different in plane k-wavevectors, which encounter different resonance frequencies. To compute this effect, we approximate our THz beam by a Gaussian shape. The maximum angle permitted by the lens is given by θ_{max}=arctan($\frac{D}{2f}$) with D the lens diameter and f its focal length. For D=25mm and f=17.5mm, we obtain θ_{max}= 35.5 °.

Figure 3.24 shows the reflectance spectra computed for a 3 layers Tamm cavity for a collimated incident THz beam ($k_{//}$=0) and for focused incident THz beam obtained using different f-number lens. The calculation is obtained by integrating over the $k_{//}$-distribution of a Gaussian beam incident with an angle θ_{max}. We clearly observe that increasing components of $k_{//}$ by using smaller f-number lens, severely broadens the Tamm resonance and reduces its magnitude. The resonance frequency also slightly shifts to higher frequencies from . The Q-factor is consequently reduced from 587 for $k_{//}$=0 down to 90 for f-number=1.

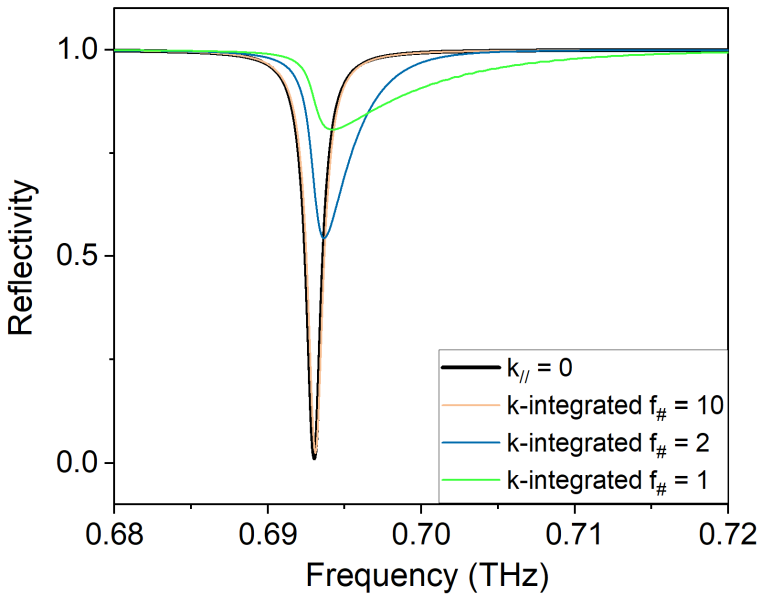

Figure 3.24: Calculated reflectance spectra of a 3 layers Tamm cavity for a collimated incident THz beam, $k_{//}$=0 (black curve) and for an incident THz beam focused by a lens of f-number=10 (orange), f-number=2 (blue), f-number=1 (green).

At last, we calculate the reflection spectra considering also the spatial inhomogeneities discussed in the previous section. Figure 3.25a shows the reflectance spectra of a 3 layers Tamm cavity computed for a collimated incident THz beam ($k_{//}$=0) and for a focused THz beam

(f-number=2 lens) and adding the integration due to spatial inhomogeneities. We first consider large spatial inhomogeneities of 3.3 GHz/mm, representing the case of uncontrolled Tamm mounting. We observe a narrow, high-contrast Tamm resonance for the collimated THz beam (black curve), which broadens and decreasees for the focused THz beam (blue curve), and becomes very broad and low-contrast if spatial inhomogeneities are added. By reducing the spatial inhomogeneity to 0.3 GHz/mm, corresponding to stacking with a torque screwdriver, the Tamm resonance of the calculated reflectance spectra shown in Fig3.25a broadens and attenuates for the focused THz beam compared to the collimated beam as before, but the impact of spatial inhomogeneity is no longer significant and can be considered negligible.

This study shows that to accurately estimate the Q factor and the contrast of a resonance in a coupled-mode Tamm cavity, it is required to implement an advanced experimental system that enables $k_{//}$-filtering.

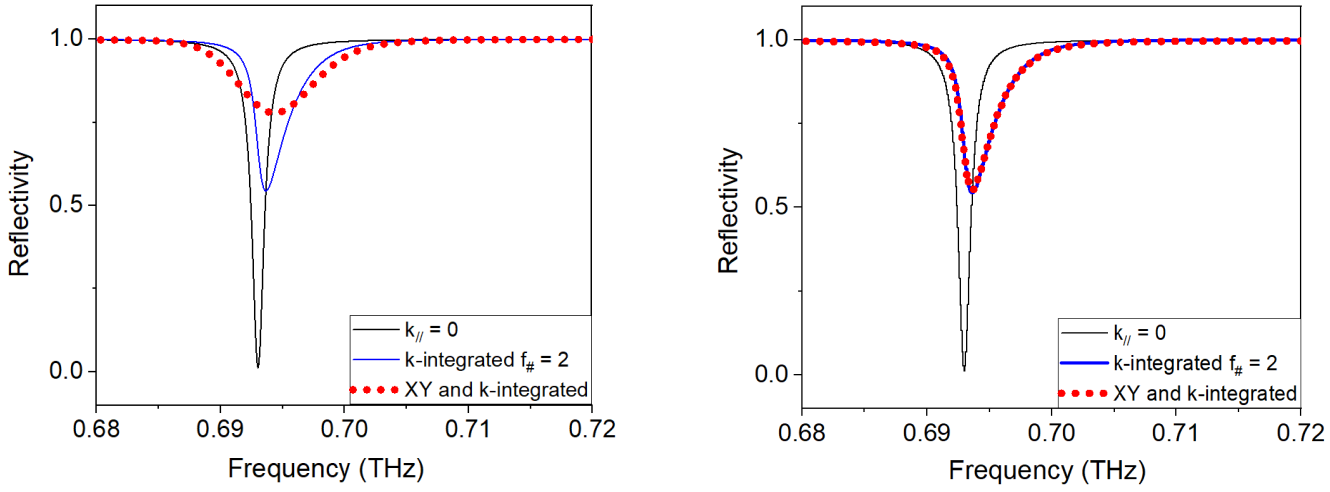

Figure 3.25: **(a)** Calculated reflectance spectra of a 3 layers Tamm cavity for a collimated incident THz beam (black curve), for an incident THz beam focused by a lens of f-number=2 (blue) and adding the integration due to spatial inhomogeneities of 3.3 GHz/mm. **(b)** Calculated reflectance spectra of a 3 layers Tamm cavity for a collimated incident THz beam (black curve), for an incident THz beam focused by a lens of f-number=2 (blue) and adding the integration due to spatial inhomogeneities of 0.3 GHz/mm.

3.5.2 Lateral confinement of the Tamm mode

As discussed previously, an important step towards the realisation of hybrid cavities based on a confined-mode Tamm cavity coupled to a single LC resonator, is to get knowledge on confined-mode Tamm cavity alone, shown in Fig. 3.20a. So far, this type of cavity has been studied only in the near-infrared range [33]. In this section, we present a preliminary study of confined-mode Tamm cavity in the THz spectral range.

We start by numerically study a Tamm cavity composed of a DBR structure on which a 100 nm-gold disk is deposited. We use the eigenfrequency solve element of COMSOL Multiphysics to calculate the resonance frequency of the modes and their quality factors Q. We simulate a

3 layers Tamm cavity with a resonance frequency ∼700 GHz to match to spectral range of our experimental set-up, corresponding to a wavelength $\lambda = 428$ μm. Such resonance frequency is obtained for silicon layers of 94 μm thickness ($\frac{3\lambda}{4n_{Si}}$) spaced by 107 μm vacuum gap ($\frac{\lambda}{n_{Si}}$).

The profiles of the electric field of the fundamental modes are depicted in Fig. 3.26 for several disk diameters, ranging from d=5λ down to d=0.5λ. By symmetry, the calculation is reduced to two dimensions and to the half the structure in order to save calculation time. Perfectly matched layers (PML) are placed at the edge of the calculation zone to avoid unphysical reflections due to the fact that the calculation space is necessarily finite. For the large diameter disk d=5λ, we observe that the Tamm mode exists only beneath the gold disk, whereas it was extending over the whole metallic plane with an infinite layer of gold. Therefore, the Tamm mode is now confined in the three directions of space. The electric field norm decreases vertically in the structure as in the 2D Tamm cavity case.

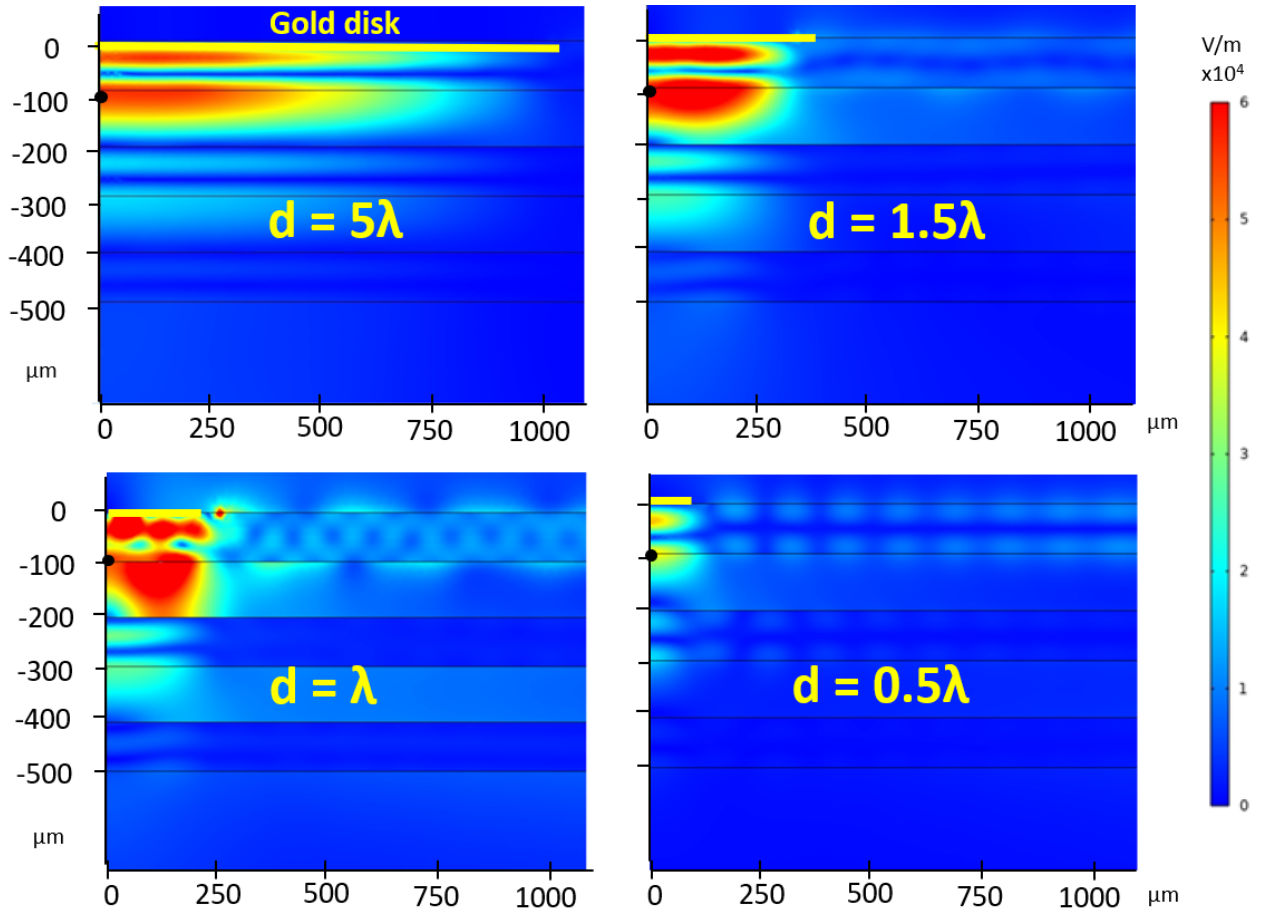

Figure 3.26: Electric mode profile of a 3 layers Tamm cavity with a gold disk represented by the yellow rectangles. From the upper left to the lower right, the gold disk size is 5λ, 1.5λ, λ and 0.5λ, with $\lambda = 428$ $\mu m = 0.7$ THz.

When the disk diameter is reduced to d=1.5λ, the electric field is more confined and more intense, but when the disk diameter is reduced to d=1λ and d=0.5λ, the profile of this fundamental mode degrades and leaks from the area beneath the disk. Actually, the mode leaks horizontally within the silicon layers, probably due to the diffraction losses that occur at the edge of the disk.

Figure 3.27 shows the electric field norm at the red dot in Fig.3.26 as a function of the disk diameter. The electric field norm increases when the diameter of the disk is reduced from 15 λ (a value equivalent to that of a basic Tamm cavity with an infinite metal layer) to d=1.7λ. At this point, the electric field amplitude is maximum with an increase of a factor of ∼10. For diameters below d=1.7 λ, the electric field decreases abruptly, which is consistent with the degradation of the mode profile observed in Fig. 3.26.

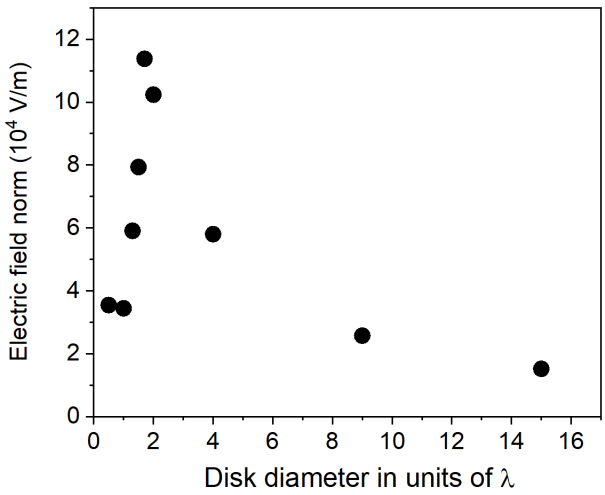

Figure 3.27: Electric field norm as a function of the disk diameter in units of λ at the interface between the top silicon layer of the DBR and the vacuum where a material system can easily be deposited (see the black dots in Fig. 3.26).

The eigen-modes analysis based on the finite element method on COMSOL Multiphysics also provides the complex eigenfrequency of the modes. The imaginary part of the eigenfrequency represents the damping of the mode, and the associated quality factor is given by Q=$|\frac{Re(\widetilde{f})}{2Im(\widetilde{f})}|$. Figure 3.28 shows the resonance frequency (a) and the quality factor (b) of the fundamental mode as a function of the metallic disk diameter. The resonance frequency and the quality factor remain relatively constant down to d=4λ. Below, the resonance frequency increases and Q decreases quite sharply with the disk diameter decrease. We attribute the drop of Q to an increase in coupling to the leakage substrate modes mentioned above. Studies are currently in progress to interpret these observations in more depth.

Lateral confinement of the Tamm modes is particularly easy to achieve by optical lithography, and leads to an increase in the electric field at the silicon/vacuum interface where a discrete quantum material can be placed. These results are promising for the realization of hybrid cavities based on the coupling of a confined-mode Tamm cavity and a single LC resonator. However, the optimal disk diameter to achieve the strong coupling regime between the two localized resonators requires future studies.

3.5.3 Characterization of THz confined-mode Tamm cavity

In this section, we present a first characterization of the coupled-mode Tamm cavity of diameter d=5 λ using the new experimental set-up we have implemented. We fabricate a 3 layers Tamm

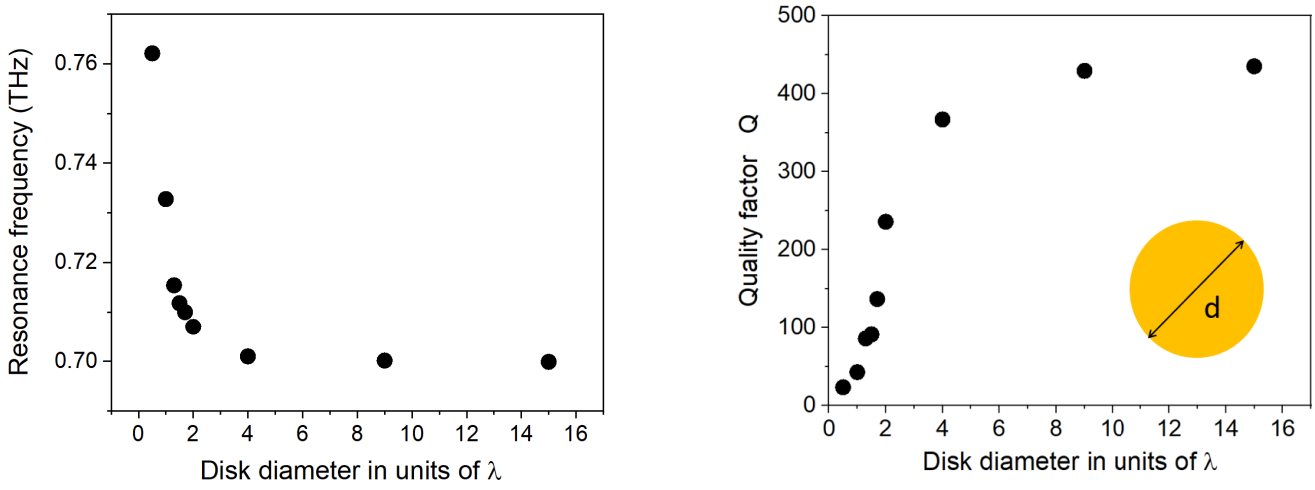

(a) (b)

Figure 3.28: **(a)** Tamm mode resonance frequency as a function of the disk diameter in units of λ, at the same point location.). **(b)** Evolution of the Q-factor as a function of the gold disk diameter of a 3 layers coupled-mode Tamm cavity with a resonance frequency of 700 GHz.

cavity with a resonance frequency ∼700 GHz to match to spectral range of our experimental set-up, corresponding to a wavelength $\lambda = 428$ μm. Such resonance frequency is obtained for silicon layers of 94 μm thickness ($\frac{3\lambda}{4n_{Si}}$) spaced by 107 μm vacuum gap ($\frac{\lambda}{n_{Si}}$). We first measure reflectivity at the fixed frequency of 685 GHz, scanning the sample position in the XY plane to determine the precise position of the mode-coupled Tamm cavity. Then, we record a high-resolved reflectivity spectrum shown in Fig. 3.29. The Q-factor of the resonance extracted from a Lorentzian fit of the data is as high as 490 at a resonance frequency of 685 GHz.

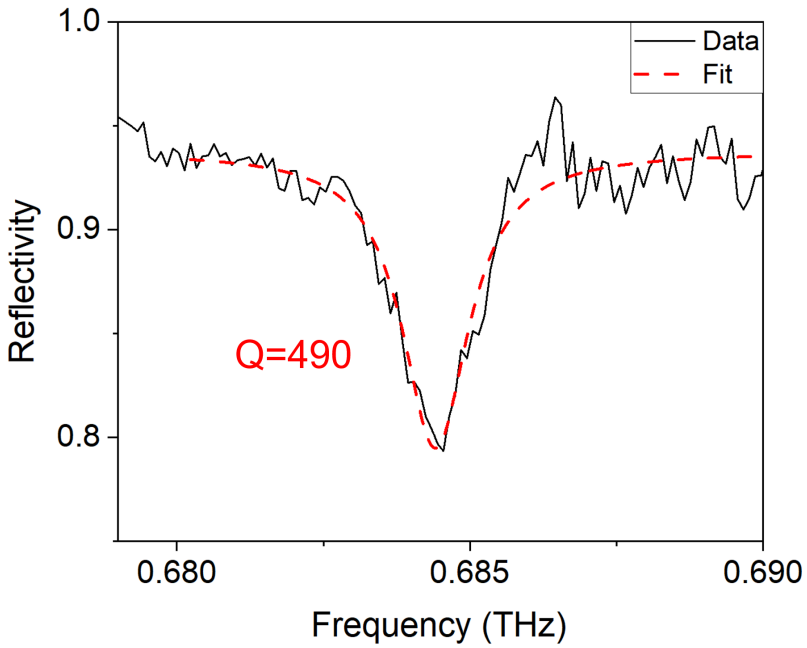

Figure 3.29: High resolution reflection spectrum of a three Si layers Tamm cavity, measured with the set-up based on an electronic source. The thickness of the Si layers for this cavity is 94 μm thickness ($\frac{3\lambda}{4n_{Si}}$) spaced by 107 μm vacuum gap ($\frac{\lambda}{n_{Si}}$). The FWHM of the Tamm resonance is 1.4 GHz, corresponding to a quality factor of 490.

Our study highlights the potential of hybrid resonators based on strongly coupled Tamm cavity to LC metamaterials for conciliating a high Q (Q=37) with sub-λ mode volume (V=$2 \times 10^{-4}\lambda^3$). Our work also shows that this approach must be adapted for an efficient coupling with a discrete material system such as double GQD. Our strategy is developp original hybrid resonators based on a coupled-mode Tamm cavity strongly coupled to a single LC resonator. Our preliminary research in this direction is promising and further studies are being carried out by my thesis group.

Bibliography

[1] CH Zhang et al. "Spontaneous emission probabilities at radio frequencies". *Phys. Rev.*, 69, p. 681, 1946.

[2] Anton Frisk Kockum et al. "Ultrastrong coupling between light and matter". *Nature Reviews Physics*, 1, 1, pp. 19–40, 2019.

[3] G. Scalari et al. "Ultrastrong Coupling of the Cyclotron Transition of a 2D Electron Gas to a THz Metamaterial". *Science*, 335, 6074, pp. 1323–1326, 2012.

[4] David Hagenmüller, Simone De Liberato, and Cristiano Ciuti. "Ultrastrong coupling between a cavity resonator and the cyclotron transition of a two-dimensional electron gas in the case of an integer filling factor". *Phys. Rev. B*, 81, p. 235303, 2010.

[5] Janine Keller et al. "Few-Electron Ultrastrong Light-Matter Coupling at 300 GHz with Nanogap Hybrid LC Microcavities". *Nano Letters*, 17, 12, pp. 7410–7415, 2017.

[6] B. Paulillo et al. "Room temperature strong light-matter coupling in three dimensional terahertz meta-atoms". *Applied Physics Letters*, 108, 10, p. 101101, 2016.

[7] Andreas Bayer et al. "Terahertz Light–Matter Interaction beyond Unity Coupling Strength". *Nano Letters*, 17, 10. PMID: 28937772, pp. 6340–6344, 2017.

[8] Yanko Todorov and Carlo Sirtori. "Few-Electron Ultrastrong Light-Matter Coupling in a Quantum LC Circuit". *Phys. Rev. X*, 4, p. 041031, 2014.

[9] Mathieu Jeannin et al. "Ultrastrong light-matter coupling in deeply subwavelength THz LC resonators". *ACS photonics*, 6, 5, pp. 1207–1215, 2019.

[10] Mónica Benito and Guido Burkard. "Hybrid superconductor-semiconductor systems for quantum technology". *Applied Physics Letters*, 116, 19, p. 190502, 2020.

[11] Stephan André et al. "Few-qubit lasing in circuit QED". *Physica Scripta*, 2009, T137, p. 014016, 2009.

[12] Audrey Cottet et al. "Cavity QED with hybrid nanocircuits: from atomic-like physics to condensed matter phenomena". *Journal of Physics: Condensed Matter*, 29, 43, p. 433002, 2017.

[13] Michael Reitz, Christian Sommer, and Claudiu Genes. "Cooperative Quantum Phenomena in Light-Matter Platforms". *PRX Quantum*, 3, p. 010201, 2022.

[14] Simone De Liberato. "Virtual photons in the ground state of a dissipative system". *Nature Communications*, 8, 1, p. 1465, 2017.

[15] E. Yablonovitch. English. *IEE Proceedings - Optoelectronics*, 145, 391–397(6), 1998.

[16] Nicolas Marquez Peraca et al. "Ultrastrong light–matter coupling in semiconductors". *Semiconductors and Semimetals*. Ed. by Steven T. Cundiff and Mackillo Kira. Vol. 105. Elsevier, 2020, pp. 89–151, 2020.

[17] Qi Zhang et al. "Collective non-perturbative coupling of 2D electrons with high-quality-factor terahertz cavity photons". *Nature Physics*, 12, 11, pp. 1005–1011, 2016.

[18] Xinwei Li et al. "Vacuum Bloch–Siegert shift in Landau polaritons with ultra-high cooperativity". *Nature Photonics*, 12, 6, pp. 324–329, 2018.

[19] Elena Mavrona et al. "THz Ultrastrong Coupling in an Engineered Fabry–Perot Cavity". *ACS Photonics*, 8, 9, pp. 2692–2698, 2021.

[20] Curdin Maissen et al. "Ultrastrong coupling in the near field of complementary split-ring resonators". *Phys. Rev. B*, 90, p. 205309, 2014.

[21] Curdin Maissen et al. "Ultrastrong coupling in the near field of complementary split-ring resonators". *Phys. Rev. B*, 90, p. 205309, 2014.

[22] Shima Rajabali et al. "An ultrastrongly coupled single terahertz meta-atom". *Nature communications*, 13, 1, pp. 1–8, 2022.

[23] Fanqi Meng et al. "Nonlocal collective ultrastrong interaction of plasmonic metamaterials and photons in a terahertz photonic crystal cavity". *Optics express*, 27, 17, pp. 24455–24468, 2019.

[24] Lei Cao et al. "Can a terahertz metamaterial sensor be improved by ultra-strong coupling with a high-Q photonic resonator?" *Opt. Express*, 30, 8, pp. 13659–13672, 2022.

[25] Fanqi Meng et al. "Strong interaction between two photons and a plasmon of a complementary metamaterial in a terahertz dual cavity". *Opt. Express*, 29, 26, pp. 42420–42434, 2021.

[26] Mathieu Jeannin et al. "Absorption engineering in an ultrasubwavelength quantum system". *Nano letters*, 20, 6, pp. 4430–4436, 2020.

[27] Simon Messelot. "Terahertz Tamm cavities for light-matter coupling with graphene based materials". PhD thesis. 2021, 2021.

[28] Guillaume Lheureux et al. "Polarization-Controlled Confined Tamm Plasmon Lasers". *ACS Photonics*, 2, 7, pp. 842–848, 2015.

[29] C. Symonds et al. "High quality factor confined Tamm modes". *Scientific Reports*, 7, 1, p. 3859, 2017.

[30] Ig. Tamm. "Über eine mögliche Art der Elektronenbindung an Kristalloberflächen". *Zeitschrift für Physik*, 76, 11, pp. 849–850, 1932.

[31] Simon Messelot et al. "Tamm Cavity in the Terahertz Spectral Range". *ACS Photonics*, 7, 10, pp. 2906–2914, 2020.

[32] Simon Messelot et al. "High Q and sub-wavelength THz electric field confinement in ultrastrongly coupled THz resonators". *Photon. Res.*, 11, 7, pp. 1203–1216, 2023.

[33] Guillaume Lheureux. "Étude de l'effet laser dans les structures à plasmon Tamm". PhD thesis. 2015, 2015.

Conclusion and perspectives

In this thesis, we have studied the transport through a physically etched double GQD and the properties of hybrid THz resonators with the perspective to develop quantum THz devices based on a two-level system coupled to a THz resonator. The three chapters we have presented reveal that a double GQD effectively acts as an artificial two-level system in the THz range, and that its insertion into a hybrid THz resonator based on a confined-mode Tamm cavity with a single LC resonator is a very promising approach of achieving different light-matter coupling regimes, from weak to ultra-strong.

In Chapter 1, we described the steps involved in the clean room nanofabrication of double GQDs embedded into LC THz resonators, starting with the mechanical exfoliation of a graphene monolayer to obtain large graphene flakes of the order of the dozen μm^2. The graphene monolayer wass encapsulated by two hBN layer to preserve its high quality. The exfoliation of hBN flakes, and particularly thin, large and smooth ones, to stack hBN/graphene/hBN 2D heterostructures has represented a major difficulty. A precise and challenging electron-beam lithography was performed on the stack to physically pattern the two quantum dots, the narrow constrictions and the large number of gates on the reduced-size heterostructure. After development, RIE etching revealed the patterned double GQDs structure along with the 1D line for the future 1D edge contacts. The etching step required special attention, as the etching process was not perfectly isotropic and could break the 40 nm thick graphene constrictions. A second electron-beam lithography was performed to pattern the contacts with larger pads, which was made possible with a chromium/gold evaporation and lift-off process. The development of an effective protocol for the nanofabrication of a single-electron transistor using a double GQD integrated into an LC resonator has been a significant technological challenge. Nonetheless, despite the obstacles faced, the fabrication process is now fully functional, allowing for the fabrication of multiple devices.

The Chapter 2 is dedicated to the characterization of the double GQD based devices fabricated in the previous chapter. We characterized and analyzed the dark transport at low temperature through a double GQD based device in a single electron transistor configuration. We started by describing the state of the art of quantum dots in the THz spectral range that point out that due to their optical properties and THz quantum responses, large GQDs are promising to achieve a two-level system at THz frequencies. Then, we reported on the dark finite bias transport spectroscopy measurements through the double GQD at low temperature (300 mK). Charge stability diagrams we recorded revealed the characteristic honeycomb pattern of double quantum dot behavior, as well as triple points. By analyzing the data, we showed

that when electrons can tunnel coherently and one by one from a quantum dot to the other through the inter-dot tunneling barrier, the eigenstates become delocalized and extend over the entire double GQD system, leading to a bonding and anti-bonding eigenstates formation. The resonance frequency of the two-level system f_{res} is estimated within the range 0.13-0.17 THz, demonstrating that double GQD acts as a two-level system in the THz range.

In Chapter 3, we explored original hybrid THz resonators as the second building block for the perspective to develop quantum THz devices based on a two-level system coupled to a THz resonator. We recalled the basic of resonators, the state-of-the-art of resonators at THz frequencies and the properties of THz Tamm cavity that is included in the THz hybrid resonator. We then presented our deep investigation of hybrid resonators based on Tamm-cavity coupled to LC circuit metamaterial. While Tamm cavity hold a high Q and low mode confinement and LC circuit metamaterial hold a low Q but high mode confinement, we showed that by strong coupling the two types of resonators, the resulting hybrid THz resonators conciliate the advantage of each resonators providing a efficient electromagnetic mode energy storage (Q=37) with electromagnetic mode energy confinement on sub-wavelength volume (V=$2 \times 10^{-4}\lambda^3$). However, these hybrid THz resonators must be adapted for for an efficient coupling with a discrete material system such as double GQD, as the resonator modes extend laterally over the plan of the layers and require to be restricted in all directions of space to be efficiently coupled to a single LC resonator in which would e placed the double GQD. Our approach was replaced the gold layer to a finite gold disk, to confine the Tamm mode, on top of which is patterned a single LC resonator. We presented our research on the THz confined-mode Tamm cavity. Using FEM simulations, we analyzed the properties of the Tamm confined modes and in particular the evolution of Q factor and spatial profile of the electric field as a function of the disk diameter. Our analysis revealed that under a critical diameter, the confined Tamm modes begin to leak by coupling to substrate modes. We then reported on the implementation of an experimental set-up for the high frequency-resolved characterization of reflectivity of confined-mode Tamm cavites and showed a first result on a 5λ confined-mode Tamm cavity.

In this thesis work, the resonance frequency of the two-level system was not matched the LC resonator resonance frequency, which prevented the coupling signature from being observed. A perspective is to reduce the length of the constriction between the two quantum dots to increase inter-dot coupling up to 300 GHz. This will make it possible to probe vacuum field-induced conductance changes in the double GQD ultra-strongly coupled to the LC resonator using dark transport measurements at low temperature.

Also in perspective, transport measurements through the fabricated double GQD based devices under coherent THz illumination could provide unique insight on the two-level system properties. During this PhD work, we carried out such measurements at Soleil on the AILES beamline, in collaboration with Pascale Roy and Jean-Blaise Brubach, and Kelly Rader. The experimental set-up was based on the SOLEIL synchrotron source, a Bruker IFS125 HR spectrometer and the double GQD devices were placed in an adiabatic demagnetization refrigerator (ADR) operating at 500 mK. Unfortunately, the experiments were not conclusive, mainly because the sample connections broke either during the trip from LPENS to Soleil or during the

measurements, due to uncontrolled spikes. We spent several days there, but were unable to succeed. My thesis group has recently acquired a dilution cryostat with optical access perfectly suited to such experiments. It can operate from 10 mK to 30 K with a magnetic field of up to 5 Tesla. The illumination of a double GQD-based device with coherent THz radiation could enable to directly measure the resonance frequency of the two-level system, as well as the photon-assisted transport in the device, which would provide in particular information on the coherence properties of this two-level system and paving the way for its control.

Further development of hybrid cavities should enable to design a hybrid cavity based on confined-mode Tamm cavity coupled to a single LC resonator optimized for its coupling to a double GQD, opening the way to the realization of THz quantum devices exploiting the different light-matter coupling regimes. More specifically, by inserting the double GQD in a high Q mode-confined Tamm cavity and exploiting the weak coupling regime high quantum efficiency photon detectors could be achieved and moreover, by including a charge detector to individual charging events in the double DQD, the detection of THz photons down to the single-photon level could be reached. Exploring the strong coupling regime by inserting the double GQG to a hybrid cavity based on confined-mode Tamm cavity coupled to a single LC resonator could be explore for generating THz squeezed light. Indeed, two incident photons would be absorbed and reemitted down the ladder of states to produce squeezing. The ultra-strong coupling regime between double GQDs and a THz hybrid resonators with deep-subwavelength mode volume could also enable detection of non-classical states of THz light, such as squeezed states.

Acknowledgments

Mes premiers remerciements vont à Juliette, ma directrice de thèse. Tu as été un soutien constant tout au long de ces trois ans et demi, m'encourageant toujours à repousser mes limites et à viser l'excellence. Grâce à toi, j'ai énormément appris, tant sur le plan scientifique que personnel. Je garderai un précieux souvenir de nos échanges. Dans ma vie professionnelle, les défis à venir me sembleront plus abordables grâce à tes enseignements. Un grand merci pour toute l'aide apportée, du début du stage en avril 2021 jusqu'à aujourd'hui.

J'aimerais également remercier mon jury, à commencer par mes deux rapporteurs de thèse, François Parmentier et Olivier Gauthier-Lafaye. Merci d'avoir accepté de consacrer du temps à mes travaux, pour vos commentaires ainsi que pour nos discussions lors de ma soutenance. Je tiens aussi à remercier les autres membres du jury, Cheryl Feuillet-Palma et Jean-François Lampin d'avoir accepté d'être examinateurs de ma thèse. Merci également à Yanko Todorov pour sa participation en tant que membre invité.

La recherche repose sur la participation de nombreux acteurs, sans qui ce projet de thèse n'aurait jamais abouti. Mes premières pensées vont vers l'équipe HQC de Takis Kontos et Matthieu Delbecq. Votre équipement et vos précieux conseils ont permis d'étudier mon dispositif dans les meilleures conditions. Merci pour votre présence, votre aide précieuse tout au long de cette collaboration, et merci à toute l'équipe de m'avoir accueilli dans votre labo !

Avant l'étude de cette fameuse double boîte, un (très) lourd travail en salle blanche a été nécessaire. Aujourd'hui, je suis fier de maîtriser ce process de nanofabrication, qui ressemble vraiment à une recette de cuisine. Comme dans toute bonne cuisine, le résultat est le fruit de la collaboration de tout un tas de monde. Je vais commencer par remercier Simon et Romaine, avec qui j'ai fait mes premiers pas en salle blanche. J'ai découvert un univers à part qui m'a tout de suite plu. Le personnel de la salle blanche y a grandement contribué : merci à Michael, Jose et Aurélie pour votre aide et la bonne ambiance apportée. Aurélien, je t'admire pour deux choses : d'abord, ta capacité à fabriquer des sandwiches et ta maîtrise de l'exfoliation du graphène, des techniques aussi complexes qu'essentielles pour mon projet. Ensuite, pour ta conviction inébranlable que le FC Metz est un grand club de football, franchement bravo. Enfin, je tiens à remercier Rebecca Ribeiro et toute son équipe au C2N de m'avoir enseigné leurs techniques d'exfoliation et de transfert. Super équipe, super labo, super salle blanche : mille mercis pour votre accueil ! Merci aussi à Jean-Blaise Brubach, Kelly Rader et toute l'équipe pour notre collaboration dans votre labo à SOLEIL, qui n'a malheuresement pas porté ses fruits. J'ai une nouvelle fois été super accueilli !

Il est indispensable de remercier toutes les personnes qui font tourner le laboratoire, Olga et le service administratif ; Christine, Noria, Nadia et le service financement ; Florent et Olivier pour la cryo ; Laurent et Philipe pour le service électronique ; ainsi que Yann, Pascal, Claude, Jean-Michel et bien d'autres. Chaque midi j'étais heureux (oui, heureux) de manger au Pôt,

merci à toute l'équipe et plus spécifiquement à Eric : j'espère que tu as apprécié ma soutenance. Tu as tenu de bons arguments en faveur d'un voyage en Colombie, je saurai m'en souvenir.

Je tiens également à remercier Suhky, notre tant aimé chef du super groupe Nano-THz. Tu as joué ton rôle à la perfection, veillant à la bonne cohésion de l'équipe et en te souciant du bien-être de chacun, merci pour tout ! J'en profite pour remercier toute l'équipe Nano-THz, les anciens comme les nouveaux : Simon, Romaine, Thibault, Chao, Pavel (fais un effort au billard, s'il te plaît), Minoosh, Enzo, Joaquin, Thomas, Louis-Anne, Niloufar, Seonggil. Merci à Anna et Aurélie de digérer votre défaite aux JO de Fréjus ; bien joué Adrien. Merci à Bastien, Martin, Etienne, Sabrine, Louise, Soumya, Ismaël, Boris, et bien entendu Alexis, qui prendra la suite de ces travaux. Je te souhaite la meilleure des thèses !

Merci à Orsay pour toutes ces années, Hêlio et Emilie, Marylise, Fredo, Nils, Guillaume (dire que tu pilotes des avions c'est inquiétant, mais bravo), Emma, Maélie. Merci au 47 : Jojo, Dodo et Quentin, que je voyais tous les jours en Croatie, sur le fond d'écran de mon ordi du labo. Merci pour vos allers-retours entre le 47 et Paris, et tout ce qui s'en est suivi. J'en profite pour remercier Pedro Diaz et toute la Montagne, un sacré endroit. Merci à Hamza pour ses dégradés et à Bibani pour ses pizzas à 5 balles, des endroits où l'inflation n'est certainement pas leur problème. Aussi et ça c'est atroce, merci au P d'avoir égayé (Thierry aussi) mes nocturnes : on dormira quand on sera mort, j'te l'aurais dit direct.

Pour ces derniers mots, un grand merci à Pailloles.

Merci à Lou de m'avoir accompagné pendant cette thèse. Je n'ai pas assez de mots pour exprimer à quel point tu as été importante. Laisse-moi donc te le raconter toute notre vie.